Quantitative Magnetic Resonance Imaging Biomarkers for Diffuse Liver Disease:
Technical Development and Validation

By

Xiaoke Wang

A dissertation submitted in partial fulfillment of
the requirements for the degree of

Doctor of Philosophy
(Biomedical Engineering)

at the
UNIVERSITY OF WISCONSIN-MADISON
2019

Date of final oral examination: 09/06/2019

The dissertation is approved by the following members of the Final Oral Committee:

- Scott Reeder, Professor, Biomedical Engineering
- Diego Hernando, Associate Professor, Medical Physics
- Walter Block, Professor, Biomedical Engineering
- Oliver Wieben, Professor, Medical Physics
- Beth Meyerand, Professor, Biomedical Engineering

Abstract

Non-alcoholic fatty liver disease (NAFLD) is a common liver disorder hallmarked by abnormal deposition of fat, i.e.: hepatic steatosis. NAFLD can take the form of non-alcoholic steatohepatitis (NASH) or isolated steatosis. Both forms of NAFLD can cause chronic liver injuries which leads to the progression into liver fibrosis. At the same time, NAFLD is a known risk factor of type-II diabetes and premature cardiovascular diseases. Although liver fibrosis is less common than NAFLD, it has serious complications such as liver failure. Cirrhosis as a form of advanced fibrosis is a risk factor of hepatocellular carcinoma.

Effective treatments are emerging for NAFLD and liver fibrosis. Lifestyle intervention has been demonstrated to reduce hepatic steatosis and inflammation. In the case of viral hepatitis, treatment for hepatitis C virus infection often leads to the reversal of liver fibrosis (even in patients with cirrhosis). The accurate evaluation of hepatic steatosis and fibrosis using non-invasive magnetic resonance imaging (MRI) methods are needed to improve the diagnosis and treatment monitoring of patients afflicted by these conditions.

Chemical shift encoded (CSE)-MRI has been established as a quantitative imaging biomarker (QIB) for hepatic steatosis. In this dissertation, the effect of non-standardized spectral model of fat was evaluated such that meaningful comparisons can be made between results obtained at different research and clinical sites. A T_1-corrected variable flip angle (VFA) CSE-MRI was also proposed and rigorously evaluated for fat quantification in the hope of improving the precision of CSE-MRI fat quantification.

Quantitative diffusion MRI using an intra-voxel incoherent motion (IVIM) model and T_2 mapping have shown promise for the evaluation of liver fibrosis. However, some additional development and validation is required for them to be recognized as QIBs. In this dissertation, a novel acetone-based diffusion phantom was proposed to provide a controlled environment for the development of quantitative diffusion MRI techniques. Further, to enable the quantification of T_2 from the water signal (parenchyma) and simultaneous quantification of R_2*, a novel phase-based T_2 mapping technique was developed with its feasibility in the liver demonstrated.

Acknowledgements

I would first like to thank the University of Wisconsin-Madison Biomedical Engineering program, Dr. Aaron Field, and Dr. Walter Block for giving me the opportunity to study at this excellent University. This is a world class facility with an exceptionally beautiful campus and abundant high-quality academic resource.

I would also like to thank the department of Medical Physics and Radiology for the wonderful environment I have been working in. Part of this is a result of hard logistic work done by the IT-staff, administrative staff and especially the custodians whose arduous work often happened unnoticed throughout the nights. Special thanks to the many technicians for their hard work and their tremendous patience with my various quirky requests.

I would like to thank my advisor Dr. Scott Reeder and my thesis committee members: Dr. Diego Hernando, Dr. Walter Block, Dr. Oliver Wieben, Dr. Edward Jackson (Preliminary Exam) and Dr. Beth Meyerand for their guidance and their insightful advice. I have also had the pleasure of learning from many other brilliant researchers and engineers, especially Dr. Bruce Collick, Dr. Kang Wang, and Ann Shimakawa. Special thanks to Dr. David Harris and Dr. Anja Gwendolyn van der Kolk for teaching me the way of academic writing when I was deeply convinced I was too fundamentally flawed to learn it.

The graduate school experience for me has been volatile with many unforeseen challenges. Fortunately, I have met some extraordinary friends along the way. Their unrequited support and honesty, like shining beacons, has guided me in the darkest and most confusing of times. Special thanks to Stanley Kruger, David Niles, Larry Hernandez, Deb Horng, Gengyan Zhao, Fang Liu, and Gesine Knobloch. There are many more individuals unnamed here, who have been kind and inspirational.

At last, these dissertation research projects received financial and technical support from NIH (R01 DK083380, R01 DK100651, K24 DK102595, R01 DK117354, R01 DK088925, and R41 EB025729) and the UW ICTR grant UL1TR000427 from NIH/NCATS, GE Healthcare, and University of Wisconsin D2P Igniter Program.

Table of Contents

List of Figures

List of Tables

Chapter 1 : Introduction

Non-alcoholic fatty liver disease (NAFLD) results from the excess accumulation of fat in the liver in the absence of alcohol abuse. NAFLD is one of the most common liver disorders and may progress into more serious liver injury. Emerging treatments for NAFLD are becoming available but rely early and non-invasive diagnosis and treatment monitoring. The current gold standard for diagnosis is biopsy, which is risky with dangerous complications and suffers from sampling errors. The non-invasive gold-standard of steatosis (fat accumulation) evaluation is MR spectroscopy (MRS). Only a single voxel can be evaluated by MRS in a single breath-hold while the steatosis could be heterogeneously distributed in the liver. Chemical shift encoded MRI (CSE-MRI) is a valid quantitative imaging biomarker (QIB) for NAFLD after the correction of confounding effects. Compared with MRS, CSE-MRI can estimate spatially resolved steatosis over the entire liver.

In chapter 2, a more detailed review of NAFLD is given. Various biomarkers including MRI and non-MRI methods are compared. Although CSE-MRI is a valid QIB for evaluation of hepatic steatosis, there are remaining questions that must be answered to facilitate its widespread dissemination.

In chapter 3, the pre-calibrated spectral model of fat is discussed. In CSE-MRI, the spectral distribution of fat is treated as known a priori from pre-calibration mainly by MR spectroscopy. Several different pre-calibrated spectral models of fat were adopted in various studies of CSE-MRI fat quantification. This disparity makes it difficult to make meaningful comparisons between results from different research sites. In this chapter, the impact of these pre-calibrated spectral models of fat on the accuracy of CSE-MRI fat quantification was assessed in computer simulations and on a large in vivo dataset.

In chapter 4, a T_1-corrected CSE-MRI fat quantification technique was developed. Typically, multi-echo spoiled gradient echo (SGRE) signal was used in CSE-MRI fat quantification. A small flip angle is used to suppress T_1-related bias. This use of small flip angles is an inefficient use of available longitudinal magnetization and leads to low SNR in the source images. Higher SNR can be attained if SGRE signal can be acquired with larger flip angles and the effect of T_1 can be accounted for in the signal model. In this chapter, a CSE-MRI PDFF quantification technique using a large flip angle was developed and evaluated.

Liver fibrosis is a condition known for the accumulation of extracellular matrix (ECM) proteins, and is a result of chronic liver injuries such as chronic viral hepatitis (hepatitis B and C), non-alcoholic steatohepatitis, alcohol abuse, auto-immune hepatitis, among others. Advanced fibrosis (cirrhosis) afflicts 0.27% of the U.S. population and may cause complications such as ascites and hepatic encephalitis. Cirrhosis is also an established risk factor for hepatocellular carcinoma (HCC). Liver fibrosis can be reversible, but requires accurate diagnosis and staging, as well as removal or reversal of the underlying cause of liver injury.

In chapter 2, a more detailed review of liver fibrosis is also provided. Methods of staging the liver fibrosis such as liver biopsy, ultrasound, CT, MR elastography (MRE), diffusion MRI with an intravoxel incoherent motion (IVIM) model, and T_2 mapping are described. Diffusion MRI with IVIM and T_2 mapping have shown great potential and require no extra hardware.

In chapter 5, a phantom was designed for the development of quantitative diffusion MRI techniques. Estimates of the apparent diffusion coefficient (ADC) is an essential part of diffusion MRI with intravoxel incoherent motion (IVIM) model. However, the measurement of ADC showed wide variability across studies and sites. These variabilities are likely a result of unaddressed confounding factors. The development of quantitative diffusion MRI could benefit from a phantom with reproducible ADC that can be tuned over the entire physiological range. Currently available phantoms for diffusion MRI do not fulfill this need.

In chapter 6, a phase-based T_2 mapping technique feasible for whole liver T_2 mapping that is compatible with simultaneous CSE-MRI was developed. Quantitative T_2 mapping is promising biomarker for the staging of liver fibrosis. Single-echo spin-echo and multi-echo spin-echo methods are too time consuming to assess an entire liver over a breath-hold, which is required for the suppression of respiratory motion. Steady-state T_2 mapping techniques i.e. driven equilibrium single pulse observation of T_1 and T_2 (DESPOT2), double-echo steady-state (DESS), triple-echo steady-state (TESS) are faster. However, they are challenged by banding artifact (DESPOT2) and the presence of fat and iron (DESS&TESS). A feasible steady state T_2 mapping technique that has the potential to be corrected for the effect of fat and iron may advance the development of T_2 as a QIB for the staging of liver fibrosis.

Finally, chapter 7 summarizes the contribution of this dissertation towards the development of QIB for diffuse liver disease. Future work expanding on the work presented is also discussed.

Chapter 2 : Background

2.1 Diffuse Liver Disease

Non-alcoholic Fatty Liver Disease (NAFLD)

Non-alcoholic fatty liver disease (NAFLD) is a disorder where excess fat accumulates in the liver (steatosis) in the absence of alcohol abuse[1]. As a common chronic liver disease, it affects up to 30% of the adult U.S. population[2]. NAFLD is associated with a series of conditions: obesity, hyperlipidemia[1], type-2 diabetes mellitus[3], and metabolic syndrome with a specific hepatic insulin resistance that could also lead to diabetes[4]. These association suggested possible causes of the steatosis and provided clues to treatment designs of NAFLD.

A subgroup of NAFLD known as non-alcoholic steatohepatitis (NASH) is distinguished from isolated steatosis by the presence of inflammation, hepatocyte injury and often fibrosis. Liver fibrosis is often diagnosed in patients with NASH[5]. Further, in combined results of studies clinically following patients with NASH, around 43% progressed to develop fibrosis, 8%-17% cirrhosis, and 3% terminal liver failure[6]. It is also well-established that NASH is a risk factor associated with hepatocellular carcinoma (HCC) in patients with and without cirrhosis[7]. Finally, even isolated steatosis could cause oxidative stress which activates hepatic stellate cells, and in time, leads to liver injury and fibrosis[8].

Treatments are available for patients diagnosed with NALFD to prevent progression into more serious liver injuries. Lifestyle interventions which promotes healthier diet, physical activities and exercise are an effective and established treatment of NAFLD[9]. A prospective study of 293 patients with histologically proven NASH who took on lifestyle changes recommended for treatment was conducted by Vilar-Gomez et al[10]. A dose-effective relationship was found between weight-loss and steatosis improvement, NASH-resolution and fibrosis-regression evidenced by the changes in histological parameters. Steatosis improvements was defined as a reduction of at least 2 points in the NAFLD activity score (NAS), including at least 1-point in more than one category. NASH-resolution was defined as the lack of hepatocellular ballooning, as a marker of liver injury. The fibrosis-regression was defined as a reduction of at least 1 point in the fibrosis score.

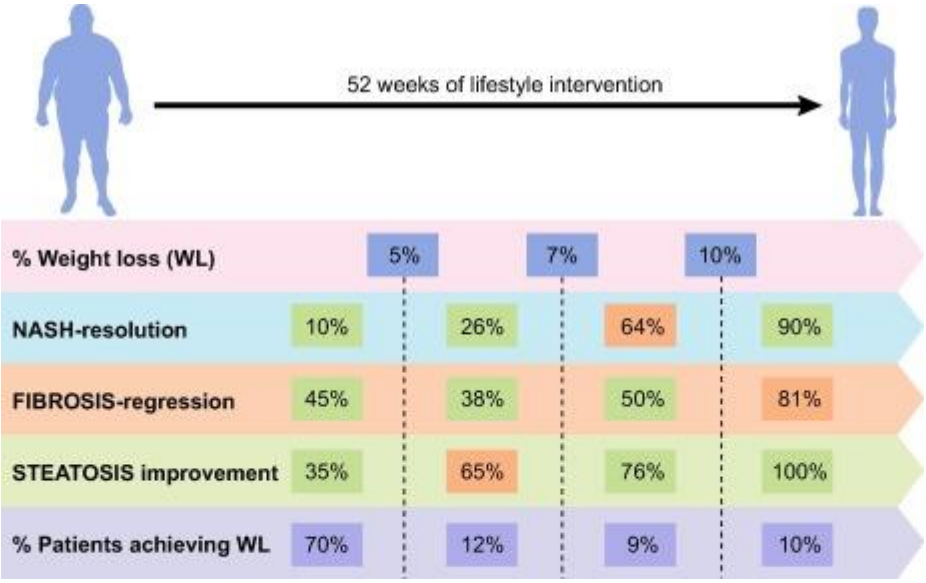

Figure 2.1 The strong correlation between patient weight-loss and the effectiveness of NAFLD treatment indicated by NASH-resolution, fibrosis-regression and steatosis improvement.Image from Vilar-Gomez et al. J Hepatol (2017).

Inspired by strong correlation between NAFLD and insulin resistence[11], pilot studies have shown that insulin sensitizing agents such as metformin[12] and thiazolidinediones[13] will reduce aminotransferase levels, reduce liver fat and improve liver histology[14]. However, randomized controlled studies are still required to validate these agents as effective treatment[14].

With the discovery of effective treatment, early diagnosis can help prevent the progression of NAFLD into life-threatening conditions while improving the overall health of NAFLD patients.

Liver Fibrosis

The traditional view of hepatic fibrosis was the process of a collagen-rich tissue replacing damaged and collapsed parenchyma[15]. More recently, liver fibrosis has been modeled as a sophisticated wound healing process in response to chronic liver injury[16]. In this process, the accumulation of extracellular matrix (ECM) protein makes up fibrous scar and distorts the hepatic architecture. Cirrhosis develops when consequent nodules of regenerating hepatocytes appear[16].

The leading causes of liver fibrosis in industrialized countries are hepatitis C virus (HCV) infection, alcohol and non-alcohol fatty liver disease[16]. In a study conducted in France of 7554 subjects[17], the prevalence of liver fibrosis was estimated as 2.8%, and that of cirrhosis 0.3%. In the United State, the prevalence of liver cirrhosis[18] was estimated to be 0.27%, or an estimated 891,000 people. Once cirrhosis develops, the hepatocellular dysfunction and increased intrahepatic resistance to blood flow will cause hepatic insufficiency and portal hypertension, respectively. There are major clinical complications of cirrhosis, including ascites, renal failure, encephalopathy and variceal bleeding[17]. Further, cirrhosis, of any etiology, is an established cause of HCC. As the incidence of NAFLD continues to increase, the complications of cirrhosis are expected to increase commensurately.

Contrary to previous popular belief, recent evidence showed feasibility of the reversal of fibrosis (including cirrhosis)[19]. It has been shown that removal of the underlying cause of liver injury is often effective treatment of liver fibrosis[20–22,16]. Further, various promising anti-fibrotic drugs are under development and validation[16]. As a result, the accurate diagnosis and staging has great promise to improve the diagnosis, prognosis and treatment monitoring of patients with liver fibrosis.

Liver Iron Overload

A homeostasis of iron in the human body is usually maintained by a regulated dietary absorption of iron and a consistent process of the elimination of iron by a number of spontaneous mechanisms[23]. This homeostasis can be disrupted by increased absorption of iron due to hereditary hemochromatosis and thalassemia, as well as frequent blood transfusions[24]. The result of the disrupted homeostasis is iron overload (increased iron concentration).

The work in this dissertation does not aim to address any difficulties in the diagnosis and evaluation of liver iron overload. However, the presence of iron depending on the cluster size, distribution and concentration greatly alters the signal behavior in MRI. As a result, the effect of iron is a factor that must be accounted for in many applications of MRI to diffuse liver diseases. Further, the increased presence of iron in tissue impacts the ability of CSE-MRI methods to quantify liver fat and must be accounted for in CSE-MRI signal models.

2.2 Diagnosis of NAFLD

Percutaneous liver biopsy is the current gold standard for diagnosing hepatic steatosis. It provides important histological information such as fat content, cellular injury and fibrosis[25,26]. Nevertheless, it suffers from sampling variability and significant risk of complication.

Imaging modalities such as ultrasound and computed tomography (CT) are also sensitive to the liver fat content[27]. However, ultrasound struggles to provide sufficient repeatability and reproducibility[28,29]. Further, the fat content measured in CT is confounded by the effect of local concentrations of iron, copper, etc[30], as well as the use of iodinated contrast. The non-invasive clinical standard method of diagnosing hepatic steatosis is MR spectroscopy (MRS)[27]. MRS measures proton density fat fraction (PDFF) as a quantification of steatosis. MRS acquisitions for liver PDFF quantification can be performed rapidly (e.g.: single breath-hold). However, MRS is challenged by sampling variability since it measures only a single voxel.

In contrast to MRS, chemical shift encoded (CSE) MRI enables rapid and accurate PDFF quantification with whole-liver 3D coverage in a single breath-hold. In recent years, MRI based techniques have been emerging as well validated biomarkers of hepatic steatosis. Extensive validation of confounder-corrected quantitative CSE-MRI has demonstrated equivalence of these methods to MRS[31–36].

2.3 Diagnosis and Staging of Liver Fibrosis

The gold standard for the diagnosis and staging of fibrosis is liver biopsy. Liver fibrosis staging using standardized grading system such as METAVIR has shown good to excellent inter- and intra-observer reproducibility[37]. However, due to a high degree of sampling error, liver biopsy is extremely limited in its reproducibility and reliability. Further, biopsy is associated the risk and dangerous complications (0.13-6.4%)[38].

Among less invasive techniques. Serum bio-markers such as N-terminal propeptide of type III collagen are effective for detecting fibrosis of all stages, but are not effective for the staging of fibrosis[16,39]. Using ultrasound, fibrotic liver will produce a coarse echo pattern which can be used for diagnosis[40]. However, the specificity of ultrasound is limited in the presence of steatosis.

Magnetic resonance elastography (MRE), encodes the periodical displacement into the signal phase, using a propagating mechanical wave induced by a passive transducer. Shear stiffness can be calculated from the wave function, e.g., with a local frequency estimation (LFE) inversion algorithm. The shear stiffness can detect liver fibrosis with high specificity and sensitivity.

However, the staging of fibrosis is less successful[41,42]. When elastography is performed using ultrasound (transient elastography), similar performance was observed[41,43].

Contrast agent Gadoxetic acid uptake is a measure of hepatic function which is impaired by the increase of fibrotic tissue. Liver fibrosis evaluation based on this premise using contrast enhanced MRI has been developed and evaluated[44–47]. Although contrast enhanced MRI was shown to be a promising tool for the staging of liver fibrosis, further technical development is required to reach the accuracy delivered by MRE based on the results in these studies.

Diffusion weighted MRI (DWI) using an intravoxel incoherent motion (IVIM) model has been investigated for the staging of liver fibrosis. This was evidenced by a meta-study of 25 independent studies involving 1833 patients in total. The measured area under the curve (AUC) in summary receive operation curve (SROC) were 0.8554 (F0 vs F1-F4), 0.8770 (F0-F1 vs F2-F4), 0.8836 (F0-F2 vs F3-F4), and 0.8596 (F0-F3 vs F4)[48]. However ADC measurements in the liver demonstrated poor reproducibility across combinations of b-values[49]. Another study came to the same conclusion using weighted mean difference (WMD) analysis[50]. However, the staging by DWI has been less reliable than MRE [44]. DWI based fibrosis staging is challenged by confounding factors including steatosis. Should these confounding factors be addressed, the accuracy of fibrosis staging is likely to improve.

Importantly, an apparent monotonic increase of T_2 with the progression of liver fibrosis has been discovered in recent animal studies[51,52]. This strong correlation between T_2 and the degree of fibrosis level measured using the Ishak classification system reflects the potential of T_2 as a imaging biomarker for the staging of hepatic fibrosis[53]. However, obvious challenges from the effects of iron overload and hepatic inflammation will need to be addressed.

2.4 Quantitative Imaging Biomarkers

MRI-based quantitative imaging biomarkers (QIBs) have tremendous potential in applications pertinent to diffuse liver disease. As described in previous sections, CSE-MRI measured proton density fat fraction (PDFF) has been used as a QIB for NAFLD. DWI (with IVIM) model produced parameters such as perfusion fraction (pf), and T_2 have the potential to be QIBs used for assessing liver fibrosis.

In order for MRI techniques to provide valid QIBs, they should be:

- ***Accurate:*** Correlate with an accepted reference
- ***Precise:*** Repeatability within subjects (low variability)
- ***Reproducible:*** Low variability across sites and platforms

The thesis of this dissertation is to address the challenges in the development and widespread dissemination of MRI based QIBs for diffuse liver diseases.

2.5 PDFF Quantification using CSE-MRI

CSE-MRI

CSE-MRI was first used for the separation of water and fat signal. Due to the relative chemical shift between water and fat, each species signal would contain a relative phase that is a linear function of the echo time. The acquisition can be adjusted such that the relative phase shift between the two chemical species are 0 (in-phase) and π (opposed-phase). By adding and subtracting these two signals, S_W (water) and S_F (fat) can be derived[54]. However, without the knowledge of which chemical species is the major component in a voxel, it is ambiguous which of the S_W and S_F is the summation and which is the subtraction. Both chemical species were assumed to present a single MR spectral peak.

Robust and uniform separation was achieved after measuring and compensating for phase shifts caused by local magnetic field inhomogeneity[55]. To account for the B_0 field inhomogeneity, a version of the following signal model was adopted to model signal acquired at three different echo times.

$$S = e^{i(\gamma \Delta B_0 \cdot TE_n + \phi_0)}(S_W + S_F \cdot e^{i2\pi \cdot f \cdot TE_n}) \quad [2.1]$$

Where γ is the gyromagnetic ratio, ΔB_0 is the local B_0 field inhomogeneity, TE_n is the echo time of the n^{th} echo, and f is the relative chemical shift of fat to water. S_W and S_F denote the magnitude of water and fat signal respectively while ϕ_0 denotes a common initial phase for all the signal.

This update of the signal model introduces the formidable challenge of estimating local B_0 field inhomogeneity to the separation of chemical species. The large spatial variation in B_0 field sometimes encountered in clinical exams will cause spectral alias, resulting in ambiguity in the solution[56,57]. Another source of ambiguity is the scenario where a single chemical species is dominant in a voxel. It could not be determined from the signal model whether the dominant signal is water or fat[56]. Further, iterative reconstruction such as non-linear least square fitting, the non-convexity of the model sometimes causes the reconstruction to converge to a local minimum instead of the desired solution[56].

Various region growing-based[58,59] and multiresolution[60] methods were proposed to solve the ambiguities with varying degrees of success. Alternatively, Hernando et al. proposed a method where a combination of spatially regularized maximum likelihood formulation and a graph cut optimization algorithm resolved ambiguities and non-convexity of the signal model. Robust performance was achieved even in challenging cardiac cases[56].

At this point, despite the successful and unambiguous separation of water and fat signal, important factors that influence the signals such as the coil sensitivity and R2* decay were ignored. This results in the qualitative nature of the produced water and fat signals.

CSE-MRI PDFF as a QIB for Steatosis

After further proposition and validation of more realistic signal models, proton density fat fraction (PDFF) was measured using CSE-MRI[61]. PDFF is defined as the ratio $S_w /(S_w + S_F)$ after correction for all confounding factors discussed in the following paragraphs contributing to the estimated signal intensity denoted as S_w and S_F.

The signals acquired at different echo times experience different amounts of R_2* decay which is ignored by signal model in Eq.2.1. Without modeling the effect of R_2* decay, a bias will arise in the estimate of PDFF[62,63]. In theory, water and fat signals experience R_2* decay at different rates, and a dual R_2* model (independent R2* for water and fat) gives more accurate estimation of PDFF in phantoms[64]. However, in vivo, a single R_2* model results in more accurate PDFF estimates than a dual R2* model, at least in liver applications[65]. Consequently, single R2* signal models have been widely accepted.

The complex structures of triglyceride molecules (fat) give rise to inhomogeneous chemical shift within the molecule. The fat signal was historically modeled as a single MR spectral peak with a chemical shift of 1.3ppm (methylene peak) while the chemical shift experienced by protons in these molecules range from 0.7 to 5.3ppm as measured by MR spectroscopy[66]. Generally, this mismatch between the model and the physical truth causes bias in the PDFF estimate[36,67]. Especially, the double bond peak (5.3ppm) being much closer to the water peak(4.7ppm) than the main fat peak(1.3ppm) will contribute to the estimated water signal instead of fat. This confounding effect was successfully addressed by treating the fat ^{1}H MR spectrum as known a priori measured using MR spectroscopy[36,67].

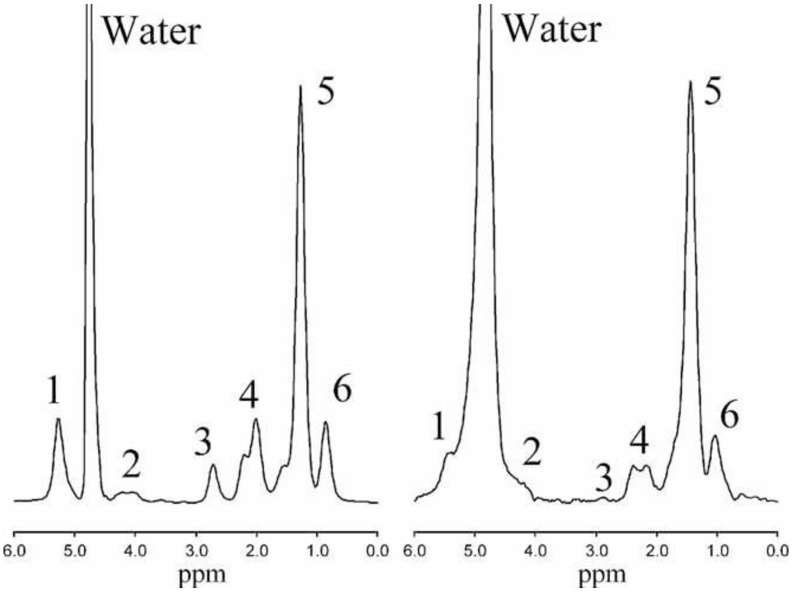

Figure 2.2 The MR spectrum of fat contains multiple peaks, some of which are closer to the water peak than the main fat peak(5). MR spectrum of Microlipid® fat-water emulsion phantom MR spectrum (left) and in vivo liver MR spectrum from a human subject with fatty liver (right). Image from Hamilton et al. NMR Biomed (2010).

Eddy current induced by rapidly changing gradient fields creates a phase shift between signals acquired at different echo times. The bias from this phase shift in PDFF estimate can be removed by utilizing a mixed fitting scheme[68]. Further, the estimated signal intensities S_W and S_F are random variables with skewed non-Gaussian distribution after taking the magnitudes of complex values. This asymmetry will propagate into the bias of PDFF estimate if not dealt with, especially in noisy voxels. A model where a common phase is assumed for the water and fat signal can successfully tackle this effect and produce accurate PDFF estimate[69].

A number of studies have shown that PDFF measured using CSE-MRI (signal model shown in Eq.2.2) after correcting for the confounding effect of R2*, using a multi-peak spectral model of fat, etc. is a valid QIB for hepatic steatosis[31–36,67,70].

$$S(TE_n;\ S_W, S_F, \Delta B_0, R_2{}^*, \phi_0\ ) = e^{i(\gamma\cdot\Delta B0\cdot TE_n)}\cdot e^{-R_2{}^*\cdot TE_n}\cdot e^{i\phi_0}(\ S_W + S_F\cdot\sum_{p=1}^{P} a_p e^{i2\pi\cdot f_p\cdot TE_n}) \quad [2.2]$$

Pre-calibration Spectral Model of Fat

Pre-calibrated multi-peak models have been derived by MRS or dedicated CSE-MRI experiments with a large number of echo times. However, different models including a 9-peak model by Hamilton et al[66]. and a 6-peak model after merging some peaks with very similar resonance frequency[66], a 7-peak model by Ren et al[71]., a 4-peak and a 5-peak model by Wokke et al[72]., and a 3-peak model by Yu et al[67]., have been derived and applied in different studies. The various models differ in the number of peaks, chemical shift between peaks and relative amplitudes of the peaks. Although techniques using different spectral models have been validated for accurate fat quantification or water fat separation, there is no consensus as to which spectral model should be used.

The impact on PDFF estimation from the choice of spectral model of fat is unknown, and this lack of standardization has potential impact on the reproducibility of CSE-MRI for quantifying fat. This work will validate the fat spectral models currently used in CSE-MRI based fat quantification. It will seek to establish how the choice of fat model will affect the accuracy and reproducibility of CSE fat quantification.

T1-related Bias in CSE-MRI PDFF Quantification

In human hepatocytes, the short T_1 of fat can lead to overestimation of the fat signal relative to water signal in CSE techniques based on spoiled gradient echo (SGRE) acquisitions, if the acquisition is T_1-weighted. T_1-independent methods mitigates this overestimation by applying a small flip angle in SGRE acquisitions to approach proton-density weighting[31–33,35]. Flip angles smaller than 5° are usually applied, which unfortunately results in reduced SNR. Thus, if larger flip angles can be used in CSE-MRI without causing T_1-related bias, it is likely that better precision may be achieved, by reducing the variability of individual measurements.

Instead of T_1-independent methods, T_1 can be measured from signals acquired at multiple flip angles, then used to correct T_1 weighting in water and fat estimates. Based on DESPOT1 by Denoi et al[73]., Liu et al first proposed a dual flip angle method which combines a 3-point Dixon method and DESPOT1. This approach acquires multi-echo SGRE signal and estimates water and fat at two different flip angles respectively[69]. DESPOT1 was performed to produced T_1-corrected water, fat signals as well as T_1 of water and fat. Dual flip angle methods allow the choosing of larger flip angles and thus higher SNR in acquired signal without inducing T_1-related bias in PDFF estimate. At the same time, the additional parameters to estimate (T_1 of water and fat) offsets some of the SNR benefit of utilizing the magnetization more efficiently.

In Liu's method, R_2* and B_0 field inhomogeneity were estimated repeatedly at 2 different flip angles. This redundancy of parameters is likely to impair the noise performance. It is therefore expected that by applying the constraint that R_2* and B_0 field inhomogeneity remain unchanged between scans at each flip angle, less noisy unbiased estimate of PDFF may be achieved as well as estimates of R_2* and T_1. Based on this hypothesis, in this thesis we will propose a joint fit approach for T_1 corrected fat quantification based on dual flip angle multi-echo SGRE acquisition.

2.6 Quantitative Diffusion MRI for the Staging of Fibrosis

Quantitative Diffusion MRI

The thermodynamics of homogeneous particles going through Brownian motion (diffusion) was theorized by Albert Einstein. An important conclusion[74] is that unrestricted diffusion can be described by Eq.2.3.

$$\mathrm{r_{rms}} = \sqrt{2\mathrm{Dt}} \qquad [2.3]$$

Where $\mathrm{r_{rms}}$ the root-mean-squared displacement is a function of diffusion time (t) and diffusion coefficient (distance squared per time with the unit mm^2/s).

Torrey first modeled the effect of diffusion on magnetization in nuclear magnetic resonance (NMR) by adding a diffusion term into the Bloch Equations[75]. Stejskal and Tanner, at the University of Wisconsin, later used a diffusion sensitizing gradient to measure the diffusion coefficient[76] (D) described in the Einstein equation (Eq.2.4). The signal encoded using the diffusion sensitizing gradient were modeled based on Torrey's work as:

$$\mathrm{S} = \mathrm{S_0}\ \mathrm{e}^{-\mathrm{bD}} \qquad [2.4]$$

where S is the signal measured with diffusion sensitizing gradient and S_0 is the theoretical signal intensity if no diffusion sensitizing gradient was added. The parameter b commonly referred to as the "b-value", defines the diffusion weighting, which changes with the shape, intensity, spacing and duration of the diffusion sensitizing gradient. The diffusion sensitizing gradient are sometimes referred to as diffusion encoding gradient as well as diffusion weighting gradient.

For a diffusion sensitizing gradient with rectangular gradient lobes, the b-value can be calculated as follows[74]:

$$\mathrm{b} = \gamma^2 \mathrm{G}^2 \delta^2 (\Delta - \delta/3) \qquad (2.5)$$

where γ is the gyro magnetic ratio, G is the gradient strength, Δ and δ are the spacing and duration of diffusion sensitizing gradient lobes.

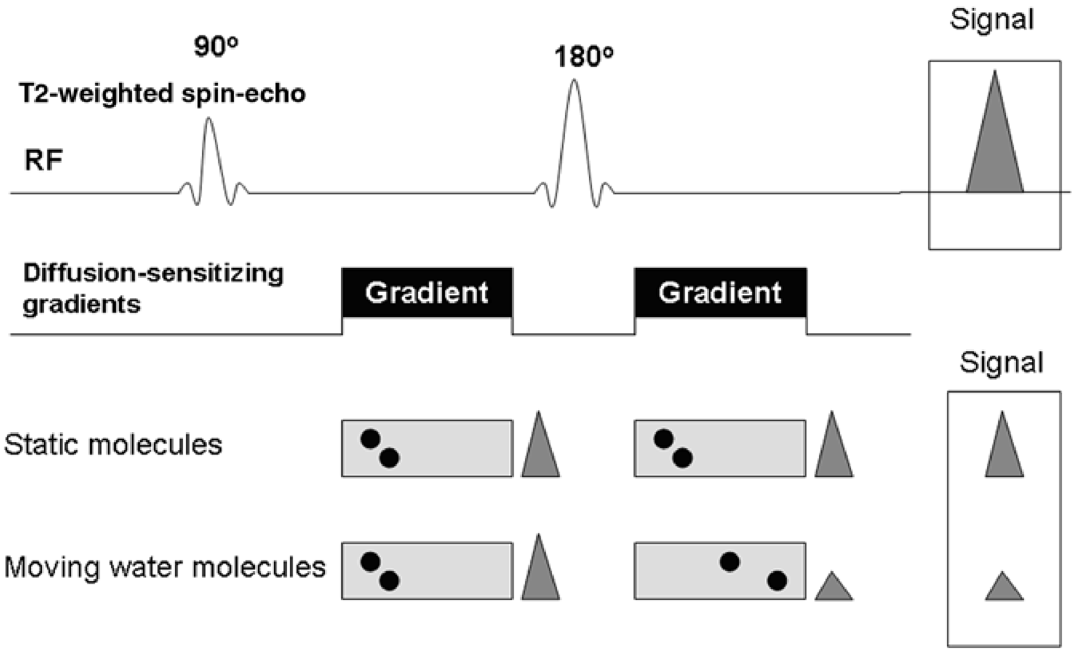

Figure 2.3. Spin-echo based pulse sequence diagram for diffusion MRI. Image from Koh et al. AJR (2007).

The signal model in Eq.2.4 is derived with the assumption of unrestricted homogeneous single component diffusion. With such an assumption, particle displacement after a fixed duration of Brownian motion follows a Gaussian distribution. As a result, such diffusion activity is also called Gaussian diffusion. Unfortunately, in the in vivo environment, unrestricted, homogenous, single component diffusion activity is not a realistic assumption. The term apparent diffusion coefficient (ADC) was therefore coined to describe the number measured using Eq.2.4 from more complicated diffusion activity. Therefore, we can rewrite Eq.2.4 as:

$$S = S_0\, e^{-b \cdot ADC} \qquad [2.6]$$

An IVIM (intravoxel incoherent motion) model was also proposed by Le Bihan et al[77].,which better approximates the physiological reality in vivo including in the presence of liver fibrosis. The signal was modeled to be a sum of perfusing and diffusing components. Three parameters are used to model this mix of perfusion and diffusion activity: perfusion-related diffusion (D*), perfusion fraction (pf) and pure molecular diffusion (D)[77,78]. Great potential was shown for the IVIM model to accurately evaluate the severity of liver fibrosis[48,50].

The pure molecular diffusion (D) is the parameter less associated with the development of fibrosis in the IVIM model. However, the accurate measurement of ADC as a QIB from diffusion MRI is critical in the measurement of perfusion-related diffusion (D*) and perfusion fraction (pf). This is due to the fact that IVIM signal model is equivalent to a compound of 2 components experiencing unrestricted diffusion described by Eq.2.6.

Challenges in Quantitative Diffusion MRI

Reported measures of diffusivity such as ADC from different studies have shown significant variability. For instance, reported ADC in healthy liver and liver lesions vary widely across studies[49,79–84], with clinically relevant overlap in values : normal liver (0.69-1.83 $\times 10^{-3}$mm^2/s), metastases (0.94-1.50 $\times 10^{-3}$mm^2/s), HCC (0.97-1.38 $\times 10^{-3}$mm^2/s), hemangiomas (1.90-2.95 $\times 10^{-3}$mm^2/s), cysts (2.54-3.63 $\times 10^{-3}$mm^2/s). This wide variability of ADC has precluded the standardization of diagnostic and treatment criteria and the adoption of these techniques for multi-center clinical trials and widespread clinical use, because the overlap of ADC values precludes the use of ADC to differentiate lesion type.

Bulk motion also introduces significant artifacts in DW-MRI and bias in measurement of diffusivity (ADC)[85–92]. These effects are particularly severe in the left liver lobe[93]. The presence of liver fat is extremely common and may affect liver diffusion measurements. Prior studies show contradictory results on the way presence of fat biases measured ADC[94,95] . Hansmann et al. and Taviani et al. have also shown the potential confounding effect of liver fat on ADC[96,97]. Finally, in vivo validation of the technical accuracy (i.e.: lack of systematic error) of quantitative diffusion MRI techniques is challenging, due to the lack of a direct reference standard. Rather, technical accuracy can be assessed using phantoms with highly controlled diffusion properties[98–100]. In vivo, validation of clinical accuracy (e.g.: correlation with treatment prognosis) can be employed as a surrogate for technical accuracy.

Phantoms in Quantitative Diffusion MRI

Development, validation and quality assurance of quantitative diffusion MRI can greatly benefit from highly controlled testing on diffusion MRI phantoms. Early phantoms used in diffusion-MRI were constructed using various pure substances. Compounds such as water[101], ethanol and isopropanol[102], corn oil[103], acetone[104], silicone oil[105] and cyclohexane[103] were proposed and tested. These phantoms are easy to construct, and provide simple diffusion behavior. However, some of these compounds possess multiple MR spectral peaks (ethanol), which may cause ghost images in diffusion weighted echo-planar imaging (DW-EPI). Very importantly, a very limited number of discrete ADC values can be achieved using these pure substances. Therefore, these early phantoms are generally not adequate for validation of diffusion MRI techniques.

Instead of pure substance phantoms, several solution-based phantoms have been proposed in recent years. In these phantoms, a solvent provides MRI signal, and its diffusion behavior is modified (resulting in progressively lower ADC) by adding various concentrations of a solute. Two important examples of solution phantoms include designs based on solutions of water with sucrose[100,106] or polyvinylpyrrolidone (PVP)[98]. It has been shown that dissolved sucrose or PVP reduces the measured ADC of water, enabling the design of phantoms with the desired ADC values[98,100,106]. Note that, in general, solutes such as sucrose and PVP dissolved in water generate

MR signals with multiple spectral peaks. Although preliminary studies have examined the Gaussian diffusion properties of sucrose phantoms[98,100,106–108], comprehensive validation of these phantoms is still needed. For instance, it is unknown whether the signal from PVP or sucrose could confound ADC values measured with quantitative diffusion MRI techniques. Further, an ice-water bath is typically used to maintain a constant temperature[99] while scanning phantoms with diffusion MRI. The use of water as a signal source results in limited range of ADCs at ice water temperature ($ADC<1.1 \cdot 10^{-3}$ $mm^2 \cdot s^{-1}$)[109] which is well below the higher end of physiological values ($2.6 \cdot 10^{-3}$ $mm^2 \cdot s^{-1}$)[110]. This limited ADC range is a fundamental limitation of phantoms based on water as a solvent. Although scanning at higher temperatures (eg: room temperature) is possible, and will lead to higher ADC values, the requirement of accurate temperature control makes the experiments complicated. For the purpose of reaching the entire physiological ADC range, in this work we propose, develop and validate a phantom based on the mixture of acetone and deuterium oxide.

2.7 T_2 Quantification for the Staging of Liver Fibrosis

Lengthy exam times have been a challenge to commercially available single-echo spin-echo and multi-echo spin-echo T_2 mapping techniques. This is due to the fact that long TR is required for reducing the T_1 weighting in the signal. To avoid motion artifacts, respiratory motion in abdomen exams needs to be addressed. A common solution is to acquire the images in a breath-hold. As a result, to the best of our knowledge, multi-slice multi-echo spin-echo is the only spin-echo based T_2 mapping method applicable in the abdomen[52,111]. This technique does not cover the entire liver in a single breath-hold.

Steady-state based T_2 mapping technique has vastly reduced the exam time required for T_2 mapping. Driven equilibrium single pulse observation of T_1 and T_2 (DESPOT2)[112] is based on 2 separate SGRE acquisitions and a balanced-steady state free precession (b-SSFP) with varied T_1 and T_2 weightings. This technique requires 3 separate steady-state acquisitions and may be confounded by banding artifact. Whole liver T_2 mapping in a breath-hold is therefore not feasible.

Double echo steady-state (DESS)[113], and triple echo steady-state (TESS)[114] methods encode varied T_2 and T_1 weighting into separate echoes acquired in a single steady-state acquisition. Although T_2 can be calculated from a single steady-state acquisition, this method is not readily compatible with CSE-MRI due to the different compositions of signal echoes. When imaging livers with steatosis, the presence of fat and the difference between T_2 of water and fat[66] may have a confounding effect on the estimate of T_2. Further, T_2 is heavily influenced by the local iron concentration[115], for T_2 to provided dedicated information to the staging of fibrosis, it is critical to account for the contribution of iron. Both steatosis and iron concentration can be evaluated with CSE-MRI[23,33]. The inability to acquire TESS and DESS signal in a combined acquisition with CSE-MRI is a challenge in the T_2-based staging of liver fibrosis.

The steady-state methods introduced above exploit only the magnitude for the encoding of relaxation parameters. The signal phase was discarded as redundant information. In this work we propose a novel T_2 mapping mechanism by encoding T_2 information into the signal phase of steady-state signal acquired with RF phase increments[116]. The use of phase may reduce the number of acquisitions required in DESPOT2. The use of steady-state signal similar to an SGRE signal also makes the proposed technique compatible with CSE-MRI in the form of a multi-echo acquisition. The proposed technique may potentially enable the T_2-based staging of liver fibrosis.

2.8 Significance

CSE-MRI PDFF quantification is a proven QIB for hepatic steatosis. Accurate diagnosis and grading of NAFLD followed by treatment of lifestyle intervention can prevent the progression of NAFLD into more dangerous liver diseases and improve the quality of life. Further, CSE-MRI PDFF quantification due to its non-invasive nature and robustness to the heterogeneity of steatosis can be used to monitor treatment response either by lifestyle intervention or insulin sensitizing drugs.

In this work, the evaluation of pre-calibrated fat NMR spectrum used in CSE-MRI will provide necessary information to the design of standardized CSE-MRI protocol for accurate assessment of hepatic steatosis. The development of T_1-corrected CSE-MRI PDFF quantification technique may improve the SNR in the PDFF estimate and consequently the precision in the assessment of NAFLD.

Recent studies have indicated the feasibility of reversing even advanced fibrosis by removing the cause e.g. HBV, HCV, NASH, and alcohol abuse. The staging of liver fibrosis can provide vital information to the design of treatment plan and the monitoring of treatment response.

In this work, the development of a diffusion phantom with controlled temperature and a wide range of tunable ADC values may help address the confounding factors that caused the wide variability of ADC measurements by diffusion MRI. The improved diffusion MRI techniques may further improve the accuracy and precision of IVIM model used in the staging of hepatic fibrosis.

Finally, the development of a phase-based T_2 mapping technique potentially compatible with CSE-MRI may enable T_2 mapping of the liver tissue. The T_2 information combined with simultaneous derived PDFF and iron concentration could provide a promising alternative tool for the staging of liver fibrosis.

Chapter 3 : Sensitivity of Chemical Shift-Encoded Fat Quantification to Calibration of Fat MR Spectrum

This work has been published in the *Magnetic Resonance in Medicine*.2015;75(2):845-854 under the title "Sensitivity of Chemical Shift-Encoded Fat Quantification to Calibration of Fat MR Spectrum"

3.1 Abstract

Purpose: To evaluate the impact of different fat spectral models on proton density fat-fraction (PDFF) quantification using chemical shift-encoded (CSE) MRI.

Material and Methods: Both simulations and in vivo imaging were performed. In a simulation study, spectral models of fat were compared pairwise. Comparison using both magnitude fitting and mixed fitting was performed over a range of echo times and fat fractions. In vivo acquisitions from 41 patients were reconstructed using 7 published spectral models of fat. T_2-corrected STEAM-MRS was used as reference.

Results: Simulations demonstrate that imperfectly calibrated spectral models of fat result in biases that depend on echo times and fat fraction. Mixed fitting is more robust against this bias than magnitude fitting. Multi-peak spectral models showed much smaller differences among themselves than when compared to the single-peak spectral model. In vivo studies show all multi-peak models agree better (for mixed fitting, slope ranged from 0.967-1.04 using linear regression) with reference standard than the single-peak model (for mixed fitting, slope=0.76).

Conclusion: It is essential to use a multi-peak fat model for accurate quantification of fat with CSE-MRI. Further, fat quantification techniques using multi-peak fat models are comparable and no specific choice of spectral model is shown to be superior to the rest.

Keywords: fat quantification; spectral model of fat; proton density fat fraction; fat spectrum; non-alcoholic fatty liver disease; magnetic resonance imaging

3.2 Introduction

Non-alcoholic fatty liver disease (NAFLD) is the most common chronic liver disease, affecting up to 30% of the adult U.S population[2]. NAFLD is a risk factor for diabetes and cardiovascular disease, and can progress into cryptogenic cirrhosis and hepatocellular carcinoma[117,118]. The diagnosis of NAFLD requires assessment of intracellular triglycerides in hepatocytes. Chemical shift-encoded (CSE) water fat imaging enables accurate quantification of proton density fat fraction (PDFF) over the entire liver. Compared with liver biopsy and single voxel MR spectroscopy (MRS)[119], CSE-MRI provides non-invasive spatially resolved quantification of liver fat. 3D coverage of the entire liver can be acquired within a single breath-hold[27,31–33]. Extensive validation of confounder-corrected quantitative CSE-MRI have demonstrated equivalence of these methods to MRS[31–36].

In CSE-MRI, multiple images are acquired with increasing echo time (TE). A water image (W) and a fat image (F) are calculated by fitting the acquired data at each voxel to a signal model based on the chemical shift between fat and water[31,33]. Fat fraction is then calculated as F/(W+F). To ensure that the calculation yields proton density fat-fraction (PDFF), a fundamental property of tissue that reflects the concentration of triglycerides[61], several confounding factors must be addressed. Such confounders include B_0 inhomogeneity[120], T_1 bias[62,69], T_2* signal decay[67,121–123], eddy currents[68,124], noise bias[69], and the spectral complexity of fat[123,125].

Compared with water, which has a single spectral peak, the complex structure of triglyceride molecules leads to complex and heterogeneous proton chemical shifts within the molecule. The different chemical shifts observed in a number of functional groups in fat molecules give rise to multiple peaks of fat signal in proton-based MRI. In early CSE-MRI techniques, a single-peak fat model (methylene peak) was generally assumed. However, this single-peak model accounts for only 70% of the total fat protons[66]. A recent study showed that the single-peak model results in a biased estimate of PDFF that can be corrected by using a multi-peak spectral model of fat[125]. In principle, the use of such a model requires independent estimation of the amplitude (and potentially other spectral parameters) of every fat peak. However, due to limited number of echo times typically acquired in CSE-MRI, it is not possible to individually resolve each fat peak. Consequently, CSE-MRI using a pre-calibrated multi-peak fat spectral model have been proposed[62,67,125], where the relative amplitudes and chemical shift of fat peaks are known parameters. Therefore, compared with the single-peak model, no additional variables (degrees of freedom) are introduced into the estimation problem.

Pre-calibrated multi-peak models have been derived by MR spectroscopy or using dedicated CSE-MRI experiments with a large number of echo times[66,67,71]. However, different models have been derived and applied in different studies. The various models differ in the number of peaks, chemical shift between peaks and relative amplitudes of the peaks. Although techniques using different spectral models have been validated for accurate fat quantification or water fat separation, there is no consensus as to which spectral model should be used.

The impact on PDFF estimation from the choice of spectral model of fat is unknown, and this lack of standardization has potential impact on the reproducibility of CSE-MRI for quantifying fat. The purpose of this study is to evaluate the sensitivity of PDFF mapping to the choice of multi-peak fat model by simulation and in vivo liver fat quantification.

3.3 Theory

In chemical shift-encoded (CSE) MRI, the acquired signal in a voxel in the presence of water and fat can be generally described as:

$$s_n = e^{i(\Delta\omega_0 \cdot TE_n)} \cdot \left(We^{i\phi_{0,w}} e^{-R_{2w}^{*} \cdot TE_n} + Fe^{i\phi_{0,F}} \cdot \sum_{p=1}^{P} \alpha_p e^{i2\pi \cdot f_p \cdot te_n} e^{-R_{2p}^{*} \cdot TE_n} \right) \qquad [3.1]$$

where s_n is the signal acquired at the n^{th} echo time TE_n, $\Delta\omega_0$, is the frequency offset due to local B_0 off-resonance $\phi_{0,w,}$ $\phi_{0,F}$ are the initial phase of water and fat signal. The signal consists of one water peak and P fat peaks. W and F are the sum of all water signal and fat signal, respectively. The R2* decay rate of water is $R_{2W}*$. The relative amplitude, relative frequency shift, and R_2* decay rate of the p^{th} fat peak are denoted as α_p, f_p and R_2*_p, respectively. In general, $\phi_{0,w,}$ $\phi_{0,F}$, $\Delta\omega_{0,}$ $R2_W*$, $\alpha_1 \ldots \alpha_P$, $f_1 \ldots f_P$, $R_2*_1 \ldots R_2*_p$ are the unknown parameters to be estimated.

In CSE-MRI, due to imaging time constraints, 6 echoes with maximum echo time of approximately 10-20ms (at 1.5T) are typically acquired, providing limited spectral resolution. To achieve robust water fat separation, the number of unknowns can be reduced by introducing assumptions to the general signal model in Eq.3.1. Two major and well-validated assumptions are commonly used 1) R_2* of water and all fat peaks are all assumed to be equal[31,65], 2) the relative amplitude and chemical shift of all fat peaks are assumed to be known a priori[67,125] (i.e. pre-calibrated fat spectrum). These assumptions lead to the following simplified signal model[124]:

$$s_n = e^{i(\Delta\omega_0 \cdot TE_n)} \cdot \left(We^{i\phi_{0,w}} + Fe^{i\phi_{0,F}} \cdot \sum_{p=1}^{P} \alpha_p e^{i2\pi \cdot f_p \cdot te_n} \right) e^{-R_2^{*} \cdot TE_n} \qquad [3.2]$$

where α_p, f_p are the known (ie: pre-calibrated) relative amplitude and frequency shift of the p^{th} fat peak. In a typical CSE-MRI acquisition, signals from multiple echoes acquired are fit, on a voxel-by-voxel basis, using the signal model in Eq.3.2 to estimate the six unknown parameters W, F, $\phi_{0,w}$ and $\phi_{0,F}$, $\Delta\omega_0$, and R_2*. A PDFF map then can be calculated using separated water and fat images, including correction for noise bias effects[69]. This signal model has been successfully applied for PDFF quantification, and validated using MR spectroscopy-based fat quantification as a reference[31,33].

Further, eddy current effects can lead to undesired phase shifts between different echoes, introducing errors in CSE fat quantification. To address this challenge, fitting is often performed after taking magnitude of both sides of Eq.3.2, i.e.: “magnitude” fitting. When the phase in equation 2 is preserved, this is referred to as “complex” fitting. Magnitude fitting is relatively immune to eddy current related phase errors but suffers reduced noise performance compared with complex fitting[126]. Alternatively, a mixed fitting technique has been proposed where only the phase of the first echo is discarded in “single echo train” acquisitions. Mixed fitting results in good robustness to phase errors relative to complex fitting, and improved noise performance relative to magnitude fitting[68].

The specific choice of pre-calibrated multi-peak fat model differs considerably between studies and there is no consensus as to which is the best and most appropriate spectrum to use. In recent works, Hamilton et al, measured the human liver fat spectrum as a 6-peak and a 9-peak model using spectroscopy on a 3T GE system[66]. Ren et al, characterized the human subcutaneous and bone marrow fat spectrum using a 7-peak model, measured at 7T, using single-voxel stimulated echo acquisition mode (STEAM)-spectroscopy[71]. Wokke et al[72], derived 4- and 5-peak fat models by merging peaks that are close together in the 6-peak model[64]. Yu et al[67], applied a self-calibrated fat quantification method which calibrated human liver fat spectrum as a 3-peak model.

The differences in number of peaks, frequency shifts relative to water, and relative amplitudes are summarized in Table 1. Among these fat models, 6,7 and 9-peak models are most commonly used in CSE fat quantification. The 9-peak model has been adopted by Berglund et al[127], 6-peak model has been adopted by Hernando et al[123], Hines et al[31], Meisamy et al[33]. The 7-peak model has been used by Jonker et al[128]. An additional 3-peak model and 5-peak model have also been reported by Yokoo et al[32,34].

Peaks	Frequency relative to water (ppm)	Relative amplitude (%)	Reference
1	-3.4	100	n/a
3	0.73, -2.49, -3.29	8, 17, 75	Yu (17)
4	0.73, -2.49, -3.27, -3.68	8, 15, 72, 4	Wokke (26)
5	0.73, -2.35, -2.54, -3.27, -3.68	8, 5, 10, 72, 4	Wokke (26)
6	0.6, -0.5, -1.95, -2.6, -3.4, -3.8	4.7, 3.9, 0.6, 12, 70, 8.8	Hamilton (22) Hernando (18) Meisamy (6) Hines (7)
7	0.61, -1.93, -2.45, -2.67, -3.11, -3.4, -3.8	4.2, 1.5, 6.6, 9.6, 7.1, 62.7, 8.3	Ren (23), Jonker (28), Zhong (10)
9	0.59, 0.49, -0.5, -1.95, -2.46, -2.68, -3.1, -3.4, -3.8	3.7, 1, 3.9, 0.6, 5.8, 6.2, 5.8, 64.2, 8.8	Hamilton (22), Berglund (27)

Table 3.1 List of different multi-peak spectral models of fat used in this work.

3.4 Methods

Simulations

As part of a computer simulation, each spectral model of fat was compared with all other models in a pairwise manner. Specifically, one model was used to generate a test signals (as the "true" fat model) at each TE, and the other spectral model (as the estimator fat model) was used to fit the test signals to estimate PDFF. All frequencies are based on 1.5T imaging. Each test signal was generated using the signal model in Eq.3.2 for simulated voxels, which have fat fraction ranging from 1% to 40%, and a fixed R2* of $40s^{-1}$ (typical for 1.5T liver imaging[129]). Signals were generated with no noise added for 6 echo times, starting at 1.2ms, and spaced by 2.0ms. The initial phase of water and fat was assumed 0, and the initial field inhomogeneity was 2ppm. No eddy current induced phase was added to the first echo. Nevertheless, the phase of the first echo was discarded for both the magnitude and mixed fitting algorithms to better approximate the in vivo situation[68,126].

The PDFF was estimated by fitting the test signals to equation 2 using both magnitude and mixed fitting algorithms, using a different signal model as the estimator fat model. The estimated PDFF was then compared to the true PDFF using linear regression to determine the bias. This simulation was performed for all possible pairs of the fat models listed in Table 1.

Next, the effect of the choice of echo times on the PDFF bias caused by multi-peak model mismatch was also evaluated using simulations. Each combination contains 6 echoes with initial echo time (TE_{min}) and echo spacing (ΔTE) both ranging from 0ms to 3ms. For this simulation, the fat fraction was 30%, R2* = $40s^{-1}$, field strength 1.5T. Signal was generated using 6-peak model as the “true” fat model and PDFF was estimated with 1, 3, 5, 7, 9-peak models. No noise was added to the test signals since we were evaluating the effects of bias in these simulations. Bias was calculated for each echo combination studied.

In Vivo Liver Fat Quantification

In vivo liver datasets from 41 patients were also analyzed. Data acquisition was performed on GE Signa HDxt 1.5T scanners, with either an 8-channel cardiac coil or an 8-channel torso coil. This dataset has been analyzed by previous studies[31,33] for different purposes, but reprocessed specifically and uniquely for this study.

CSE data were obtained using an investigational version of a multi-echo spoiled gradient echo (SGRE) sequence. All images were acquired in axial plane and obtained during a single 21s breath-hold, with the following imaging parameters: readout direction R/L, matrix size 256×128, 2D parallel imaging with an effective reduction factor of 2.2 slice thickness 10mm, 24 slices, flip angle 5°, TR=13.7-14.9ms, BW=±125kHz, mono-polar readout (flyback gradients), 6 echoes, TE_{min}=1.2ms,ΔTE=2.0ms. PDFF maps using the multi-echo SGRE data were reconstructed twice using each fat model listed in Table 1, once using magnitude fitting and once using mixed fitting algorithms, respectively for a total of 14 reconstructions for each dataset. Due to eddy current induced phase, pure complex fitting was not performed since phase shifts on the first echo caused by eddy currents were known to create bias. T_1 bias was minimized by using a low flip angle and by performing a retrospective T_1 correction for any residual T_1 related bias[31,130] assuming a T_1 of 568ms for water and 343ms for fat[131].

A single voxel STEAM-MRS spectrum was also acquired in a single breath-hold in every subject to provide a reference standard for fat fraction[121]. MRS data were acquired in the right lobe of liver during a 21s breath-hold at 5 echo times (10, 20, 30, 40, 50 ms) enabling T_2 correction. Typical voxel size was 20 × 20 × 25 mm^3, TR=3500ms, 2048 readout points, 1 average, and spectral width = ±2.5 kHz. MRS-PDFF was estimated from STEAM data using AMARES fitting in jMRUI, with correction of T_2 decay, and prior spectral knowledge[132,133].

For each patient, a region-of-interest (ROI) was co-localized with the STEAM voxel in the slice closest to the center of STEAM voxel. The PDFF was measured in a 20 x 20 mm^2 voxel and the two adjacent slices to match the STEAM voxel closely. MRI-based PDFF was then calculated by averaging the PDFF values within the three ROI's. This procedure was repeated for reconstructions using each spectral model of fat and fitting algorithms. The same ROI's were used for all reconstructions of the same patient to achieve perfectly co-registered MRI-PDFF values.

For each patient, 14 generated MRI-based PDFF values were linearly regressed against STEAM PDFF. 95% confidence intervals and p-values were generated from applying a t-test to the estimate of slopes and intercepts to determine whether slopes are significantly different from 1 and intercepts are significantly different from 0 (i.e.: $p_{slope}<0.05$ or $p_{intercept}<0.05$).

3.5 Results

Simulations

In pairwise comparisons, for each pair of spectral models of fat, estimated PDFF was linearly regressed against true PDFF with excellent correlation ($r^2 > 0.998$) as expected. Thus, slopes close to 1 and intercepts close to 0 reflect equivalence between compared models. In Figure 3.1, A) C) show slopes in comparison of each pair of spectral models when magnitude fitting (A) and mixed fitting (C) were used as fitting algorithms. Each row shows the slope between a particular spectral model ("true" fat model) and every other model (estimator fat model) in each column. Between a single-peak model and any multi-peak model, great errors were observed between estimated fat fraction and true fat fraction (slope< 0.79 or slope>1.22, |intercept| up to 1.2% for mixed fitting, slope<0.82 or slope>1.15, |intercept| up to 1.5% for magnitude fitting). Between any two multi-peak models, improved agreement was demonstrated: 0.94<slope<1.03, -0.5%<intercept<0.1% for mixed fitting, 0.89< slope<1.08, -0.4%<intercept<0.6% for magnitude fitting.

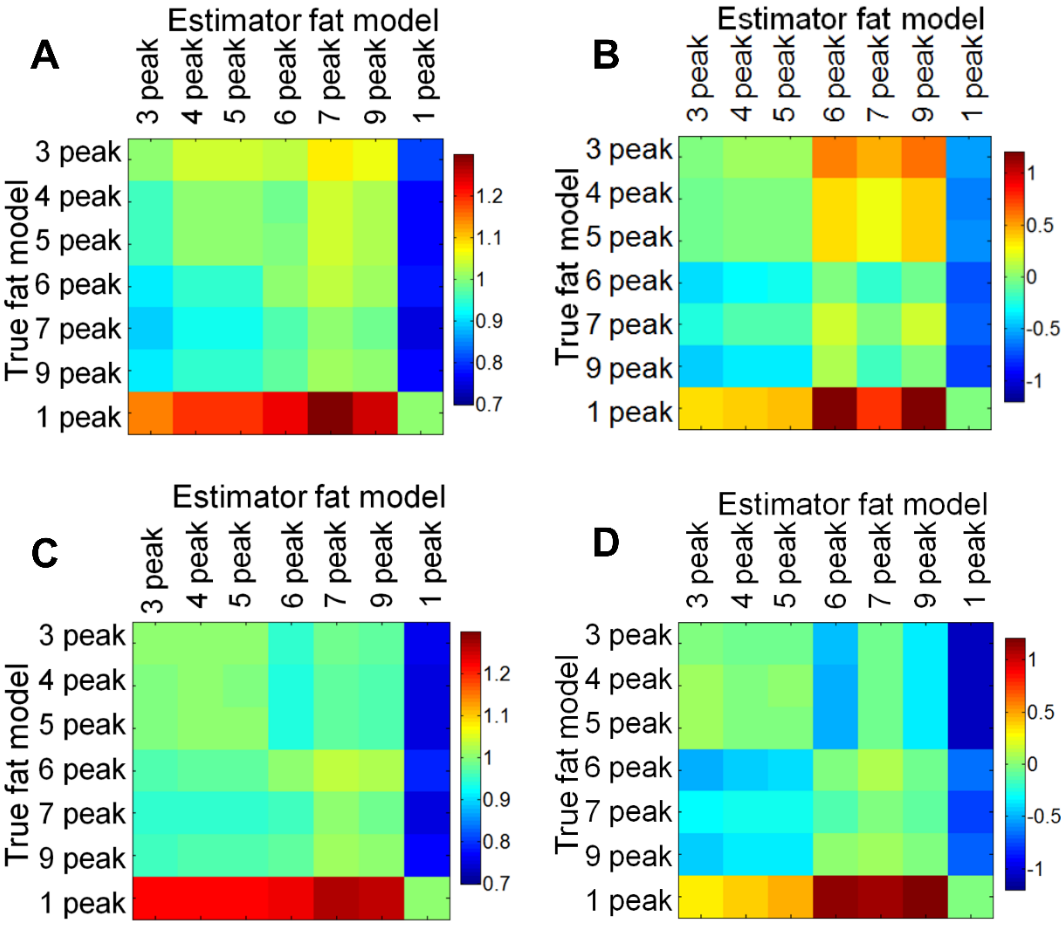

Figure 3.1 Multi-peak models demonstrate better agreement with each other than with the single peak spectral model of fat. Results are from simulations comparing, in a pairwise manner, different spectral models of fat. The color coding plots the slope (A, C) and intercept (B, D) from linear regression of estimated PDFF with true fat fraction, for magnitude fitting (A,B) and mixed fitting (C, D).

Figure 3.2 presents simulation results for the absolute bias in estimated PDFF over a range of initial echo times and echo spacings. Horizontal and vertical axes show echo spacing and initial echo times, respectively. The top row was reconstructed using mixed fitting and the bottom row was reconstructed using magnitude fitting. A clear dependence of bias on echo combination is seen for both fitting algorithms. For magnitude fitting, there is a range of echo combinations (near

TE_{min}=1.25ms, ΔTE=2.3ms) that result in over 10% absolute bias regardless of the fat model used in estimation. For mixed fitting, the bias changes more gradually with echo times, and remains relatively low for lower initial echo times and echo spacings.

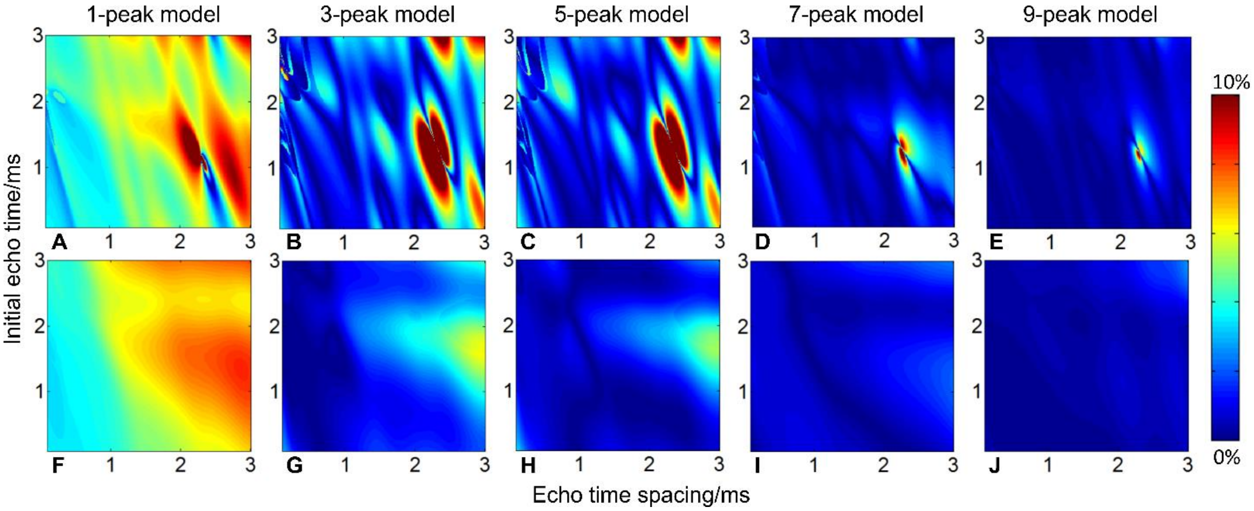

Figure 3.2 In general, mixed fitting has lower bias than magnitude fitting and is less sensitive to the choice of spectral model of fat. Absolute biases from simulated PDFF estimate resulting from difference between "true" fat model (6-peak model) and estimator fat model (1-, 3-, 5-, 7-, 9-peak models) are presented for magnitude fitting (A, B, C, D, E) and for mixed fitting (F, G, H, I, J). The bias is shown to be a function of echo times. For certain echo time combinations, magnitude fitting can lead to large bias (>10%) even from small model differences, while mixed fitting had lower bias. particularly for 7-peak and 9-peak models

In Vivo Liver Fat Quantification

Figure 3.3 shows representative PDFF maps of a patient calculated using several spectral models of fat, for both mixed fitting and magnitude fitting algorithms. A clear PDFF offset can be observed between reconstructions using single-peak model and multi-peak models. Over all patients, linear regression showed strong correlation between STEAM PDFF and all MRI-based PDFF values (r^2>0.962). Further, slopes and intercepts of these regressions were calculated and are shown in Table 3.2, including the 95% confidence intervals and p-values generated from t-tests. Multi-peak models with both fitting algorithms exhibit better agreement with the MRS as reflected by the values of slopes and intercepts. Only 1-peak ($p_{slope}=1.6 \cdot 10^{-15}$ in magnitude fitting $p_{slope}=3.2 \cdot 10^{-16}$ in mixed fitting) model and 7-peak ($p_{slope}=0.04$ in magnitude fitting and mixed fitting) models were significantly different from the reference. Despite being significantly different from the reference, 7-peak model has much closer agreement with the reference than single–peak model (slope=1.046 compared with 0.76 for single-peak model).

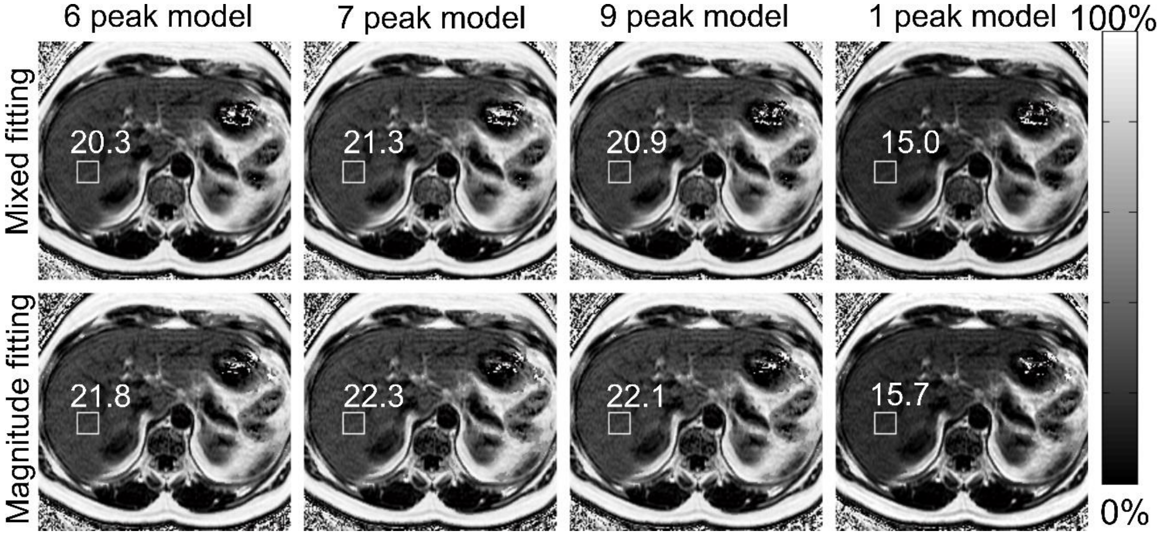

Figure 3.3 Single-peak model produced substantially different liver fat fraction using 6-, 7-, and 9-peak spectral models of fat. PDFF maps from one patient reconstructed using mixed fitting (top row) and magnitude fitting (bottom row) for 4 different spectral models of fat. T_2-corrected STEAM MRS-PDFF was 20.9% in this patient. The location of the steam voxel and Co-localized MRI-PDFF measurements are shown in the figure.

	R^2	**Slope** [95th CI]	p-value (slope)	**Intercept** (%) [95th CI]	p-value (intercept)
Magnitude Fitting					
1-peak	0.974	0.770 [0.726, 0.814]	$3.755 \cdot 10^{-13}$	-0.406 [-0.891, 0.078]	0.098
3-peak	0.962	0.952 [0.900,1.004]	0.068	-0.284 [-0.852, 0.284]	0.318
4-peak	0.974	0.967 [0.916,1.019]	0.210	-0.295 [-0.868, 0.278]	0.304
5-peak	0.974	0.967 [0.916, 1.019]	0.214	-0.293 [-0.866, 0.279]	0.307
6-peak	0.978	1.035 [0.979, 1.091]	0.219	-0.282 [-0.907, 0.334]	0.357
7-peak	0.977	1.060 [0.988, 1.109]	0.041	-0.287 [-0.912, 0.349]	0.372
9-peak	0.970	1.050 [0.993, 1.107]	0.083	-0.287 [-0.914, 0.339]	0.360
Mixed Fitting					
1-peak	0.978	0.760 [0.723, 0.797]	$4.996 \cdot 10^{-15}$	-0.421 [-0.830, -0.012]	0.044
3-peak	0.979	0.967 [0.920,1.013]	0.151	-0.317 [-0.829, 0.194]	0.217
4-peak	0.979	0.975 [0.929,1.021]	0.281	-0.326 [-0.838, 0.185]	0.205
5-peak	0.979	0.975 [0.929,1.022]	0.292	-0.324 [-0.835, 0.188]	0.209
6-peak	0.982	1.008 [0.964, 1.053]	0.703	-0.373 [-0.864, 0.118]	0.133
7-peak	0.983	1.047 [1.001, 1.092]	0.044	-0.313 [-0.813 0.188]	0.214
9-peak	0.981	1.045 [0.997, 1.092]	0.063	-0.358 [-0.880 0.164]	0.174

Table 3.2 All multi-peak fat models agree closely with the reference standard (MRS-PDFF), as evidenced by regression results. Results of the linear correlation of MRI-PDFF and MRS-PDFF are tabulated for the 7 spectral models and the two fitting methods. Coefficient of determination, slope and intercept of the linear regression are all listed, including 95th percentile confidence intervals. Overall, multi-peak models including 7-peak model demonstrate better correlation and agreement with MRS than single-peak model as reflected by the values of slope and intercept estimate. No significant difference (p=0.05) was observed for multi-peak models expect 7-peak model using both fitting methods. Further, mixed fitting demonstrates slightly stronger correlation and agreement than does magnitude fitting, although the differences are small.

3.6 Discussion

In this study we have analyzed the sensitivity of MRI-based CSE fat quantification to the choice of spectral model of fat, using both computer simulations and in vivo data acquired in patients. Spectral models of fat from previously published studies were used in this analysis and it was demonstrated that all multi-peak models showed greater accuracy for quantifying fat than the single-peak model. In addition, mixed fitting showed better agreement between the spectral models than magnitude fitting. Overall, these data demonstrate that multi-peak spectral modeling of fat is essential for accurate estimation of PDFF. However, no compelling evidence has been found to support any specific multi-peak spectral model of fat over the rest.

Among the discussed multi-peak spectral models of fat, the 7-peak model by Ren et al. was calibrated in subcutaneous fat while the others were all measured in liver. The results shown in this study indicate the 2 fat depots have similar fat spectral peaks. 3-peak (1.5T) and 7-peak (7T) models are also calibrated at different field strengths compared with other models (3T). The fact that these models are relatively interchangeable, suggests that MR spectroscopy is a reproducible tool for the measurement of fat spectrum in scanners at different field strength (1.5T - 7T).

In all signal estimation problems, bias will be introduced when there is discrepancy between the underlying physics (e.g. true spectral model) and the signal model used in the estimation of the parameters of interest. In the case of PDFF estimation, the resulting bias will depend on factors such as the true PDFF and the choice of echo times and fitting method (eg: magnitude vs mixed fitting).

The choice of echo times is an important component of CSE-MRI based fat quantification. It has been shown that the choice of echo times has a large impact on the noise performance of the technique[120,134]. Further, previous studies have shown that bias due to temperature-related effects (i.e.: model mismatch) is heavily influenced by the choice of echo times, and also the fitting method[135]. In this study, we have shown that bias created by discrepancies in the true spectral model and the estimator model will depend on the choice of echo times. Interestingly, the bias increased markedly with longer echo spacing. Bias can be limited by shortening initial echo time and echo time spacing. It was also important to note that mixed fitting was more robust to changes in echo time (ie: had less bias) than magnitude based fitting, which is consistent with the study by

Hernando et al[135]. This may explain the observation by Heba[136] that using a shorter echo train length may improve the accuracy of PDFF quantification using magnitude based fitting. A discrepancy between the underlying physics and the spectral model used in CSE-MRI may explain why using fewer echoes appears to lead to less bias, as shown in that study.

This study has several limitations. Small differences between a spectral model of fat used for PDFF estimation compared to actual spectra will reduce accuracy. However, we have demonstrated that the accuracy of PDFF quantification is relatively insensitive to different spectral models. Therefore, it is likely that errors introduced by small discrepancies in the spectral model relative to the true spectra are much smaller than the variability due to noise and other unrelated confounders. Large patient populations may be necessary to detect errors introduced by errors in the spectral model. Although, published data suggest relative uniformity in the triglyceride spectra across patients[66], variability in the spectra between patients could also introduce additional variability in the estimated PDFF. A second limitation is that all in vivo data and simulations were acquired at 1.5T. However, quantitative CSE-MRI is increasingly frequently performed on 3T scanners. The difference between these two platforms may result in different optimal echo times, which impacts the relative importance of the spectral models. In addition, this study did not consider the presence of liver iron overload. The high R_2* introduced by the presence of iron may affect the relative impact of different fat models. Furthermore, all in vivo data were acquired at the same echo time not allowing further in vivo validation of the echo time dependence of fat signal model related bias. Overall, however, we believe that the conclusions drawn by this study will, in all likelihood, extend to 3T and when R_2* is higher, although further work would be needed to confirm this speculation.

In conclusion, multi-peak spectral modeling of fat is essential for accurate estimation of tissue fat concentration, as measured by the proton density fat-fraction. Although spectral modeling is necessary, no specific choice of spectral model was shown to be superior, so long as one of the multi-peak models discussed in this work is used. Echo time combinations, such as shorter echo times, and the use of mixed fitting may be useful to minimize the impact of any model imperfections.

3.7 Acknowledgement

We acknowledge the use of the ISMRM Fat-Water Toolbox (http://ismrm.org/workshops/FatWater12/data.htm) for some of the reconstruction methods described in this article. We acknowledge the support of the NIH (R01 DK083380, R01 DK088925, K24 DK102595, and UL1TR00427). We also thank GE Healthcare for their support.

Chapter 4 : T_1-Corrected Quantitative Chemical Shift Encoded Magnetic Resonance Imaging

This work has been submitted to the *Magnetic Resonance in Medicine*. under the title “T_1-Corrected Quantitative Chemical Shift Encoded Magnetic Resonance Imaging”

4.1 Abstract

Purpose: To develop and validate a T_1-corrected chemical shift encoded MRI (CSE-MRI) method to improve noise performance and reduce bias for quantification of proton density fat-fraction (PDFF).

Methods: A variable flip angle (VFA)-CSE-MRI method using joint-fit reconstruction was developed and implemented. In computer simulation and phantom experiments, sources of PDFF bias measured with VFA-CSE-MRI were investigated. The effect of tissue T_1 on bias using low flip angle (LFA)-CSE-MRI was also evaluated. The noise performance of VFA-CSE-MRI was compared to LFA-CSE-MRI, for liver fat quantification. Finally, a prospective pilot study in patients undergoing gadoxetic acid-enhanced MRI of the liver to evaluate the ability of the proposed method to quantify liver PDFF before and after contrast.

Results: VFA-CSE-MRI was accurate and insensitive to transmit B_1 inhomogeneities in phantom experiments and computer simulations. With high flip angles, phase errors due to RF spoiling required modification of the signal model. For relaxation parameters commonly observed in liver, the joint-fit reconstruction improved the noise performance marginally, compared to LFA-CSE-MRI, but eliminated T_1-related bias. A total of 25 patients were successfully recruited and analyzed for the pilot study. Strong correlation and good agreement between PDFF measured with VFA-

CSE-MRI and LFA-CSE-MRI (pre-contrast) was observed before (R^2=0.97; slope=0.88, 0.81-0.94 95%CI; intercept=1.34, -0.77-1.92 95%CI) and after (R^2=0.93; slope=0.88, 0.78-0.98 95%CI; intercept=1.90, 1.01-2.79 95% CI) contrast.

Conclusion: Joint-fit VFA-CSE-MRI is feasible for T_1-corrected PDFF quantification in liver, is insensitive to B_1 inhomogeneities, and can eliminate T_1 bias, but with only marginal SNR advantage for T_1 values observed in the liver.

Keywords: Magnetic resonance imaging, chemical shift encoded imaging, proton density fat-fraction, fat quantification, hepatic steatosis, liver fat, T_1 correction, T_1 bias

4.2 Introduction

Since 1984, there have been tremendous advances in chemical-shift encoded magnetic resonance imaging (CSE-MRI) for robust separation of water and fat signals[137]. More recently, quantitative CSE-MRI methods for fat quantification have been developed through improved signal modeling that accurately reflects the underlying physics of proton signals from water and fat.

By accounting for confounding factors such as B_0 field inhomogeneity, R_2* signal decay[62,67,70] and multi-peak spectral modeling of fat[62,67], the proton density of individual chemical species can be estimated accurately. The effects of B_1 receive sensitivity are also eliminated through the use of the ratio of the fat signal to the total signal (water+fat) as the estimate of the local fat-fraction.

The T_1 of fat is typically shorter than that of water, leading to relative overestimation of fat-fraction, if the acquisition is T_1-weighted. The most common strategy to avoid T_1-related bias is to minimize T_1-weighting by reducing the flip angle[69].

When all confounding factors have been addressed, including T_1-related bias, the resulting fat-fraction estimate is equivalent to the proton density fat-fraction (PDFF). PDFF is the ratio of proton density of mobile fat protons to the total proton density of mobile water and mobile fat, and is a fundamental property of tissue that reflects tissue fat concentration[61].

T_1-insensitive low flip angle (LFA)-CSE-MRI methods have become widely accepted for liver fat quantification[138,139]. Estimation of PDFF in organs such as pancreas[140], muscle[141] adrenal glands[142] and even brown adipose tissue[143,144], have shown important research and clinical applications.

Unfortunately, the use of low flip angles is an inefficient use of longitudinal magnetization and limits the noise performance of CSE-MRI[145,146]. When the flip angle is sufficiently lower than the Ernst angle, the signal is approximately proportional to the flip angle, and any reduction in flip angle leads to a proportional reduction in signal amplitude. To address this limitation, Liu et al. first proposed the combined use of variable flip angle (VFA) methods with a three-point CSE-MRI method[69]. Other groups have also investigated related VFA strategies[147,148]. By acquiring two separate CSE-MRI acquisitions at different flip angles, T_1-corrected water and fat signals can be estimated.

In this work, we build on prior work by proposing to combine the VFA method with modern confounder-corrected CSE-MRI methods as an alternative to low flip angle CSE-MRI. Importantly, we note that a simple combination of the VFA approach with CSE-MRI leads to redundant estimation of R_2* and B_0 field inhomogeneity[69]. Both R_2* and B_0 inhomogeneity are independent of flip angle, and therefore joint estimation of R_2* and B_0 inhomogeneity along with T_1-corrected water and fat signal estimation should be feasible. By reducing the number of degrees of freedom in the signal model, the overall signal to noise ratio (SNR) performance of this estimation should also improve. Therefore, the overall purpose of this work is to develop and validate an SNR efficient T_1-corrected CSE-MRI method for accurate quantification of PDFF.

4.3 Theory

Low Flip Angle T_1-insensitive Quantitative CSE-MRI

Quantitative CSE-MRI to estimate PDFF is typically acquired using a multi-echo spoiled gradient-echo (SGRE) acquisition. Signal models typically ignore T_1-weighting, requiring the use of very low flip angles. In the following signal model, confounding factors including the spectral complexity of fat, B_0 inhomogeneity and R_2* decay, are accounted for:

$$S_{LFA}(TE_n;\ S_W, S_F, \Delta B_0, R_2{}^*, \phi_0\ ) =$$

$$e^{i(\gamma\cdot\Delta B0\cdot TE_n)}\cdot e^{-R_2{}^*\cdot TE_n}\cdot e^{i\phi_0}(\ S_W + S_F\cdot\textstyle\sum_{p=1}^{P} a_p e^{i2\pi\cdot f_p\cdot TE_n}) \qquad [4.1]$$

where $S_{LFA}(TE_n;S_W,S_F,\Delta B_0,R_2{}^*,\phi_0)$ is the signal at the nth echo time TE_n, ΔB_0 is the field inhomogeneity, and ϕ_0 is the common initial phase of water and fat. The signal consists of one water peak and P fat peaks. Both species are modeled to have the same R_2*, a valid assumption in the liver[65,149]. The relative amplitude and relative frequency shift of the pth fat peak are denoted as a_p, f_p, respectively, and are known a priori[66,67]. S_W, S_F, ϕ_0, ΔB_0, and R_2* are the unknown parameters to be estimated. PDFF is calculated as $S_F/(S_W+S_F)$. We note that Eq.4.1 can be rearranged to estimate PDFF directly[149].

The longitudinal magnetization at thermal equilibrium (M_W, M_F) is equivalent to the proton density of water and fat. However, S_W and S_F do not directly reflect the true proton densities. S_W and S_F are better modeled as M_W and M_F modulated by a T_1- weighting term:

$$S_W(TR, \alpha; T_{1W}) = M_W\,\frac{(1-e^{-TR/T_{1W}})\sin(\alpha)}{(1-e^{-TR/T_{1W}}\cos(\alpha))} \qquad [4.2a]$$

and

$$S_F(TR, \alpha; T_{1F}) = M_F \frac{(1-e^{-TR/T_{1F}})\sin(\alpha)}{(1-e^{-TR/T_{1F}}\cos(\alpha))} \quad [4.2b]$$

where α denotes the flip angle, and T_{1W} and T_{1F} are T_1 of water and fat, respectively. As α approaches 0, S_W and S_F approach $M_W \cdot \sin(\alpha)$ and $M_F \cdot \sin(\alpha)$ respectively and the T_1-weighting diminishes. Hence, with a low flip angle, estimates of PDFF, i.e.: $S_F/(S_W+S_F)$, approach T_1-independence[69].

The primary drawback of reducing the flip angle below the Ernst angle to minimize T_1-related bias, is the inefficient use of available longitudinal magnetization and reduced SNR performance.

2-Step Variable Flip Angle (VFA) T_1-corrected Quantitative CSE-MRI

The T_1-corrected VFA-CSE method proposed by Liu et al[69]. obtains two acquisitions at different flip angles, and avoids T_1-related bias by correcting for differences in T_1 between water and fat. This approach is an extension of VFA T_1 mapping techniques[112] (also known as DESPOT1) using SGRE images acquired at two or more flip angles. In Liu's approach, two sets of multi-echo SGRE data are acquired each with a different flip angle, yielding a set of T_1-weighted signals denoted $S_W(TR,\alpha_m;T_{1W})$ and $S_F(TR,\alpha_m;T_{1F})$. M_W and M_F are then estimated by applying DESPOT1 to $S_W(TR,\alpha_m;T_{1W})$ and $S_F(TR,\alpha_m;T_{1F})$ separately. Thus, estimates of PDFF are corrected for T_1-related bias. It has been shown that this approach can avoid T_1 bias while maintaining the noise performance of PDFF estimator[69]. This method will be referred to as the 2-step VFA-CSE-MRI.

Joint-fit VFA Reconstruction for T_1-corrected CSE-MRI

When using the 2-step VFA-CSE-MRI approach, S_W,S_F,ΔB_0,R_2^*, and ϕ_0 are all estimated separately for each flip angle. However, B_0 inhomogeneity and R_2^* are independent of flip angle, TR and T_1. Estimating these parameters separately for each flip angle introduces two unnecessary degrees of freedom into the signal model, which may degrade the noise performance.

If these degrees of freedom are removed, the noise performance of parameter estimation is expected to improve. In this work, we propose a joint-fit reconstruction combined with a VFA strategy using the single signal model shown below:

$$S_{VFA}(TE_n, \alpha_m, TR; M_W, M_F, \Delta B_0, R_2{}^*, \phi_0, T_{1W}, T_{1F}) = e^{-R_2{}^* \cdot TE_n} \cdot e^{i(\gamma \cdot \Delta B_0 \cdot TE_n)} \cdot$$

$$e^{i\phi_0}\left(M_W \frac{(1-e^{-TR/T_{1W}})\sin(\alpha_m)}{(1-e^{-TR/T_{1W}}\cos(\alpha_m))} + M_F \frac{(1-e^{-TR/T_{1F}})\sin(\alpha_m)}{(1-e^{-TR/T_{1F}}\cos(\alpha_m))} \sum_{p=1}^{P} a_p e^{i2\pi \cdot f_p \cdot TE_n} \right) \qquad [4.3]$$

where signals are acquired at echo times TE_n (n=1,…, N) with flip angles α_m (m=1,2). For each voxel, a total of 2N complex signals are fit using non-linear least squares fitting to estimate 7 parameters: M_W, M_F, ΔB_0, R_2*, ϕ_0, T_{1W} and T_{1F}. PDFF is then calculated using M_W and M_F estimates. Alternatively, we note that Eq.4.3 can be rearranged to estimate PDFF directly[149].

Assumptions about the Phase of Water and Fat with Radiofrequency (RF) Spoiling

It is often assumed that the SGRE signal is perfectly spoiled, i.e.: signal amplitude for each chemical species conforms to Eq.4.2 and signal phase is constant across chemical species and acquisition parameters. This is a valid assumption when RF spoiling is performed using a well-chosen phase increment[116] (e.g. 117°). The applied RF pulse in this simulation was a hard pulse (Dirac delta function) exciting all isochromats simultaneously and instantaneously, ignoring the effects of T_1 and T_2 relaxation during the RF pulse. The repetition time (TR) used in the simulation was 7.2ms. However, the effect of RF spoiling on SGRE signal phase, has not been thoroughly evaluated.

For this reason, a Bloch-equation computer simulation was performed to evaluate the phase of water and fat signals acquired using SGRE with RF spoiling. In a simulated voxel, 1000 isochromats periodically experienced a repeating sequence of an RF pulse, longitudinal and transverse relaxation, and 2π dephasing across the ensemble of isochromats at the end of each TR, to simulate an unbalanced frequency encoding gradient. The phases of the RF pulses and signal acquisition reference frame are determined by pseudo-random RF phase algorithm[116] using a phase increment of 117°. Relaxation properties chosen were those observed in liver at 1.5T[131,150]: T_{2W}=35ms,T_{2F}=62ms,T_{1W}=586ms, and T_{1F}=343ms.

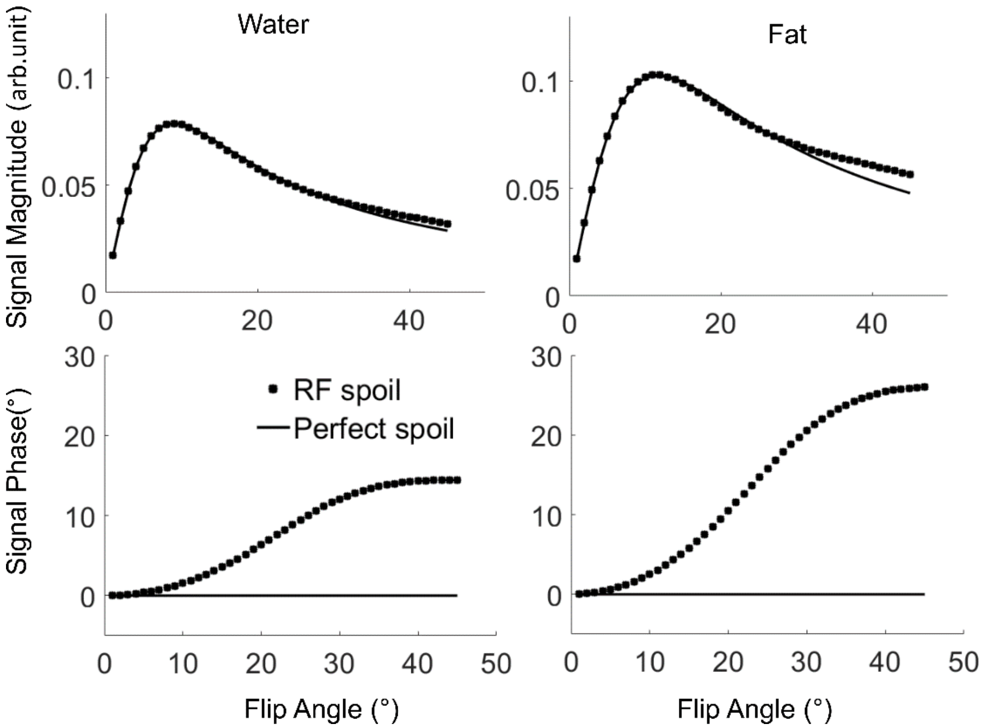

Figure 4.1 RF spoiling used with SGRE results in near perfect spoiling with of the signal magnitude, but leaves a strong flip angle dependent transverse signal phase. Steady state transverse signal amplitude and phase were calculated using Bloch-equation simulations.

As shown in Figure 4.1, the Bloch-equation simulation demonstrated a flip angle dependent phase difference between water and fat. For this reason, any previous VFA models that require the use of complex data, may be inaccurate due to the assumption of equal constant phase for all chemical species. Thus, Eq.4.3 must be modified to account for independent constant phase terms on the water and fat signals, i.e.:

$$\mathrm{S'}_{\mathrm{VFA}}(\mathrm{TE_n}, \alpha_\mathrm{m}, \mathrm{TR}; \phi_{W.m}, \phi_{F.m}, \mathrm{M_W}, \mathrm{M_F}, \Delta\mathrm{B_0}, \mathrm{R_2}^*, \mathrm{T_{1W}}, \mathrm{T_{1F}})$$

$$=$$

$$\mathrm{S}_{\mathrm{VFA}}(\mathrm{TE_n}, \alpha_\mathrm{m}, \mathrm{TR}; \phi_{W.m}\mathrm{M_W}, \phi_{F.m}\mathrm{M_F}, \Delta\mathrm{B_0}, \mathrm{R_2}^*, \phi_0 = 0, \mathrm{T_{1W}}, \mathrm{T_{1F}}) \quad [4.4]$$

which is a modified formulation in Eq.4.3 for the VFA-CSE-MRI signal, where the common phase term (ϕ_0) is replaced with independent phase terms for water and fat, with $\phi_{W,m}$ and $\phi_{F,m}$ (m=1,2). By modulating M_W and M_F with $e^{i\phi_{W,m}}$ and $e^{i\phi_{F,m}}$, the flip angle dependent phase shift resulting from RF spoiling is accounted for.

4.4 Methods

Overview

Computer simulations, phantom experiments and in vivo clinical experiments were performed. First, the Cramér-Rao lower bound (CRLB) was calculated to identify flip angle pairs that optimizes SNR performance of PDFF estimates using VFA-CSE-MRI. Next, computer simulation and phantom experiments were conducted to examine possible sources of PDFF bias with VFA-CSE-MRI. Potential sources include transmit B1 inhomogeneity, and differences in the constant phase of chemical species at different flip angles. The T_1-related bias of LFA-CSE-MRI was also simulated based on variation of T_{1W} due to biological variability or pathology, based on reports from the literature.

Further, the SNR performance of VFA-CSE-MRI and LFA-CSE-MRI were compared using CRLB prediction and Monte-Carlo simulations. The accuracy of VFA-CSE-MRI was then compared to LFA-CSE-MRI in phantoms with varying T_1 and PDFF. Finally, the in vivo accuracy of VFA-CSE-MRI was compared with LFA-CSE-MRI, in a prospective clinical study before and after administration of gadoxetic acid as contrast agent.

All computer simulations were conducted using Matlab (Mathworks Natick, MA). The non-linear least squares fitting used in parameter estimation in LFA-CSE-MRI was obtained from the ISMRM Fat-Water Toolbox[151] (http://ismrm.org/workshops/FatWater12/data.htm). For non-linear least squares fitting used with VFA-CSE-MRI, the levmar suite in Matlab was implemented (Foundation for Research and Technology-Hellas Heraklion, Crete, Greece). Constraints on the estimated T_1 ($0ms<T_{1w}<2000ms$, $40ms<T_{1F}<600ms$) were imposed to maintain robust performance when encountering PDFF values near 0% or 100%.

Tissue and Acquisition Parameters in Computer Simulation

For computer simulations performed in this work, typical T_1, T_2, and R_2* values of liver at 1.5T were used[65,66,131]: $R_2*=40s^{-1}$, $T_{2W}=35ms$, $T_{2F}=62ms$, $T_{1W}=586ms$, $T_{1F}=343ms$.

When synthesizing CSE-MRI signal in simulations described below, T_2 and T_1 were used in a Bloch equation simulation to calculate the initial phase of water and fat signal. These initial phases were filled into Eq.4 along with R_2*, T_{1W} and T_{1F} to synthesize the CSE-MRI signal.

Phantom Construction

A 7x4 grid of fat phantom vials was constructed with varying amounts of fat, and $CuSO_4$ to vary T_{1W}. Each vial was 98mm long, 28mm in diameter, and 40mL in nominal volume. Within each vial, a gel was constructed with agar (2%w/v), mixed with peanut oil and surfactant sodium dodecyl sulfate[152], with 7 volume fat-fractions varying between 0% and 60%. The agar gel was doped with four different concentrations of $CuSO_4$ (0.5mM, 1.0mM, 2.0mM, 4.0mM) to modify T_{1W} for each fat-fraction. The T_{1W} of the phantoms were measured using the VFA-CSE-MRI protocol described below for phantom acquisitions, and found to range from 863-986ms (0.5mM), 756-844ms (1mM), 399-445ms (2mM), and 249-283ms (4mM).

Flip Angle Optimization

The choice of flip angle pairs will impact the SNR performance of VFA methods[66]. To determine the optimal flip angle, the CRLB for estimation of PDFF from Eq.4.4 was formulated, as described by Scharf et al[153]. In this formulation, identical independently distributed Gaussian noise was assumed in real and imaginary channels with standard deviation of $(M_W+M_F)/400\times\sqrt{2}$.

The variance of PDFF estimated using VFA-CSE-MRI with joint estimation and 2-step reconstruction was calculated using liver tissue parameters at 1.5T (above). Other acquisition parameters are identical to those used in in vivo liver CSE-MRI and phantom experiments described below.

Phantom Data Acquisition

A multi-echo 3D SGRE pulse sequence was modified to acquire two SGRE signals with two different flip angles in a single sequential acquisition. Phantom experiments were conducted on a 1.5T clinical MRI system (Optima MR450w, GE Healthcare, Waukesha, WI).

For VFA-CSE-MRI, multi-echo, multi-flip angle SGRE data were acquired using the following acquisition parameters: TE_0=0.98ms,ΔTE=1.57ms,N=4 with unipolar flyback readout acquisition, TR=7.19ms, BW=±50kHz, slice=10mm, matrix=100x100, field of view (FOV)=$40\times34cm^2$, for true spatial resolution=$4\times4\times10mm^3$. Two flip angles (5°,20°) were acquired with four signal averages. This pair of flip angles optimizes SNR as predicted by the CRLB (below).

For LFA-CSE-MRI, SGRE data were acquired using the same sequence with a flip angle of 5°. Eight signal averages were obtained to match the VFA-CSE-MRI acquisition time. We note that a flip angle of 3-5° is commonly used for liver fat quantification with CSE-MRI[31,33,139].

One additional LFA-CSE-MRI SGRE dataset was acquired with flip angle=1° and same acquisition parameters described above, to provide reference PDFF measurements with minimal T_1-related bias.

Sensitivity of VFA-CSE-MRI to Inaccurate Transmit B1

For VFA-CSE-MRI, flip angles are treated as known parameters. In reality, due to imperfect calibration and inhomogeneities in the transmit B_1 amplitude, actual flip angles may deviate from the nominal values, and VFA T_1 estimation is known to be sensitive to B_1 errors[112]. However, for our application, we are interested primarily in estimation of PDFF, and it is unknown how B_1 transmit errors will impact PDFF estimates using VFA-CSE-MRI. As both T_{1W} and T_{1F} are affected by the same flip angle error, it was hypothesized that the ratio of fat and water signals may compensate for proportional errors in the flip angles[69].

Using acquisition and tissue parameters listed above for the phantom experiment, a computer simulation was performed to assess bias due to transmit B_1 errors. A true PDFF of 20% were assumed. Noise free simulated signals were generated using the VFA signal model (Eq.4.4). PDFF was estimated using the same signal model, but with (5°,20°) scaled by factors of 0.7 through 1.3 to simulate transmit B_1 errors of -30% to 30%.

Further, in a phantom experiment, VFA-CSE-MRI PDFF maps were reconstructed using Eq.4.4, with flip angles purposely scaled by factors of 0.7 to 1.3 to create effective transmit B_1 errors. LFA-CSE-MRI PDFF maps were also reconstructed from 1° SGRE (with 8 averages) data using the signal model in Eq.4.1, to provide reference PDFF values.

Reconstructed PDFF maps from the phantom were analyzed using circular regions of interest (ROIs) with an area of approximately 2cm^2 placed in the center slice of the 3D volume in each phantom vial. ROIs were co-registered between VFA- and LFA-CSE-MRI PDFF maps.

Bias in LFA-CSE-MRI Resulting from T_{1W} Variation

The use of low flip angles is known to reduce, but not entirely eliminate bias in PDFF estimates. If the T_{1W} and T_{1F} are known, it is also possible to perform a simple T_1-correction based on Eq.4.2a, Eq.4.2b using T_{1W} and T_{1F} values found in literature[31,130]. However, it is well known that inter-subject variation of T_{1W} exists in the liver[154] and pathology such as iron-overload and fibrosis are well known to alter T_{1W}[155,156]. T_{1W} values from 380ms to 800ms have been reported[155,156]. Further, the dramatic changes in T_{1W} after the administration of contrast will also impact PDFF estimates by LFA strategies[157–159].

To examine the residual bias in LFA-CSE-MRI over a wide range of T_1 values, a computer simulation was performed. Noiseless SGRE signals were generated using Eq.4.4 with T_{1W} =380, 586, 680 and 830ms to predict the effects of T_{1W} variation on PDFF estimation with LFA-CSE-MRI, using LFA acquisition parameters experiment described below for the in vivo liver study. Flip angles of 1° ,2° ,3° ,4° , and 5° were used in the simulation. Bias with and without simple T_1-correction was calculated for PDFF generated using the LFA signal model (Eq.4.1). Simple T1-correction assumed T_{1W}=586ms and T_{1F}=343ms. True PDFF was assumed to be 30% for this simulation.

Noise Performance of VFA-CSE-MRI and LFA-CSE-MRI

CRLB analysis and Monte-Carlo computer simulations were performed to compare the noise performance between three methods: 1) T_1-corrected VFA-CSE-MRI using the proposed joint-fit reconstruction, 2) T_1-corrected VFA-CSE-MRI using 2-step reconstruction, and 3) T_1-insensitive LFA-CSE-MRI (flip angle=2°,3°). The Monte-Carlo simulations were conducted to confirm the CRLB analysis. Noise was assumed to be identical independently Gaussian distributed with standard deviation of $(M_W+M_F)/400$ in real and imaginary components of the signals. The standard deviation was multiplied by $\sqrt{2}$ for T_1-corrected VFA-CSE-MRI to normalize SNR for acquisition time. Acquisition parameters are the same as the ensuing in vivo liver experiments, and liver relaxation parameters were those at 1.5T (above).

Assumed Constant Phase for VFA-CSE-MRI Signal Model

To evaluate assumptions regarding the constant phase of water and fat signals in Eq.4.3 and Eq.4.4, computer simulations and phantom experiments were conducted.

Bloch-equation simulations were performed, as described above with liver tissue parameters at 1.5T and phantom experiment acquisition parameters. Generated signals were fit to Eq.4.3 and Eq.4.4. Bias in PDFF estimates produced with the two models were compared.

For the phantom experiment, acquired VFA-CSE-MRI data were reconstructed with the signal models in Eq.4.3 and Eq.4.4, separately. LFA-CSE-MRI (flip angle=1°) data provided a low T_1-bias reference.

Phantom Validation of Accuracy of VFA-CSE-MRI

To validate the accuracy of T_1-corrected VFA-CSE-MRI in phantoms, PDFF values calculated using VFA-CSE-MRI (flip angle=5°,20°), LFA-CSE-MRI (flip angle=5°) were compared to PDFF measured using LFA-CSE-MRI (flip angle=1°) as the reference. The PDFF values for each method were obtained from co-registered circular ROIs ($2cm^2$) on center-slice PDFF maps.

In addition, PDFF values containing T_1-bias resulting from the high flip angle (20°) portion of the VFA acquisition were calculated and plotted in the same figure. These values were denoted as high flip angle (HFA).

In Vivo Validation of Joint-fit VFA-CSE-MRI to Quantify Hepatic PDFF

A prospective pilot study was performed in patients undergoing gadoxetic acid-enhanced abdominal MRI or MR cholangiopancreatography (MRCP), for a variety of routine clinical indications. Add-on LFA- and VFA-CSE-MRI acquisitions were performed before and approximately 20 minutes after the administration of 0.05mmol/kg of gadoxetic acid (standard clinical dose at our institution) to examine the effects of major changes in T_1 on the accuracy of fat quantification with LFA- and VFA-CSE-MRI. All in vivo imaging was performed after obtaining IRB approval and informed written consent.

All in vivo imaging was performed on 1.5T clinical MRI systems (Optima MR450w/Signa Artist, GE Healthcare, Waukesha, WI) using 32 elements of 48-channel phased-array torso coil. The same 3D multi-echo SGRE pulse sequence used for phantoms was used to acquire SGRE images at two different flip angles over the entire liver, within a single 20 second breath-hold. Other acquisition parameters included TE_0=0.98ms, ΔTE=1.57ms, N=4 with unipolar flyback acquisition, TR=7.19ms, BW=±50kHz, flip angles=(5°,20°), FOV=40×34cm^2, matrix=100×100, slice=10mm, and 24 slices, for true spatial resolution of 4x4x10mm^3. These parameters with the exception of the number of signal averages are the same as those used in the phantom experiment. k-space corner cutting was performed to shorten breath-hold time[160].

For LFA-CSE-MRI, the identical acquisition was performed but with two signal averages and flip angle set to 3°. A 3° angle was chosen rather than the typical 5°, because of the short TR used for this acquisition[31,33].

PDFF maps (pre- and post-contrast) were estimated using the joint-fit VFA-CSE-MRI method using the signal model with independent phase (Eq.4.4). Similarly, PDFF maps (pre- and post-contrast) were estimated using the LFA-CSE-MRI method by fitting source images to Eq.4.1 with non-linear least squares fitting. For pre-contrast LFA-CSE-MRI, simple T_1 correction was performed as described above assuming known values for the T_1 of water and fat[31,130] in the liver at 1.5T[131] (T_{1W}=586ms,T_{1F} =343ms). To demonstrate T_1-related bias that arises from a large flip angle, PDFF maps were reconstructed from the 20° component of the VFA-CSE-MRI data using the T_1-uncorrected signal model (Eq.4.1). These maps are denoted as HFA.

To analyze all resulting PDFF maps, one ROI was placed in each of the 9 Couinaud segments of the liver, using a standard paradigm described by Campo et al[161]. For each acquisition, the 9 PDFF values were averaged, resulting in 6 PDFF estimates per patient (LFA pre- and post-contrast, VFA pre- and post-contrast, HFA pre- and post-contrast). In addition, R2* and T_{1W}, as byproducts of LFA-CSE-MRI (R_2*) and VFA-CSE-MRI (R_2* and T_{1W}) were measured from the same ROIs.

Comparisons of the PDFF values were made using linear regression, to calculate the slope, intercept, and Pearson correlation coefficient, all with 95% confidence intervals. LFA-CSE-MRI pre-contrast PDFF measurements were used as the reference standard.

4.5 Results

Flip Angle Optimization

Based on the CRLB analysis, the flip angle pair that maximizes PDFF estimator SNR for joint-fit VFA-CSE-MRI is 6° and 31-33°, for liver imaging at 1.5T (Figure 4.2A). High flip angles, such as 33° may be limited by specific absorption rate (SAR) heating limitations and can amplify flow and motion artifacts. Fortunately, a broad maximum in the optimization demonstrates that a wide range of optimal of flip angles can be used. As shown in Figure 4.2B there is marginal difference between the optimum SNR for upper flip angle limit of 33° (SNR = 5.6) and 20° (SNR = 5.4). For this reason, a flip angle pair of 5° and 20° was chosen for both phantom and in vivo VFA-CSE-MRI.

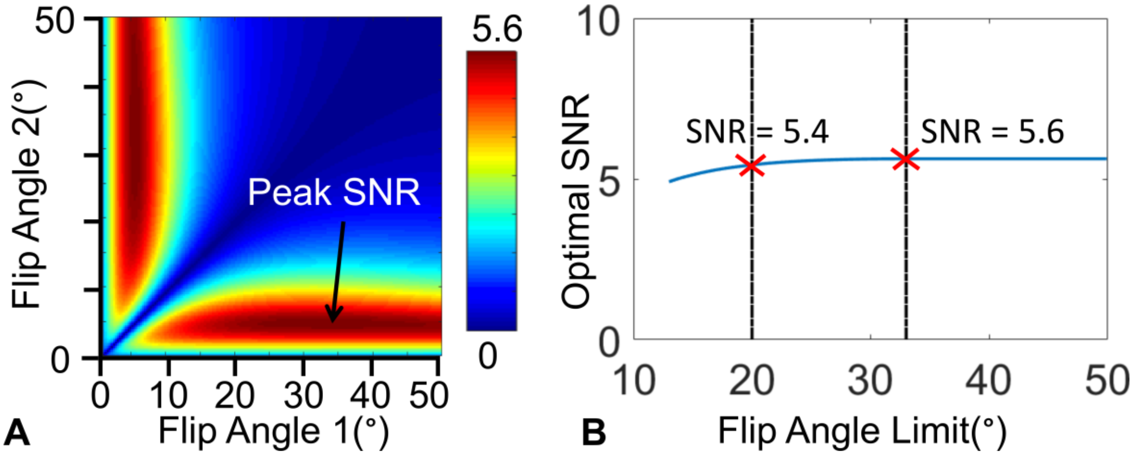

Figure 4.2 CRLB analysis can be used to identify optimal flip angle pairs that optimize the SNR performance of the proposed VFA-CSE-MRI method. In these plots SNR is defined as 20/(standard deviation of PDFF estimator). A) Predicted SNR with respect to all flip angle pairs. B) Optimal SNR with flip angle pairs under the constraint of an upper limit. The broad maximum, allows flip angle #1 to be reduced from 33° to 20°with marginal SNR penalty.

Sensitivity of VFA-CSE-MRI to Inaccurate Transmit B_1

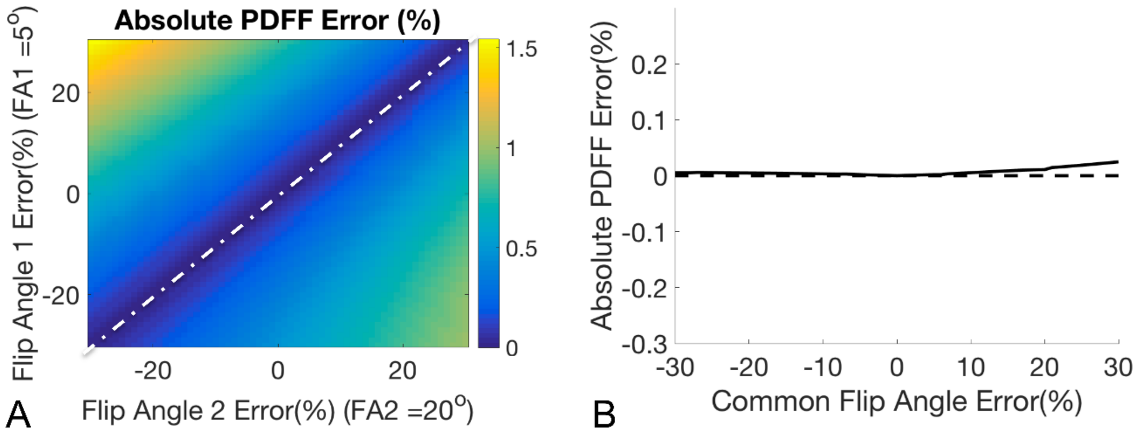

Figure 4.3 PDFF estimation using VFA-CSE-MRI is insensitive to transmit B_1 inhomogeneities in simulations. In this simulation negligible error in the estimated PDFF was observed. Absolute PDFF error as predicted by simulation in liver fat quantification at 1.5T (A, B) is shown. Note that these simulations assume that the percent error in transmitted B_1 is the same for both flip angles.

Figure 4.3 plots the error in PDFF estimation using VFA-CSE-MRI resulting from inaccurate transmit B_1. As shown in Figure 4.3B, errors in PDFF estimation are essentially zero, over a wide range of B_1 errors.

Similar results were observed in the phantom experiment, despite a wide range of T_{1W} values, and a wide range of B_1 transmit errors (Figure 4.4). The PDFF estimates using different nominal flip angles were all within 1.4% absolute PDFF values.

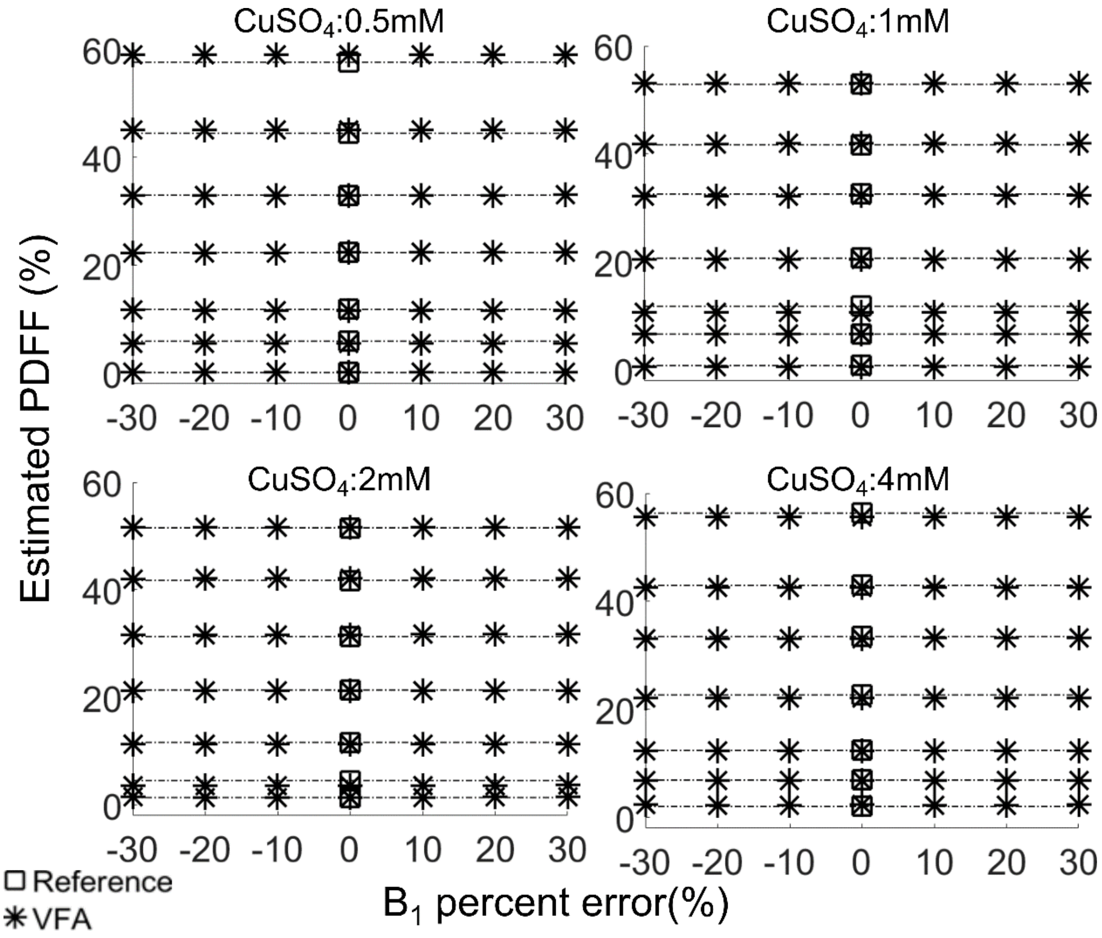

Figure 4.4 PDFF estimation using VFA-CSE-MRI is insensitive to transmit B_1 inhomogeneities in phantom experiments. Plots show PDFF measured using joint-fit VFA-CSE-MRI in phantoms in the presence of B_1 error. Phantoms were constructed in groups with varying PDFF and T_{1W} values controlled by doping agent $CuSO_4$. PDFF measurement with LFA-CSE-MRI (flip angle=1°) was used as the reference.

Bias in LFA-CSE-MRI from T_{1W} Variation

As demonstrated in Figure 4.5, bias in PDFF exceeding 1% (absolute) can occur when T_1-correction is not used, with T_{1W} above 680ms, flip angle of 3° and true PDFF of 30%. By applying a simple T_1-correction assuming T_{1W}=586ms and T_{1F}=343ms, bias in PDFF estimate can be limited to less than 1% for all T_{1W} values between 380ms and 830ms. However, if a bias less than 0.5% (absolute) is needed, a flip angle less than 2° would be necessary, negatively impacting SNR performance.

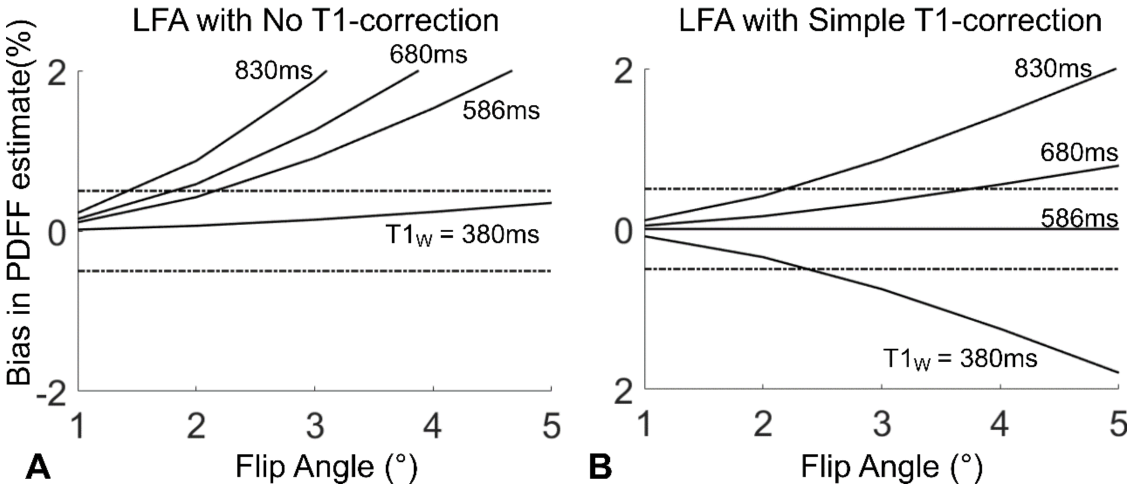

Figure 4.5 Any degree of T_1-weighting leads to bias in PDFF estimation if the T_1 of water and fat are different (A). Simple correction (eg. assuming T_{1W} = 586ms and T_{1F} = 343ms), also leaves considerable bias if the true T_1 values are different than assumed values (B). These simulations demonstrate the utility of T_1-corrected methods such as the proposed VFA-CSE-MRI method.

Noise Performance of VFA-CSE-MRI and LFA-CSE-MRI

As shown in Figure 4.6, joint-fit VFA-CSE-MRI produced PDFF estimates with slightly higher SNR compared with the 2-step method. Notably, both VFA-CSE-MRI methods have lower SNR than the 3° flip angle LFA-CSE-MRI method. We also note that the SNR using LFA method is heavily influenced by flip angle. When a flip angle of 2° is used (e.g. to further reduce T_1-related bias), the noise performance of the LFA method drops below that of VFA-CSE-MRI.

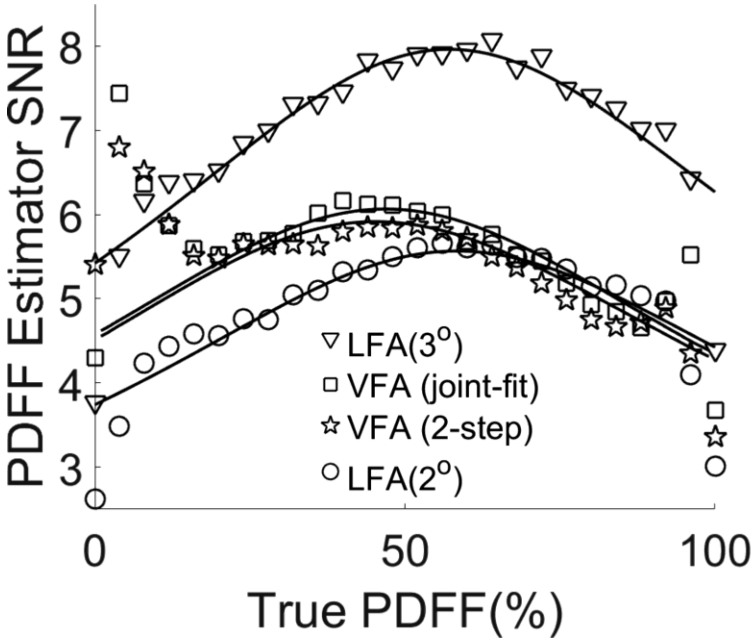

Figure 4.6 Noise performance of PDFF estimation using CRLB analysis (solid line) and Monte Carlo simulations (data points), demonstrate that for parameters commonly encountered in the liver that LFA-CSE-MRI methods have the highest SNR performance, although this performance is highly dependent on the flip angle. At very low flip angles (eg. 2°), conventional LFA-CSE-MRI has lower SNR performance. Interestingly, the proposed joint-fit VFA-CSE-MRI shows only slightly improved performance compared to the 2-step VFA method. This is likely due to the need for estimating independent constant phase on the water and fat signals, for the joint-fitting, due to the residual species dependent phase from RF spoiling. Note that SNR is defined as 20/(estimator standard deviation) for each method. The input SNR in these analyses was normalized for acquisition time.

Assumption Regarding Phase in VFA-CSE-MRI Signal Model

When a common phase was assumed in signal model (Eq.4.3) for both computer simulations and phantom experiments, bias was observed in PDFF estimates made using VFA-CSE-MRI. As shown in Figure 4.7, PDFF estimates made using the modified signal model (Eq.4.4) eliminated all bias in simulations and reduced bias in phantom experiments substantially.

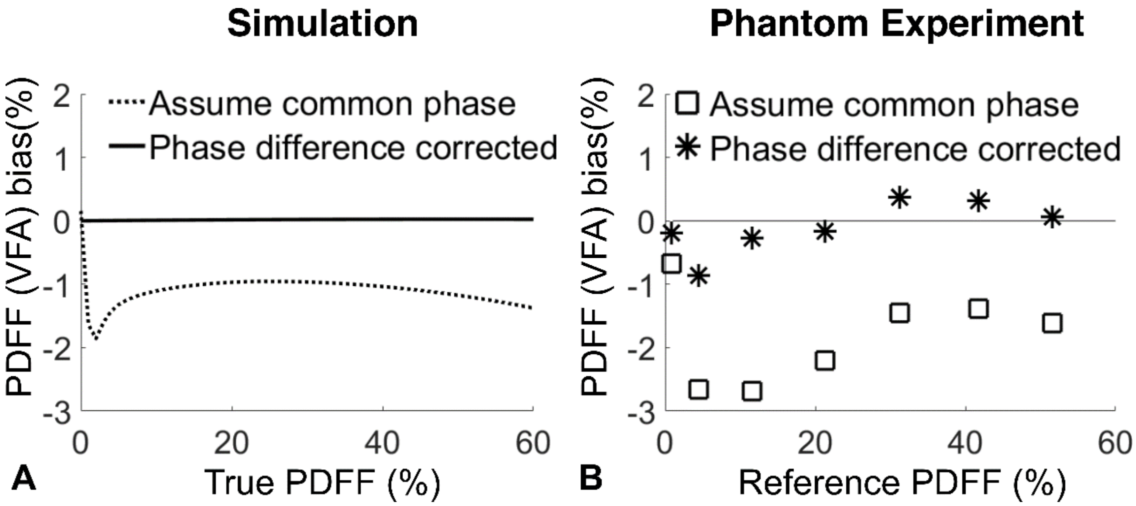

Figure 4.7 Modeling for different constant phase values between water and fat resulting from RF spoiling is needed to address the resulting bias in PDFF if this confounder is not considered. This bias can be eliminated in simulations (A) and greatly reduced in phantoms (B). The phantom used for these measurements was that doped with 1mM $CuSO_4$.

Phantom Validation of Accuracy of VFA-CSE-MRI

As shown in Figure 4.8, PDFF estimated using the VFA-CSE-MRI method agreed very closely with the reference PDFF measurements, for all $CuSO_4$ concentrations. When a 5° or 20° flip angle was used, PDFF was overestimated. As expected, this bias was highest at lower concentrations of $CuSO_4$, when the differences in T_1 between water and fat are the greatest.

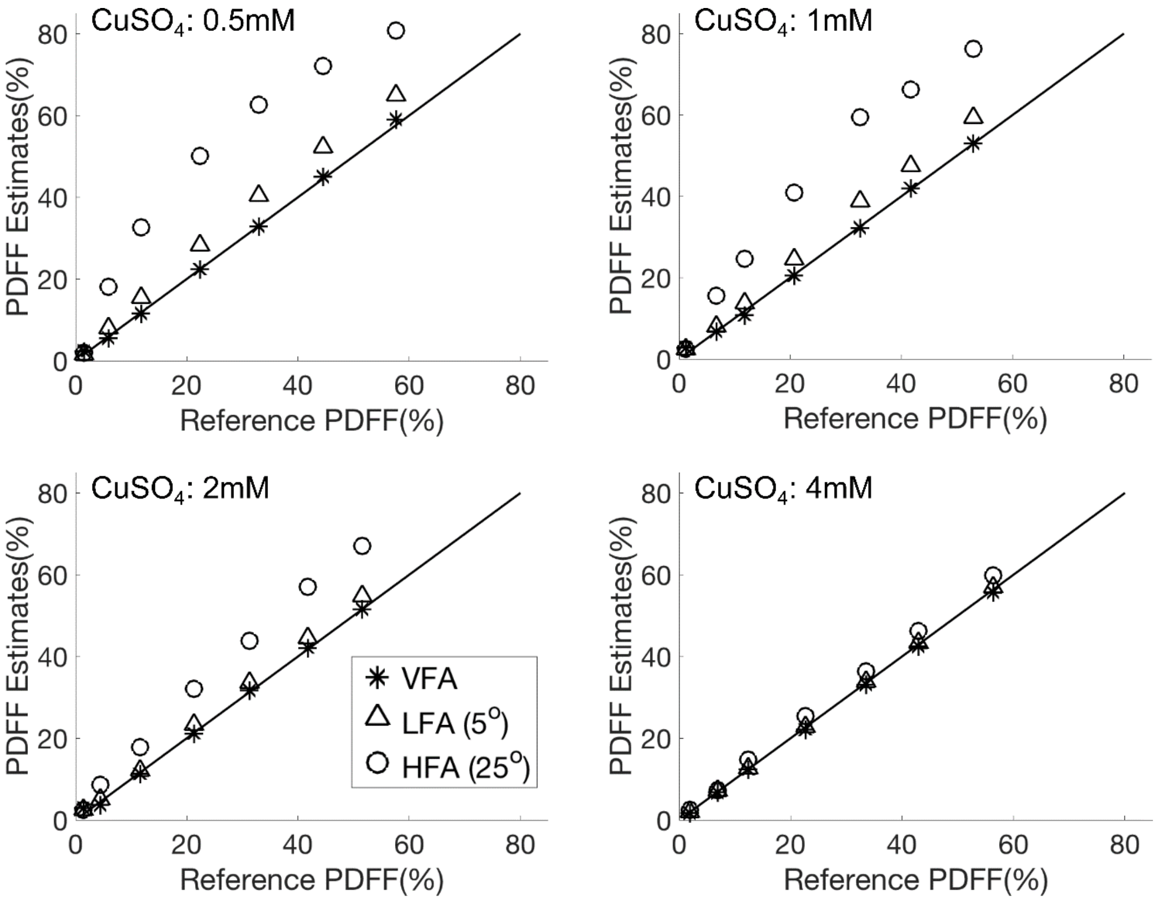

Figure 4.8 The proposed VFA-CSE-MRI method eliminates T_1-related bias, as shown in phantom experiments. The degree of bias is highly dependent on the difference in T_1 between water and fat. High flip angle CSE-MRI acquisitions demonstrate large bias, while even low flip angle acquisitions demonstrate measurable bias.

Liver in Vivo Validation of VFA-PDFF Accuracy

27 patients were recruited for this pilot study. Data from two patients were rejected due to excessive motion artifact from poor breath-holding. Of the remaining twenty-five data sets there were a total of 9:16 men:women with an average age of 48.5 years (range=21-75 years) referred for a wide variety of indications for gadoxetic acid-enhanced MRI or MRCP. Clinical indications included: indeterminate liver lesions seen on other imaging modalities (8), primary sclerosing

cholangitis (4), hepatic adenomatosis (4), focal nodular hyperplasia (2), suspected metastatic disease with known malignancy (3), follow-up of known hepatic metastatic disease (1), known cholangiocarcinoma (1), hepatocellular carcinoma surveillance (1), and abdominal pain not otherwise specified (1). Example PDFF, R_2* and T_{1W} maps from one patient with elevated liver fat before and after contrast are shown in Figure 4.9.

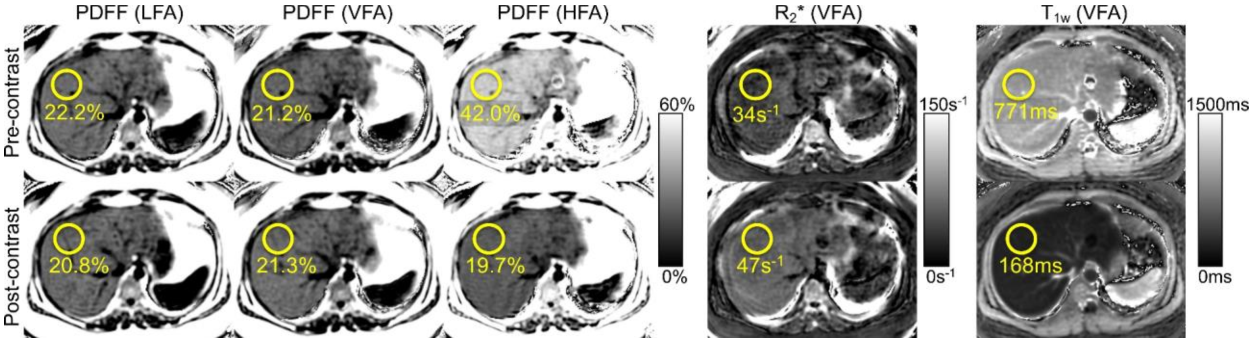

Figure 4.9 Example PDFF, R_2* and T_{1W} maps from a subject with elevated liver PDFF, acquired before and after the administration of gadoxetic acid, visually demonstrating the effects of contrast on estimated PDFF, R_2* and T_{1W} values. In this figure, the PDFF map and ROI value shown for LFA-CSE-MRI pre-contrast was not corrected with any T_1 assumption.

Comparisons of PDFF estimates between LFA-, HFA- and VFA-CSE-MRI, before and after contrast are shown in Figure 4.10. When comparing PDFF measured using VFA-CSE-MRI with PDFF measured with LFA-CSE-MRI (pre-contrast), VFA method showed strong correlation and near agreement with LFA-CSE-MRI (pre-contrast) both before (R^2=0.97, m=0.88[0.81 0.94], b=1.34%[0.77 1.92]) and after (R^2=0.93, m=0.88[0.78 0.98], b=1.90%[1.01 2.79]) contrast administration. An apparent slope less than one and intercept greater than zero was noted, due to a small disagreement between LFA- and VFA-CSE-MRI PDFF results at low PDFF values. When the regression was repeated excluding PDFF<5%, the result improved before (R^2=0.98, m=0.95[0.87 1.03], b=0.35%[-0.55 1.24]), and after (R^2=0.94, m=0.95[0.82 1.09], b=0.87%[-0.65 2.39]) contrast, respectively.

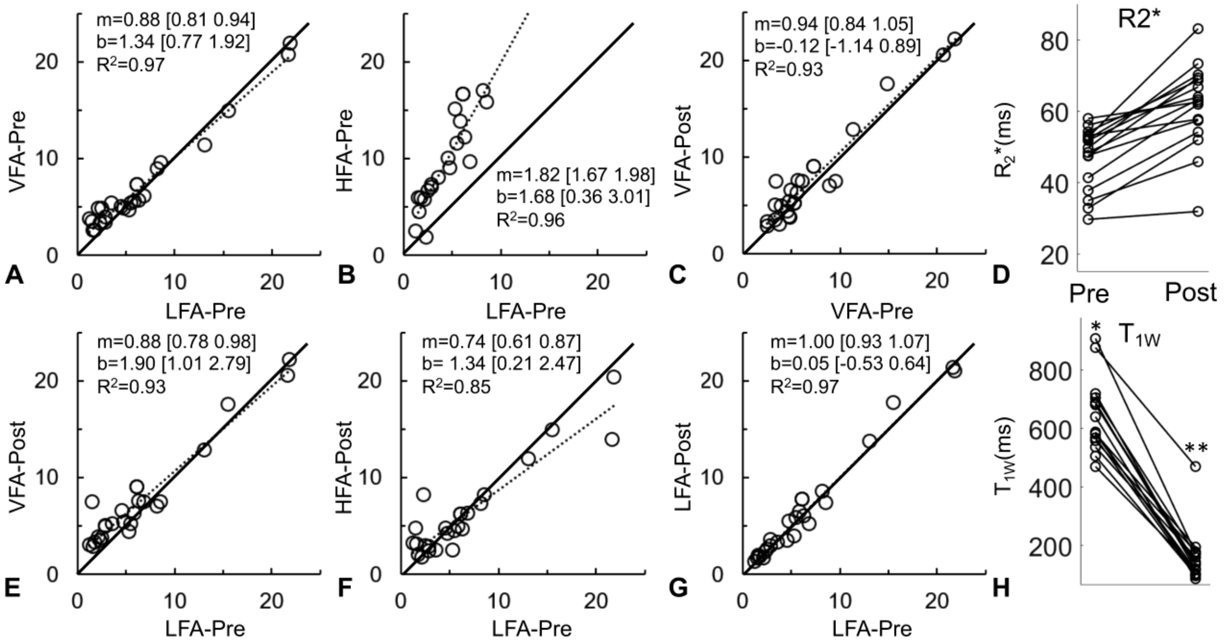

Figure 4.10 Summary results from the pilot clinical study demonstrate strong correlation good agreement between VFA-PDFF and LFA-PDFF before and after contrast, whereas the high flip angle acquisition leads to strong positive T_1-related bias before contrast and strong negative T_1-related bias after contrast. Also shown are R_2* and T_{1W} before and after gadoxetic acid. A small increase in R_2* is noted and also a strong decrease in T_{1W} observed, due to the presence of gadolinium. Note one outlier with high T_{1W} (pre,*) is in a patient with biopsy proven NASH, and a second outlier (post,**) was from a patient with known cholangiocarcinoma and liver failure related to biliary obstruction.

The correlation and agreement between VFA-CSE-MRI before and after contrast was very strong (R^2=0.93, m=0.94 [0.84 1.05], b=-0.12% [-1.14 0.89]) indicating that the VFA-CSE-MRI approach corrected PDFF over a very wide variation of T_{1W}. Similarly, the LFA-CSE-MRI produced accurate PDFF estimates even after contrast administration (R^2=0.97, m =1.00 [0.93 1.07], b=0.05% [-0.53 0.64]).

However, if a high flip angle is used without T_1-correction, the PDFF measurement demonstrates considerable bias both before (R^2=0.96, m=1.82 [1.67 1.98], b=1.68% [0.36 3.01]) and after (R^2=0.85, m=0.74 [0.61 0.87], b=1.34% [0.21 2.47]) contrast. Interestingly, the bias with HFA-CSE-MRI acquisition reverses to a negative bias after the administration of contrast, because the T_{1W} is less than T_{1F}, in the presence of gadolinium.

Example R_2* and T_{1W} images are also shown in Figure 4.9. The effect of contrast on R_2* and T_{1W} is clearly evident. Further, the measured values of T_{1W} and R_2* are shown in Figure 4.10. An outlying pre-contrast T_{1W} measurement (945ms,*) is noted. The elevated $T1_W$ value is consistent with biopsy proven non-alcoholic steatohepatitis (NASH) in this patient. Further, an outlying post-contrast (450ms,**) was observed in a patient with known cholangiocarcinoma and liver failure related to biliary obstruction, leading to reduced hepatic uptake of gadoxetic acid.

4.6 Discussion

In this study, a T_1-corrected fat quantification technique was developed and rigorously evaluated. In the presence of differences between T_{1W} and T_{1F}, T_1-corrected VFA-CSE-MRI with optimized flip angle pairs and joint-fit reconstruction proved to be unaffected by large T_{1W} variations. Importantly, this strategy was shown to be robust to large transmit B_1 inhomogeneities, and also over a wide range of T_1 differences between water and fat.

This work demonstrates that the proposed VFA method with joint-fit reconstruction is feasible for T_1-corrected PDFF quantification. The accuracy of the proposed method was validated through simulations and phantom experiments, and evaluated in an in vivo clinical study at 1.5T. Further, the SNR performance of this approach is most advantageous when there are large differences between the T_{1W} and T_{1F}. Importantly, we found that the VFA approach for typical liver tissue relaxation parameters did not confer a large SNR benefit compared with LFA-CSE-MRI, although provided T_1-corrected estimates of PDFF, even with widely varying differences between T_{1W} and T_{1F}. Further, in applications where large T_{1w} variation exist and very low flip angle acquisitions (e.g. 2°) were required in LFA-CSE-MRI, the VFA-CSE-MRI had superior noise performance over LFA-CSE-MRI with very low flip angle acquisitions that can be used to minimize T_1-related bias. A small relative bias between LFA- and VFA-CSE-MRI methods was observed at low PDFF values in vivo. While the source of this bias is uncertain, we speculate it may be a result of unstable T_{1F} estimates when the fat signal was low. Further investigation will be required into this observation.

Importantly, this work also identified an important new source of bias for complex-based CSE-MRI methods that utilize the acquired signal at high flip angles, like the method proposed in this work. Specifically, unanticipated relative phase shifts between water and fat signals and at different flip angles related to RF spoiling were identified. Such phase shifts have not been previously described in this context. With joint-fitting of complex VFA signals, however, introduction of new degrees of freedom in the signal model (independent phase shift for each chemical species at each flip angle) was necessary.

In contrast to widely used LFA-CSE-MRI, the proposed VFA method extends the possible choices of flip angles by including T_1-weighting in the signal model, enabling the acquisition of high SNR source images. However, the need for independent estimation of T_{1W} and T_{1F} introduces additional degrees of freedom. These additional parameters, in addition to a phase shift related to RF spoiling that has been newly identified in this manuscript, offset the advantages of the high SNR source images. Compared with the 2-step VFA method developed by Liu et al[69]. and Tamada et al[148]., the use of joint-fitting slightly improved the SNR by eliminating the redundant estimation of field inhomogeneity and R_2^*. Karampinos et al[147] also investigated the joint estimation of R_2* and B_0 field inhomogeneity in VFA-CSE-MRI based on IDEAL reconstruction. In comparison, this work applied joint estimation and VFA T_1-correction to modern confounder-corrected CSE-MRI using non-linear least squares reconstruction. Further, the phase difference in spoiled gradient echo signal at different flip angles, which was unaccounted for by Karampinos et al, was corrected in this work.

It is well established that LFA-CSE-MRI fat quantification is highly accurate in the liver[31,33,139]. As also shown in this work a LFA-CSE-MRI with a 3° flip angle has similar SNR to VFA-CSE-MRI in the liver at 1.5T. However, due to variation in T_{1W} caused by biological variability, pathology or the presence of contrast agents, the bias in PDFF using LFA-CSE-MRI may be high for some applications. By comparison, PDFF estimated using VFA-CSE-MRI is unaffected over a wide range of T_{1W} values.

The main advantages of LFA-CSE-MRI are its simplicity and low T_1-related bias, particularly at low PDFF values. At the same time, LFA-CSE-MRI can be performed with a shorter minimum acquisition time. Further, VFA-CSE-MRI requires the use of a more complex reconstruction algorithm, although such algorithms are fully automated and inapparent to the user. A major advantage of VFA-CSE-MRI is removal of T_1-related bias, over a wide range of T_1 values, particularly at higher fat-fraction values.

One limitation of this study is that the proposed joint-fit VFA-CSE-MRI was only evaluated at 1.5T, whereas CSE-MRI is routinely performed at both 1.5T and 3.0T[32,34,139,162,163]. Further evaluation at 3.0T will be needed for comprehensive evaluation of this strategy. We speculate that the wider separation between T_{1W} and T_{1F} at 3.0T field strength may improve the SNR performance of VFA-CSE-MRI relative to LFA-CSE-MRI. With increasing differences between T_{1W} and T_{1F} at 3T, the LFA-CSE-MRI approach must use smaller flip angles to avoid T1-related bias, degrading its SNR performance. Further studies will be needed to evaluate VFA-CSE-MRI at 3.0T.

Another limitation of the VFA strategy is that it doubles acquisition time. In this study, breath-hold acquisitions over the entire liver were feasible, although with reduced spatial resolution. The use of 2D parallel imaging may be a useful way to alleviate acquisition time limitations.

We also note that the in vivo accuracy of VFA-CSE-MRI at low fat-fractions demonstrated some bias, unlike in phantoms where VFA-CSE-MRI was accurate across all PDFF values. This bias may be related to lower SNR in vivo, leading to instability and bias from T_{1F}-corrected estimates of the fat signal at low fat concentrations. This is a recognized limitation of VFA-CSE-MRI strategies[69], and can be mitigated in part through the use of physically plausible lower and upper bound constraints on the estimated T_{1F}. Although we employed the use of such constraints in our estimation strategy, further optimization and the use of more advanced approaches, such as PDFF-dependent constraints may address this bias, and should be considered in future work.

Further, we note that the VFA-CSE-MRI approach, like conventional LFA-CSE-MRI also provided estimates of R_2*. As this patient population did not include any patients with iron overload, rigorous evaluation of the performance of VFA-CSE-MRI to quantify R_2* was not performed, and this was also beyond the scope and purpose of this work.

Finally, the VFA-CSE-MRI method also provided estimates of the T_1 of water and fat. The T_{1F} was not analyzed, as these values are noisy when fat is present in low concentration, such as that observed in the liver. T_{1W} was measured before and after the administration of gadoxetic acid, and found to be very similar to values reported in the liver both before[131] and after contrast[158]. Rigorous evaluation of T_{1W} estimation in phantoms and in vivo using a reference standard was not performed, as this was also beyond the scope and purpose of this work. We also note that like conventional DESPOT1, T_1 estimates made using the proposed VFA-CSE-MRI may be confounded by transmit B_1 inhomogeneities. However, no obvious spatial variation resulting from B_1 inhomogeneities was observed, likely due to the use of 1.5T where B_1 inhomogeneities tend to be small.

In conclusion, joint-fit VFA-CSE-MRI is a feasible technique for T_1-corrected fat quantification particularly for applications where there are large differences between T_{1W} and T_{1F}. For measurement of PDFF, this approach is independent of B_1 transmit inhomogeneities and provides fully T_1-corrected estimates of PDFF. Further evaluation of this strategy in clinical studies, including at 3.0T, may be warranted to determine its clinical utility and performance as an accurate and precise biomarker of liver fat quantification.

4.7 Acknowledgement

We acknowledge the use of the ISMRM Fat-Water Toolbox (http://ismrm.org/workshops/FatWater12/data.htm) for some of the reconstruction methods described in this article. We also acknowledge the assistance of Mr. Takanori Ii with data analysis and Dr. David Harris with manuscript preparation. We also thank Ms. Ann Shimakawa and Dr. Bruce Collick for their advice. We also acknowledge the support of the NIH (R01 DK083380, R01 DK100651, K24 DK102595, R01 DK117354 and R01 DK088925) including the UW ICTR grant UL1TR000427 from NIH/NCATS. We also wish to thank the NIH (UL1TR00427) as part of a pilot funding grant through the University of Wisconsin Institute for Clinical and Translational Research (ICTR).

Chapter 5 : An Acetone Based Phantom for Quantitative Diffusion Magnetic Resonance Imaging

This work has been published in the *Journal of Magnetic Resonance Imaging.*2015;75(2):845-854) under the title "An Acetone Based Phantom for Quantitative Diffusion Magnetic Resonance Imaging"

5.1 Abstract

Purpose: The purpose of this study was to propose and evaluate an acetone-D_2O phantom which has extended range of ADC for quantitative diffusion MRI, as well as to compare its properties to previously described water-based phantoms.

Materials and Methods: The proposed acetone-D_2O, and previously described sucrose water solution and PVP water solution phantoms were constructed in a number of concentrations between 0% and 50%. At 1.5T field strength, diffusion-weighted MR spectroscopy (DW-MRS) based on a point resolved spectroscopy (PRESS) acquisition, non-diffusion-weighted stimulated echo acquisition mode (STEAM)-MRS and diffusion-weighted echo-planar imaging (DW-EPI) were used to evaluate each phantom. The MR spectra, diffusion-weighted signal decay pattern, tunability of ADC, and ADC range of each phantom were all evaluated.

Results: When placed in an ice-water bath, all phantoms provided desirable signal properties, including single-peak signal with Gaussian diffusion and tunable ADC. At 0^oC, however, water-based phantoms had ADC limited to less than $1.1 \cdot 10^{-3}$ $mm^2 \cdot s^{-1}$ ($0.2\text{-}1.1 \cdot 10^{-3}$ $mm^2 \cdot s^{-1}$) while the proposed acetone-based phantom had ADC values spanning a wider range ($0.6\text{-}3.5 \cdot 10^{-3}$ $mm^2 \cdot s^{-1}$).

Conclusion: The proposed acetone-D_2O phantom provided desirable signal properties over a wide range of ADC with temperature controlled using an ice-water bath.

Keywords: quantitative diffusion MRI, phantom, polyvinylpyrrolidone (PVP), acetone, D_2O, apparent diffusion coefficient (ADC)

5.2 Introduction

Quantitative diffusion MRI has been the subject of intensive research developments that seek to improve data acquisition as well as diffusion signal modeling and reconstruction[77,164–168]. There is an emerging body of evidence demonstrating the potential of quantitative diffusion MRI techniques for diagnosis, staging and treatment monitoring of cancer in multiple organs[81,82,169,79,170–176]. Unfortunately, widespread dissemination and application of quantitative diffusion MRI has been limited. Large variations in measured diffusion parameters have been observed between studies and research sites in both pathological and normal tissues[49,79–84]. The potential sources of these variations include physiological variations such as motion and the presence of fat[97]. Other sources of variability include hardware imperfections such as image distortions caused by susceptibility[177] and eddy currents[178], as well as b-value error[99] from imperfect gradient amplitude calibration[179]. In order to characterize the effect of these technical confounding factors, it is highly desirable to develop a phantom that provides accurately known reference apparent diffusion coefficient (ADC) values that are unconfounded by the presence of physiological motion, the presence of fat, or diffusion modeling mismatches.

Early phantoms[180] for diffusion MRI were constructed using different pure substances, including water, acetone and various oils[102–105]. These phantoms are easy to construct and reproducible, but provide a very limited number of ADC values. Alternatively, solution phantoms have been proposed. In these phantoms, water serves as the solvent and provides the MRI signal. Its diffusion behavior is tuned by dissolving a solute that reduces the ADC of water in a concentration dependent manner. Two important examples of solution phantoms include designs based on sucrose[105,106] and polyvinylpyrrolidone (PVP)[98,107], each dissolved in water. A major challenge with these phantoms is that solutes such as sucrose and PVP generate MR signal with multiple spectral peaks[181,182]. Although preliminary studies have examined the properties of these phantoms[98,100,106–108], comprehensive validation is still required to rule out possible confounding effects from the solute signal on the measured ADC.

An essential component of any diffusion phantom is temperature control because the diffusion of liquids such as water is highly dependent on temperature[109]. For this reason, the use of ice-water baths has become a well-accepted means to maintain the temperature of a diffusion phantom[99] at a highly reproducible temperature (0°C). Unfortunately, water has limited ADC (ADC<1.1 $\cdot 10^{-3}$ $mm^2 \cdot s^{-1}$)[109] at 0°C, while ADC in tissue may be up to 2.6 $\cdot 10^{-3}$ $mm^2 \cdot s^{-1}$ at body temperature[110]. Although scanning water-based phantoms at higher temperatures (e.g., 37.5°C) is possible[183], accurate control at such temperature is very challenging compared with temperature control at 0°C.

In this work, we propose a diffusion phantom design using acetone as the signal source. Compared to water, acetone has very high ADC (e.g., ADC>3.0 $\cdot 10^{-3}$ $mm^2 \cdot s^{-1}$ at 0°C)[184]. Further, it has been shown that in a mixture of water and acetone, the diffusion coefficient of acetone can be lowered due to hydrogen bonding between water and acetone[185,186]. Unfortunately, acetone-water mixtures produce MR signals from both acetone and water (i.e., two spectral peaks with different diffusion properties), which will confound quantitative diffusion MRI measures. To avoid water signals, we propose to substitute water with deuterium oxide (D_2O) as the solute. In the proposed phantom, D_2O alters the ADC of acetone the same way as H_2O without producing any MR-visible signal. Because of high ADC of acetone at 0°C, the proposed phantom may reach the entire physiological ADC range ($0.6 \cdot 10^{-3}$ $mm^2 \cdot s^{-1}$ -$2.6 \cdot 10^{-3}$ $mm^2 \cdot s^{-1}$) under ice-water bath temperature control.

Therefore, the purpose of this study was to propose and evaluate an acetone-D_2O phantom for quantitative diffusion MRI, as well as to compare its properties to previously described water-based phantoms.

5.3 Methods

Phantom Construction

Previously proposed water-based solution phantoms, as well as the acetone-based phantom design proposed in this work were constructed without any doping agents, as follows:

Sucrose phantom: a sucrose phantom was constructed using an agar gel matrix following the recipe described by Lavdas et al[100]. In the five vials constructed, the concentrations of sucrose (Sigma-Aldrich, St. Louis, MO) were 0%, 10%, 20%, 30%, 40% weight/volume (w/v), dissolved in deionized water.

PVP phantom: six vials were built with PVP (Sigma-Aldrich, St. Louis, MO) at concentrations of 0%, 10%, 20%, 30%, 40%, 50% w/v, dissolved in deionized water. Similar to the work by Pierpaoli et al[98]., other components included sodium chloride which modifies the phantom's dielectric properties (9g/L) and sodium benzoate as a preservative (3mM). These ingredients were added to conform to the recipe.

Acetone-D_2O phantom: the proposed acetone-D_2O phantom was built by mixing pure acetone and D_2O (Sigma-Aldrich, St. Louis, MO) with the following concentrations of D_2O: 0%, 5%, 10%, 20%, 40% v/v, mixed in acetone. Additionally, an acetone-H_2O phantom was built with the same concentrations of H_2O for comparison.

All phantoms were stored in glass vials (Sigma-Aldrich, St. Louis, MO) 9.5 cm in height and 2.75 cm in diameter.

Study of Phantom Properties of Interest

Imaging and spectroscopic data were acquired to examine the following properties of each diffusion phantom:

1) *Single-peak MR spectrum*. Phantoms with multiple MR spectral peaks will result in severe chemical shift artifacts[187] in single shot echo-planar imaging (EPI)-based diffusion MRI, therefore a single-peak MR spectrum is highly desirable. Single-voxel multi-echo stimulated echo acquisition mode (STEAM)-MRS and diffusion-weighted (DW)-MRS[96] were performed to study the MR spectrum of phantoms as well as the diffusion of each chemical species.

2) *Reproducible diffusion behavior*. Due to the sensitivity of diffusion to changes in temperature, temperature control is required for reproducible diffusion behavior. An ice-water bath was used in order to attain reproducible diffusion behavior in DW-MRS and DW-EPI experiments. Temperature was monitored using a fiber optic thermometer as described below.

3) *Isotropic Gaussian diffusion.* Validation in the setting of Gaussian diffusion is a first and necessary step in the validation of all diffusion MRI techniques. Isotropic Gaussian diffusion is generally expected when diffusion is unhindered by any spatial restrictions (e.g., cell boundaries).

However, in solutions where hydrogen bonding exists, a distribution of diffusion rates may arise (i.e., spins involved in hydrogen bonds may diffuse at a different rate compared to spins that are not involved in hydrogen bonds)[188]. Given the presence of hydrogen bonding in the solution phantoms analyzed in this study, it is unknown whether this effect could lead to non-Gaussian diffusion behavior. To examine whether the assumption of Gaussian diffusion holds, DW-EPI was performed. The presence of mono-exponential signal decay with increasing b-values was tested as a surrogate of Gaussian diffusion behavior (When spins undergo Gaussian diffusion, signal acquired with increasing diffusion encoding, i.e., b-values, will experience a true mono-exponential decay) as follows. In this study, to validate mono-exponential diffusion decay, one ADC of each phantom was measured from DW-EPI images with two small b-values, while another from two large b-values respectively. Should two ADC measurements agree, this would support the presence of Gaussian diffusion. Additionally, DW-EPI data were acquired with multiple diffusion gradient durations. The agreement between ADC calculated using these different diffusion gradient durations was evaluated for additional validation of Gaussian diffusion. Although we expected the phantom to exhibit isotropic diffusion, all acquisitions were repeated with X, Y, Z diffusion directions, to test the reproducibility of ADC measurements with respect to diffusion direction.

4) *Tunable ADC values*. ADC measured from DW-EPI data was also used to test the feasibility of tuning ADC values and investigate the range of ADC tuning capacity of the solute. To determine the feasibility of ADC tuning by changing concentration of the solute (sucrose, PVP and D_2O, respectively) in the phantoms, ADC measured in multiple vials with increasing solute concentrations (as described above) were compared for each type of phantom.

5) *Wide range of ADC.* The attainable ADC values should cover the entire clinically relevant range ($0.6 \cdot 10^{-3}$ - $2.6 \cdot 10^{-3}$ $mm^2 \cdot s^{-1}$)[110]. The range of ADC values measured from DW-MRS and DW-EPI data of each phantom was evaluated.

The temperature control setup (ice-water bath), acquisition parameters and data processing for imaging and spectroscopic experiments are described in detail in the ensuing paragraphs.

Ice-water Bath

MR experiments were conducted in an ice-water bath for all phantoms. Additionally, the same experiments were repeated at room temperature for the sucrose and PVP phantoms in order to extend their ADC range.

The ice-water bath was conducted in a plastic container of dimensions 20cm×14cm×10cm. A layer consisting of 125ml of ice was formed in the bottom of the container, with approximately 250ml of cold water mixed with the ice, in order to immerse the vials completely. Vials with high concentrations of MnCl2 (approximately 10 mM), and therefore with no visible MR signal, were used to hold the vials of interest in place. Two separate fiber optic thermometer probes were securely placed within the ice-water bath (between the phantom vials), and the average of their measurements was used to monitor temperature changes during the scan.

Signal arising from the ice-water bath was eliminated by adding manganese chloride (2mM) to shorten the T_2 to less than 5ms[189]. This was necessary because a significant chemical shift can cause overlap between acetone and surrounding water in diffusion weighted-echo planar imaging (DW-EPI).

Data Acquisition

MRS and MRI data were acquired to examine the properties of each diffusion phantom. All experiments were conducted in a clinical 1.5T MRI system (HDxt, GE Healthcare, Waukesha, WI) magnet using a standard 8-channel cardiac phased array coil.

DW-MRS: DW-MRS based on a point resolved spectroscopy (PRESS) acquisition[96] was performed in each vial within each phantom, using b-values 0, 100, 250, 500, 750, 1000, 1500 s/mm^2, including flow compensation for diffusion encoding gradient. Other parameters include voxel size= 13mm×13mm×28mm, TE=146ms, TR= 2000ms, NEX=8, diffusion gradients applied in the S/I direction.

Multi-TE STEAM: To sample the MR spectrum without heavy T_2 or diffusion weighting, STEAM-MRS[150] was acquired with multiple short echo times. STEAM-MRS parameters included multiple TEs=8.6, 13.6, 18.6, 23.6, 28.6ms, voxel size=13mm× 13mm× 27.8mm, TR= 2000ms, mixing time (TM)=5ms. Multi-TE STEAM was acquired once in each vial within each phantom.

DW-EPI: DW-EPI was performed on all the phantoms using a dual spin-echo single-shot EPI sequence. Acquisition parameters included TR=6000ms, TE=100ms, FOV=34cm×17cm, matrix size=128×64, slice thickness=6 mm, number of slices=4, slice in axial plane, no parallel imaging acceleration. b=0, 100, 300, 500, 750, 1000, 1250s/mm^2 (the same as those used for DW-MRS). The diffusion gradient duration was 25.3ms and diffusion time was 31.3ms. For the purpose of validating reproducibility of ADC against the changes in diffusion gradient duration, DW-EPI acquisitions with b = 0, 100, 300, 500 were performed with diffusion gradient durations of 18.6ms, 25.3ms and 31.1ms and diffusion times of 24.6ms, 31.3ms and 37.1ms, respectively. Separate acquisitions were also performed using the same b-value combinations, but with diffusion gradients applied in the X, Y, and Z directions, respectively.

Data Processing and Analysis

DW-MRS: At each b-value, solute and solvent signal in each phantom were estimated individually when both signals could be detected with sufficient amplitude (i.e., when the amplitude of the smaller signal peak was no less than 10% of the larger peak). This was performed for the purpose of measuring individual ADC of each chemical species. Signal estimation was performed by fitting the spectrum to a linear combination of Lorentzian spectral shapes[190]. Individual ADC values were measured for the solvent and the solute signal separately by fitting their signal decay over b-values to a mono-exponential curve. When the solute signal was too weak or absent, only the solvent ADC was measured.

Multi-TE STEAM: Single-voxel spectroscopy data using a multi-TE STEAM pulse sequence were displayed to visualize the presence of MR spectral peaks from all chemical species in each phantom.

DW-EPI: A circular region-of-interest (ROI) of size 0.85cm^2 located on the central slice was used to measure the average signal acquired at each b-value for sucrose (40%), PVP (50%), acetone-D_2O (40%) phantoms. Two separate ADC values were measured by fitting the ROI signals from two small b-values (b=0, 500 s/mm^2) and two large b-values (b=750, 1250 s/mm^2), respectively, to a mono-exponential decay signal model. The two ADC measurements were compared. Using two b-values is not the optimal way to estimate ADC accurately, but here two combinations of b-values were used to confirm mono-exponential signal decay (i.e., Gaussian diffusion).

In order to optimally estimate ADC from each vial, using each diffusion acquisition protocol (diffusion direction, diffusion gradient duration and diffusion time), DW-EPI based ADC measurements were also performed from all b-values (using mono-exponential least-squares fitting) on a voxel by voxel basis. A single ADC value was calculated for each vial in each acquisition protocol by averaging ADC values inside a ROI of size 0.85cm^2 on the central slice.

The feasibility of ADC tuning and the range of ADC were determined using ADC values obtained from DW-EPI data acquired with all b-values and diffusion gradient duration of 25.3ms, diffusion time of 31.3ms.

The DW-EPI based ADC measurements in sucrose (40%), PVP (50%) and acetone-D_2O(40%) phantoms were compared across different diffusion gradient durations as well as diffusion direction for additional validation for Gaussian diffusion.

Relaxometry of the Acetone-D_2O Phantom

In order to assess the relaxation properties of the proposed acetone-D_2O phantom, T_1 and T_2 were measured for each vial. To measure the T_1 of the acetone-D_2O phantom in ice-water bath, 2D fast spin echo-inversion recovery (FSE-IR) was performed in the axial plane. Acquisition parameters included inversion times (TI) of 400, 800, 1200, 1600, 2200, 3000ms, TE=400ms (a long TE was used in order to avoid signals from the surrounding doped ice-water bath), FOV=24cm×24cm, slice thickness=10mm, TR=10,000ms. A T_1 map was calculated by fitting inversion recovery signal model to the signals[191] on a pixel-by-pixel basis. For each vial, a single T_1 was measured by the by averaging T_1 measurements in a circular ROI of 73.8cm^2 chosen in the center of each vial.

To measure T_2 of the acetone signal in the acetone-D_2O phantom at 0^{o}C, 2D spin echo (SE) was performed in the axial plane. Acquisition parameters included TE=14, 500, 1250, 2000ms, FOV=24mm × 24mm, slice thickness=10mm, TR=7000ms. For each voxel, a mono-exponential signal model was fit on a pixel-by-pixel basis to estimate T_2 maps. For each vial, individual T_2 estimates were averaged over a circular ROI of 73.8cm^2.

The Effect of Manganese Chloride on Temperature of ice-water Bath

Adding a doping agent ($MnCl_2$) to the ice-water bath may lead to undesired deviation of temperature from 0°C. To study this potential effect, a container of ice-water was doped with several $MnCl_2$ concentrations (0mM, 0.5mM, 1mM, 1.5mM, 2mM). For each concentration, 80 ml of ice-water as well as the corresponding weight of $MnCl_2$ were mixed in a beaker roughly 7cm in height and 5cm in diameter. The temperature of the resulting ice-water bath was measured using a fiber optical thermometer at the ice-water interface, and this measurement was repeated 10 times.

Statistical Analysis

Linear regression of the measured temperature and known concentration of $MnCl_2$ was performed to characterize ice-water temperature with respect to $MnCl_2$ concentrations used in this experiment.

5.4 Results

Study of Phantom Properties of Interest

1) *Single-peak MR spectrum:* Representative DW-MRS and STEAM-MRS spectra of the sucrose phantom (40% sucrose) at 0°C and at room temperature are shown in Figure 5.1. The STEAM-MRS spectra, acquired with short echo times (TE between 8.6ms-28.6ms), show both water and sucrose signal at both temperatures. At 0°C, sucrose signal was not observed in the DW-MRS spectrum, which was acquired at long echo time (TE=146ms). At room temperature, two sucrose peaks were observed in DW-MRS, one on each side of the main water peak. These peaks demonstrated slower decay than the water peak with increasing b-values, due to the slower

diffusion of sucrose compared with water, i.e., the diffusion signal from this phantom has multiple components, each with different ADC values.

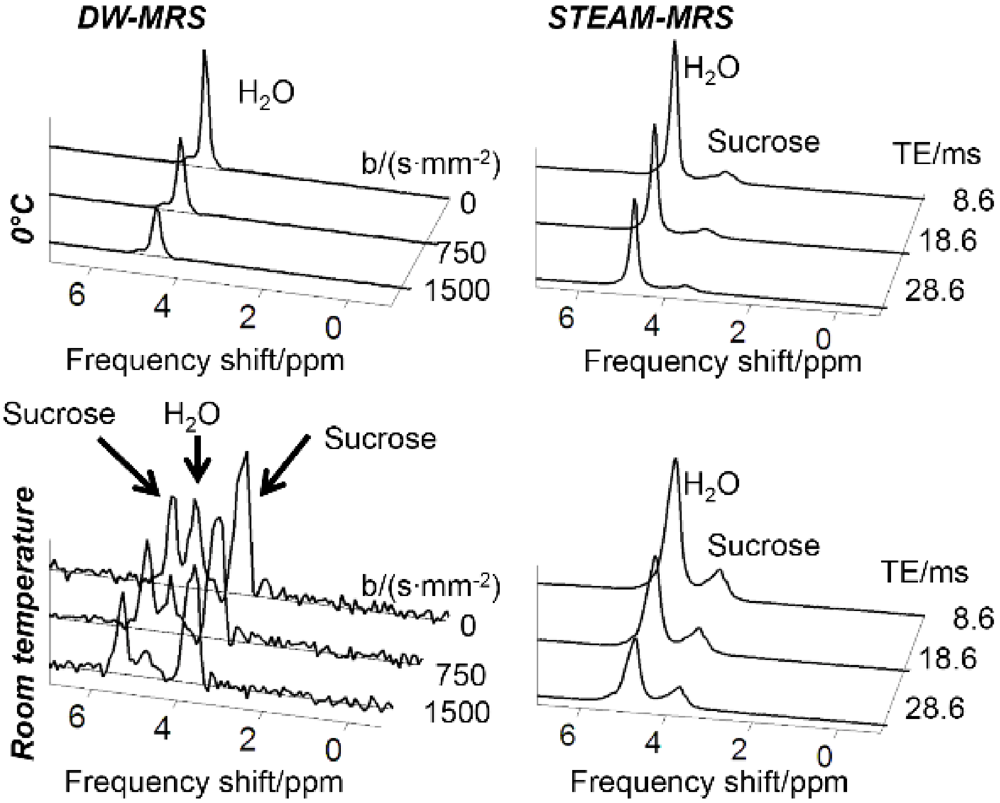

Figure 5.1 Using DW-MRS, sucrose signal was observed in a sucrose phantom at room temperature but not at 0°C. Shown are DW spectra (TE=146ms) as well as short-TE non-DW STEAM spectra of a sucrose phantom (40% sucrose in water solution), both in an ice-water bath (0°C) and at room temperature. At room temperature, sucrose signal was found in STEAM-MRS and DW-MRS. In DW-MRS the high signal is likely due to long sucrose T2. This high sucrose signal complicates the use of room temperature sucrose phantoms for quantitative diffusion MRI. However, no apparent sucrose signal was observed at 0°C in DW-MRS despite the sucrose peak shown in STEAM-MRS, hence this phantom may be considered single-peak in ice-water bath when a long echo time is utilized.

Representative DW-MRS and STEAM-MRS spectra of the PVP phantom (50% PVP) at 0°C and at room temperature are shown in Figure 5.2. Using STEAM-MRS, at room temperature two PVP peaks were observed between 2 and 4 ppm[182]. for the TE=8.6ms acquisition. These peaks decay very quickly with increasing TE (i.e., PVP has short T2), and demonstrate near complete decay at TE=28.6ms. A single signal peak was observed in the spectra of 50% PVP phantom using DW-MRS at both temperatures.

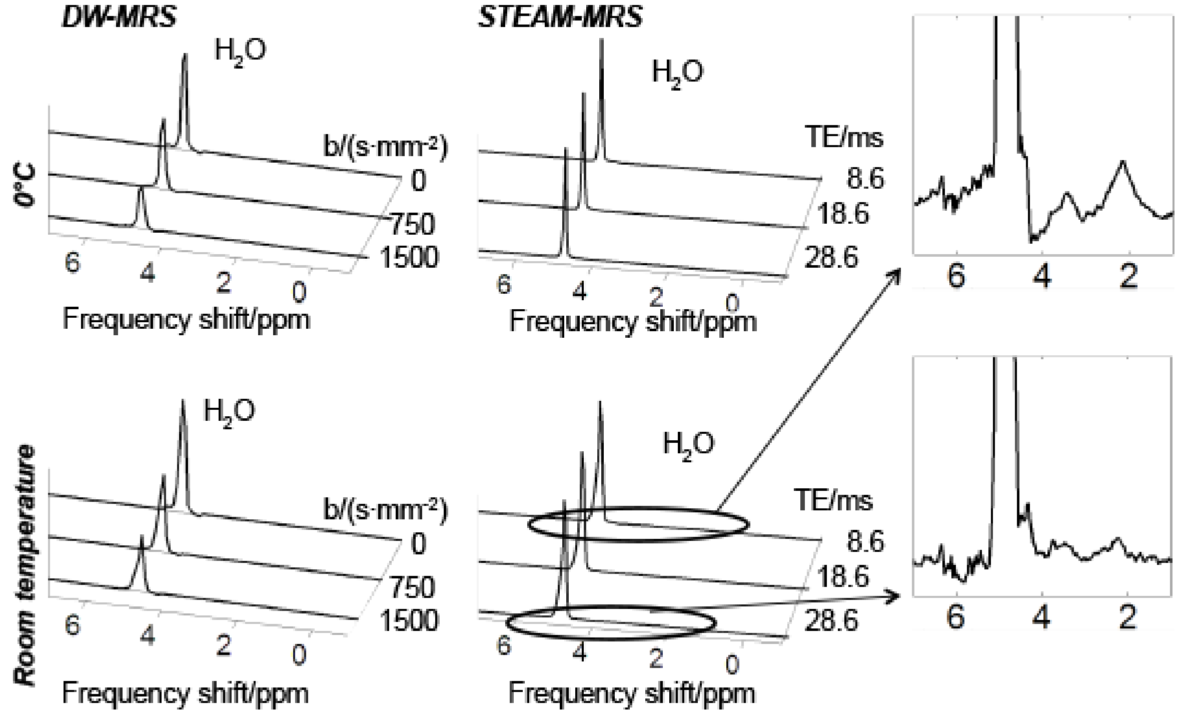

Figure 5.2 PVP phantom shows single peak spectrum in ice-water bath and at room temperature. The plots show DW-MRS (TE=146ms) and STEAM-MRS with no diffusion weighting acquired in the PVP phantom (50% PVP) in an ice-water bath and at room temperature. Nearly single peak spectra were observed in both DW-MRS and STEAM-MRS at both temperatures. After zooming in on STEAM-MRS at room temperature, a fast decaying PVP signal was found at 2-3ppm. This suggests the single-peak spectrum results from the low intensity and rapid decay of the PVP signal at either ice-water or room temperature.

In the acetone-H_2O (20% H_2O) phantom, both acetone and H_2O generate a single MR spectral peak separated by approximately 2ppm (Figure 5.3). However, in the acetone-D_2O (20% D_2O) phantom, only a single spectral peak was observed, due to lack of MR signal from deuterium. The acetone signal decayed at a similar rate (ADC of acetone was measured as $1.21 \cdot 10^{-3}\ mm^2 \cdot s^{-1}$ in acetone-D_2O, $1.43 \cdot 10^{-3}\ mm^2 \cdot s^{-1}$ in acetone-H_2O using DW-MRS), demonstrating that D_2O and H_2O have similar impact on the diffusion of acetone molecules. Note in Figure 5.3 that the H_2O signal in acetone-H_2O creates a ghost image on DW-EPI images, which overlaps with the acetone signal.

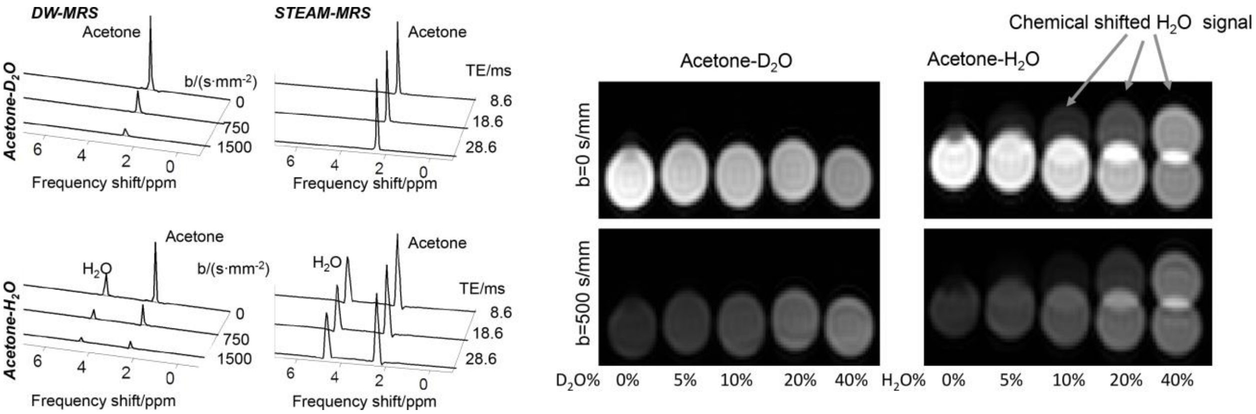

Figure 5.3 Acetone signal showed similar diffusion decay in acetone-D_2O and acetone-H_2O phantom of the same concentration (20% H_2O or D_2O, respectively). The plots show DW-MRS (TE=146ms) and STEAM-MRS of acetone-D_2O and acetone-H_2O phantoms in an ice-water bath. Importantly, H_2O gives rise to a large peak, whereas D_2O produces no NMR signal. Acetone-D_2O and acetone-H_2O phantoms provide similar acetone diffusion signal behavior. However, H_2O produces signal which appears as a ghost in the DW-EPI images, whereas D_2O produces no MR signals.

2) Reproducible diffusion behavior: Temperature was measured between 0.4 °C and 1.75 °C during the scans in ice-water bath.

3) Isotropic Gaussian diffusion: The logarithms of signal decay curves measured by DW-EPI of sucrose (40%), PVP (50%), acetone-D_2O (40%) phantoms in ice-water bath and sucrose, PVP phantoms at room temperature are shown in Figure 5.4. Deviations from a straight line indicate non-Gaussian diffusion behavior. Among the sucrose, PVP and acetone-D_2O phantoms, only the sucrose phantom at room temperature demonstrated substantial deviation ($r^2 = 0.986$) from mono-exponential decay ($r^2 > 0.997$ in other cases). The presence of sucrose signal at room temperature results in clear non-mono-exponential signal decay.

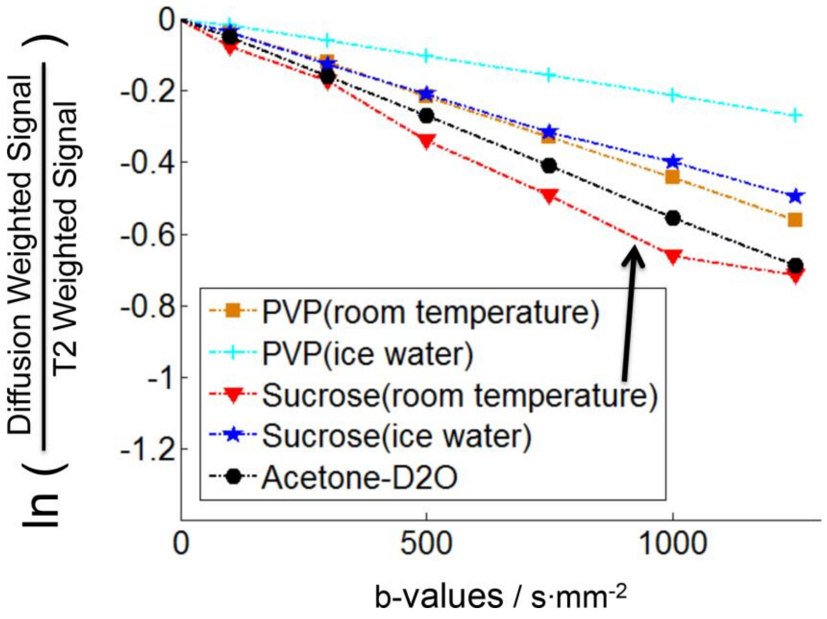

Figure 5.4 PVP phantom and acetone-D_2O phantom showed mono-exponential diffusion signal decay. Color coded lines show the logarithm of relative signal intensity at each b-value for PVP phantom (50%), sucrose phantom (40%), acetone-D_2O phantom (40%). Sucrose phantom's diffusion decay pattern deviates from a mono-exponential model, especially at room temperature (see arrow). Signals were averaged in an ROI ($0.85cm^2$) inside each vial on DW-EPI images.

Further the ADC values measured for each phantom using b=0, $500s/mm^2$ and b=750, $1250s/mm^2$ respectively in DW-EPI are listed in Table 5.1. Sucrose, PVP, and acetone-D_2O, with the exception of the sucrose phantom at room temperature ($\Delta ADC = 0.28 \cdot 10^{-3} mm^2 \cdot s^{-1}$), showed differences smaller than $0.07 \cdot 10^{-3} mm^2 \cdot s^{-1}$ between the ADC values measured using the two sets of b-values (i.e., demonstrating mono-exponential diffusion signal decay).

Phantom	ADC[a]/($10^{-3} mm^2 \cdot s^{-1}$) Measured using b=0,500· $mm^{-2} \cdot s^1$	ADC/($10^{-3} mm^2 \cdot s^{-1}$) Measured using b=750,1250· $mm^{-2} \cdot s^1$	($ADC_{b=0,500}$-$ADC_{b=750,1250}$)/ $ADC_{b=750,1250}$×100%
PVP[b] (Room Temperature) 50% PVP	0.43	0.47	-8.5
PVP (0 °C) 50% PVP	0.20	0.23	-10.7
Sucrose (Room Temperature) 40% Sucrose	0.68	0.4	42
Sucrose (0 °C) 40% Sucrose	0.42	0.36	16.5
Acetone-D_2O 40% D_2O (0 °C)	0.54	0.56	-4.5

a: Apparent diffusion coefficient

b: Polyvinylpyrrolidone

Table 5.1 ADC measured in PVP and acetone-D_2O phantoms, were robust to estimation using different groups of b-values. Specifically, ADC was estimated using a subset of small b-values (0,500· $mm^{-2} \cdot s^1$) and a subset of large b-values (750,1250· $mm^{-2} \cdot s^1$). The difference between these two ADC values in the sucrose phantom indicates signals with multi-exponential decay from multiple signal sources.

ADC values measured using different diffusion gradient durations (Table 5.2) were within a $0.12 \cdot 10^{-3} mm^2 \cdot s^{-1}$ range from each other for all phantoms, and within $0.03 \cdot 10^{-3} mm^2 \cdot s^{-1}$ range for acetone-D_2O and PVP phantoms. The fact that ADC measurements were independent of diffusion gradient duration (and therefore diffusion time) is consistent with Gaussian diffusion behavior.

DW-EPI based ADC measured with all diffusion direction was compared for 40% sucrose phantom, 50% PVP phantom and 40% acetone-D_2O phantom. The measurements were within a

$0.10 \cdot 10^{-3} mm^2 \cdot s^{-1}$ range from each other for sucrose phantom, and within a $0.04 \cdot 10^{-3} mm^2 \cdot s^{-1}$ range for PVP and acetone-D_2O phantoms.

Phantom	Solute concentration %	ADC[a](diffusion gradient duration =18.6ms)	ADC(diffusion gradient duration =25.3ms)	ADC(diffusion gradient duration =31.1ms)
Sucrose (room temperature)	40%	0.61	0.65	0.53
Sucrose(0 °C)	40%	0.37	0.44	0.35
PVP[b] (room temperature)	50%	0.46	0.45	0.43
PVP (0 °C)	50%	0.23	0.23	0.23
Acetone-D_2O	40%	0.55	0.55	0.56

a: Apparent diffusion coefficient

b: Polyvinylpyrrolidone

Table 5.2 ADC ($10^{-3} mm^2 \cdot s^{-1}$) measured from acetone-$D_2O$ phantom, with different diffusion gradient durations (different diffusion times). No monotonic changes in ADC were observed in sucrose phantom with increasing diffusion time. Closely agreeing ADC ($\Delta ADC \leq 0.03 \cdot 10^{-3} mm^2 \cdot s^{-1}$) was measured using different diffusion gradient duration and diffusion time for PVP and acetone-D_2O phantoms.

4) Tunable ADC values and 5) Wide range of ADC: The ADC measurements from DW-MRS and DW-EPI utilizing all b-values from all phantoms are summarized in Figure 5.5. In all phantoms, the ADC of the solvent is tunable by modifying the solute concentration. In the water-based phantoms (sucrose and PVP), the range of achievable ADC is limited to less than approximately $1.1 \cdot 10^{-3} mm^2 \cdot s^{-1}$ at ice-water temperature. In contrast, substantially higher ADC ($3.4 \cdot 10^{-3} mm^2 \cdot s^{-1}$) is achievable in the proposed acetone-D_2O phantom.

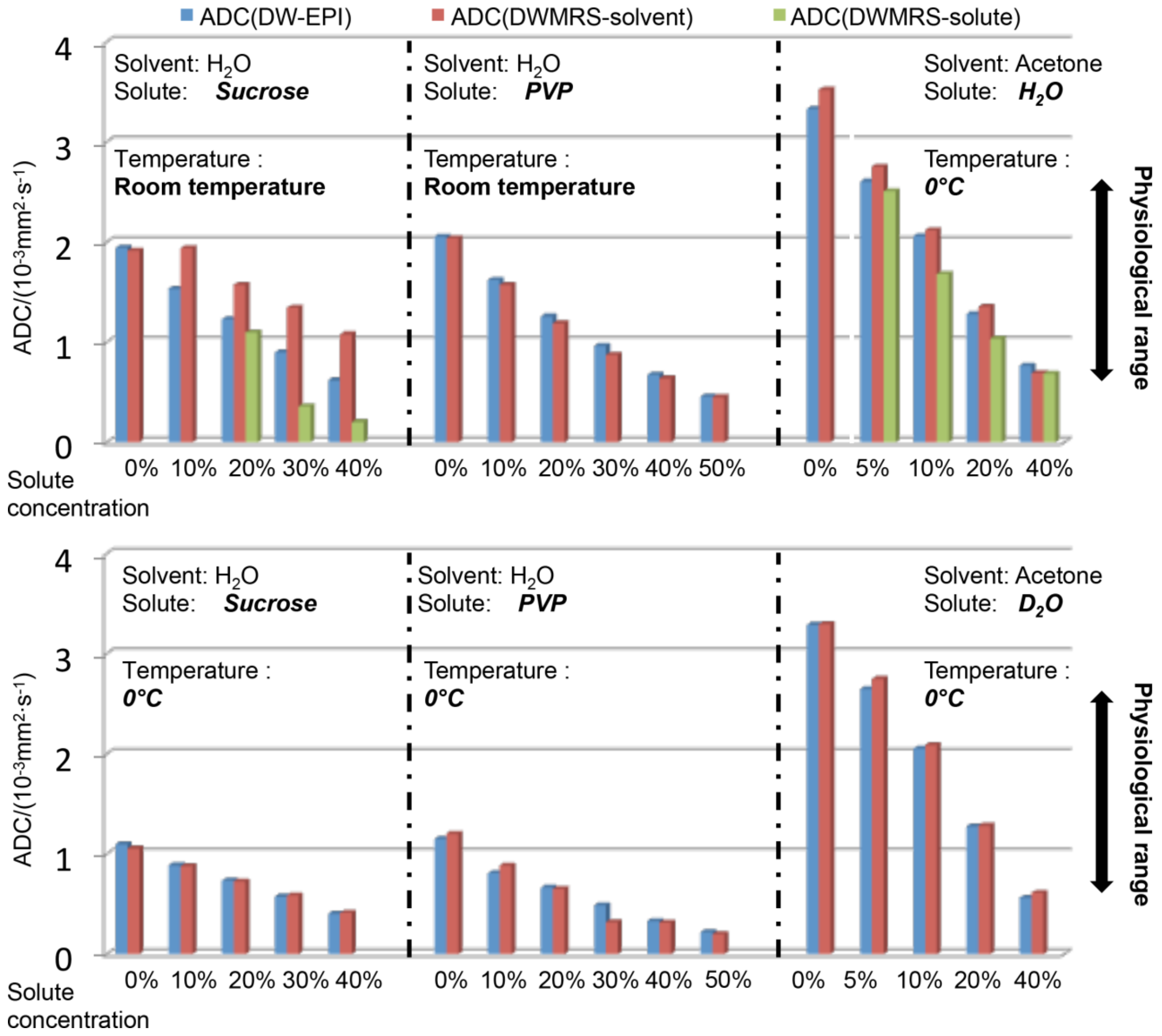

Figure 5.5 The proposed acetone-D_2O phantom covers the entire physiological ADC range at ice-water temperature. In all phantoms, the ADC of the solvent is modulated by the solute concentration. ADC measurements from DW-EPI and DW-MRS are shown for PVP and sucrose phantoms at both room temperature and 0°C, and for acetone-D_2O and acetone-H_2O phantoms at 0°C. Two ADC values were measured by DW-MRS for the solvent and solute signals when the solute signal intensity was high enough. Sucrose and PVP phantoms were limited to low ADC values, particularly when scanned at 0°C, whereas the proposed acetone-D_2O phantom attained a wide range of ADC at 0°C, covering the entire physiological ADC range. In sucrose phantoms at room temperature, although solvent ADC was modulated by solute, the ADC measured by DW-EPI is confounded by the presence of solute signal.

DW-MRS measures two very different ADC for sucrose ($0.13 \cdot 10^{-3}$ $mm^2 \cdot s^{-1}$ with 40% sucrose) and water ($0.72 \cdot 10^{-3}$ $mm^2 \cdot s^{-1}$ with 40% sucrose) in the sucrose phantom at room temperature. The concentration of sucrose as a solute successfully modulated the ADC of H_2O signal measured by DW-MRS at this temperature. However, the ADC measured using DW-EPI ($0.40 \cdot 10^{-3}$ $mm^2 \cdot s^{-1}$ with 40% sucrose) falls between that of sucrose and water measured using DW-MRS, demonstrating explicitly the confounding effect of the solute signal from sucrose, which leads to multi-exponential diffusion decay behavior in DW-EPI.

In the cases without detectable solute signal, ADC measured by DW-MRS and DW-EPI had differences smaller than $0.13 \cdot 10^{-3}$ $mm^2 \cdot s^{-1}$.

T_1 and T_2 of Acetone-D_2O Phantom

The T_1 of acetone was measured using FSE-IR images as 2.41s, 2.59s, 2.60s, 2.65s, 2.61s for acetone-D_2O phantom with D_2O concentrations of 0%, 5%, 10%, 20%, 40%, respectively. In the same phantom, the T_2 of acetone was measured using 2D SE images as 2.30s, 2.42s, 2.42s, 2.53s, 2.39s for D_2O concentrations of 0%, 5%, 10%, 20%, 40%, respectively.

The Effect of Manganese Chloride on Temperature of Ice-water Bath

The temperature measurements obtained in pure ice-water, as well as in doped ice-water with different $MnCl_2$ concentrations are shown in Figure 5.6. The linear regression slope between $MnCl_2$ concentration and temperature was -0.036 with confidence interval (95%) of [-0.08, 0.00].

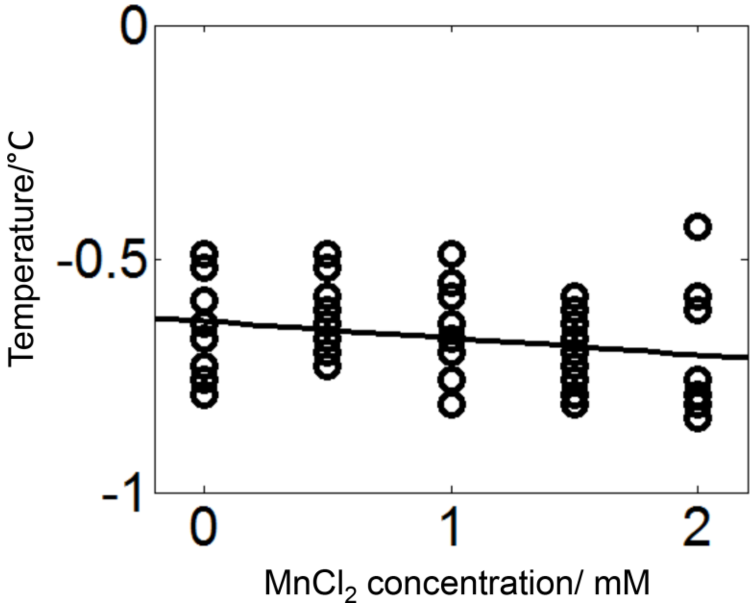

Figure 5.6 No significant linear relationship was observed between $MnCl_2$ concentration and temperature at ice-water interface(P=0.08). Temperature measured at ice-water interface in ice-water doped with $MnCl_2$ with various concentrations. Linear regression was performed with regressand being temperature and regressor being the concentration of $MnCl_2$. A t-test was used to determine whether a linear dependence between temperature and the concentration of $MnCl_2$.

5.5 Discussion

In this study, we have proposed and evaluated a new phantom based on a solution of D_2O dissolved in acetone, and compared its characteristics to previously described phantoms based on water-based solutions of PVP and sucrose, respectively. The proposed acetone-D_2O diffusion phantom overcomes the limited ADC range of water-based phantoms at 0^oC. A physiological range of ADC was achieved using acetone as a signal source (solvent) and D_2O as an MR invisible solute that can be used to modulate the ADC of acetone. In addition to the expanded ADC range, the proposed phantom also has a single-peak MR spectrum, isotropic Gaussian diffusion, and easily tunable ADC. As a result, the proposed design effectively provides a wide range of ADC while minimizing the influence of factors such as temperature, chemical shift artifacts in EPI as well as model mismatch caused by multiple signal sources. Therefore, the proposed phantom may prove useful in the development and quality assurance of quantitative diffusion MRI techniques.

Our observations of mono-exponential signal decay with increasing b-value and ADC measurements independent of diffusion time support our hypothesis that hydrogen bonding between the solvent and the solute maintains Gaussian diffusion in the acetone-H_2O phantom, acetone-D_2O phantom as well as sucrose and PVP phantoms. The non-mono-exponential decay observed in sucrose phantom at room temperature can be explained by the confounding effect of sucrose signal contributing to multi-exponential signal decay.

At 0°C, sucrose and PVP phantoms showed a single-peak spectrum, Gaussian diffusion, and easily tunable ADC. However, at 0°C the span of ADC values was limited to equal or less than the ADC of pure water[109] at 0°C, $\sim 1.1 \cdot 10^{-3}\ \mathrm{mm}^2 \cdot \mathrm{s}^{-1}$. One way to extend ADC range of water-based phantom is to image them at higher temperatures. At room temperature, the ADC range of the water-based sucrose and PVP phantoms was higher than at ice-water temperature. However, at room temperature, signal from sucrose was observed. This leads to multi-exponential diffusion signal decay, which confounds DW-EPI of sucrose phantoms at room temperature. In contrast, no significant signal from PVP was observed at echo times used for DW-EPI and DW-MRS, even at room temperature. Although at shorter echo times, PVP signal was observed at room temperature, the rapid decay indicates very short T_2 of PVP compared with water. This likely led to the lack of PVP signal in DW-EPI and DW-MRS that are typically acquired at much longer echo times. For this reason, the PVP phantom demonstrated mono-exponential signal decay with increasing b-values, in good agreement with previous studies[98,107]. Nevertheless, the main limitation for water-based phantoms at higher temperatures is the need for temperature control more sophisticated than ice-water bath, in order to attain reproducible ADC measurements[183]. This requirement introduces significant complexity into the phantom setup, and may limit the widespread applicability of water-based phantoms at higher temperatures. Therefore, the proposed acetone-D_2O phantom may provide an effective approach to obtain a wide ADC range with simple ice-water temperature control.

This study had several limitations. First, the use of acetone poses some challenges. It is often desirable to tune the T_1 and T_2 of phantoms, in order to better mimic tissue properties and to optimize SNR. Certain salts such as copper sulfate and nickel chloride are commonly used to shorten the T_1 and T_2 of water. However, neither of these are soluble in acetone. Alternative agents that alter the relaxivity of acetone may address this limitation, and further investigation is needed to optimize the relaxation parameters of acetone. Another limitation of the proposed acetone-D_2O phantom is the need to eliminate the signal from the surrounding ice-water bath. In this study, $MnCl_2$ was added to the ice-water bath for this purpose. Importantly, this process does not result in substantial changes in the ice-water temperature.

Further, the potential for proton and deuteron exchange between D_2O and acetone may limit the shelf-life of the proposed phantom by generating unwanted water signal. In preliminary results, an H_2O peak appears at the fourth month after the phantom construction if stored at room-temperature. However, when acetone-D_2O was stored in a freezer, no H_2O peak was detected a year after the construction of the phantom. However, systematic evaluation of the shelf life of the proposed acetone-D_2O phantom needs to be performed in future studies.

To demonstrate the utility of the proposed phantom for the validation of diffusion MRI techniques, multi-center studies must also be performed[107]. Reproducibility across sites, field strengths and platforms is critical for the establishment of quantitative diffusion MRI techniques as quantitative imaging biomarkers. Diffusion MRI phantoms used in multi-site reproducibility studies need to show reproducible diffusion behavior over time and across sites.

In conclusion, this study has proposed and characterized the performance of an acetone-D_2O diffusion phantom. This phantom provides single-peak MR spectrum, Gaussian diffusion behavior and a wide range of tunable ADC, covering the entire physiological range of ADC values at 0^oC. This phantom may have utility for the technical development of new diffusion MRI methods and for protocol harmonization and quality assurance in multi-center studies using quantitative diffusion MRI.

5.6 Acknowledgement

The authors wish to acknowledge support from the NIH (R01 DK083380, R01 DK100651, K24 DK102595), as well as the University of Wisconsin D2P Igniter Program. We thank Orhan Unal for assistance with the temperature probe for phantom experiments.

Chapter 6 : Phase-based T_2 Mapping with Gradient Echo Imaging

This work has been submitted to the *Magnetic Resonance in Medicine*. under the title "Phase-based T_2 Mapping with Gradient Echo Imaging"

6.1 Abstract

Purpose: Transverse relaxation time (T_2) mapping with MRI has a plethora of clinical and research applications. Current T_2 mapping techniques are based primarily on spin-echo (SE) relaxometry strategies that rely on the signal magnitude, and often suffer from lengthy acquisition times. In this work we propose a phase-based T_2 mapping technique where T_2 information is encoded into the signal phase of rapid gradient echo (GRE) acquisitions.

Theory: Bloch equation simulations demonstrate that the phase of GRE acquisitions obtained with a very small inter-repetition RF phase increment has a strong monotonic dependence on T_2, resulting from coherent transverse magnetization. This T_2-dependent phase behavior forms the basis of the proposed T_2 mapping technique. To isolate T_2-dependent phase from background phase, at least two datasets with different RF phase increments are acquired. The proposed method can also be combined with chemical shift encoded MRI to separate water and fat signals.

Methods: The feasibility of the proposed technique was validated in a phantom experiment. In vivo feasibility was demonstrated in the brain, knee, abdomen and pelvis. Comparisons were made with SE-based T_2 mapping, spectroscopy and T_2 values from the literature.

Results: The proposed method produced accurate T_2 maps compared with SE-based T_2 mapping in the phantom. Good qualitative agreement was observed in vivo between the proposed method and the reference. T_2 measured in various anatomies agreed well with values reported in the literature.

Conclusion: A phase-based T_2 mapping technique was developed and its feasibility demonstrated in phantoms and in vivo.

Keywords: magnetic resonance imaging, T_2 mapping, relaxometry, phase, gradient echo, RF spoiling, quantitative imaging biomarker

6.2 Introduction

The transverse relaxation time (T_2) is associated with important microscopic tissue properties such as the concentration and cluster-size of paramagnetic particles and the mobility of hydrogen atoms. Importantly, T_2 is well known to characterize a plethora of important disease processes such as iron deposition, fibrosis, edema, malignancy, and inflammation, among others. As a result, quantitative T_2 mapping with MRI has many applications, including assessment of neuro-degenerative diseases and characterization of malignant lesions[192], detection of myocardial edema[193], detection of chronic rejection after heart transplant[194,195], detection of early cartilage degeneration[196], quantification of liver iron overload[197] and even identification of myofascial trigger points[198].

Spin-echo (SE) based methods are commonly used to map T_2. By varying the echo time and fitting the signals to a mono-exponential decay model (multi-exponential if a multi-component model is appropriate[199,200]), T_2 can be estimated. Unfortunately, lengthy exams are needed due to the long repetition time (TR) to minimize T_1 weighting. Acquisition times can be reduced by acquiring multiple echoes (multi-echo SE) in a single TR[201,202], although the use of multi-echo methods may lead to different measurement of T_2[202].

Magnetization prepared T_2 contrast ("T_2-prep") is a method used to encode T_2 relaxation into the longitudinal magnetization[203]. This technique is advantageous for imaging blood vessels and the heart[13], and relies on modulation of the longitudinal magnetization prior to a readout acquisition. Although faster than SE-based acquisitions, T_2-prep-based T_2 quantification also suffers from relatively long acquisition times[204,205].

Steady-state short TR methods based on spoiled gradient echo (SGRE), balanced-steady state free precession (bSSFP)[112], and gradient-refocused acquisition in the steady-state (GRASS)[113,114] are time efficient compared to spin-echo (SE) T_2 mapping techniques. For example, two SGRE acquisitions with varying flip angle combined with bSSFP contain the necessary information for joint T_1 and T_2 estimation[112]. Due to the use of short TR acquisitions, these methods can deliver simultaneous T_1 and T_2 quantification of spatially resolved 3D volumes within clinically acceptable acquisition times[112].

To further reduce acquisition time for T_2 mapping, Welsch et al. proposed a multi-echo GRE acquisition known as double echo steady-state (DESS)[113]. This approach can also be extended for joint estimation of T_1 and T_2 using the triple echo steady-state (TESS) method proposed by Heule el al[114].. In these methods, T_2 information is encoded into the relative magnitude between echoes. In vivo feasibility of these methods has been demonstrated[201,206]. A variation of the DESS T_2 mapping technique developed by Staroswiecki et al[207]., has also demonstrated potential for accurate in vivo T_2 mapping. Although only a single gradient echo (GRE) acquisition is required, these methods rely on water specific RF pulses for fat suppression, which may be unreliable in the setting of B_0 inhomogeneities[114]. Differential T_2* weighting in the various echoes can also confound T_2 estimates.

We note that none of the above methods exploit signal phase to encode T_2 relaxation. In this work, we propose a major modification of an RF phase scheme first proposed by Zur et al[208] to achieve robust spoiling of transverse magnetization for GRE acquisitions. As we propose below, the use of very small RF phase increments, rather than large RF phase increments needed for RF spoiling, can create T_2-dependent changes in both the phase and magnitude of the GRE signal. In this work we propose a novel quantitative T_2-mapping technique that encodes T_2 information into the phase of the GRE signal by manipulating the RF phase increment.

6.3 Theory

Complete spoiling of transverse magnetization is generally assumed when using spoiled gradient echo (SGRE) acquisitions. RF spoiling is a well-known approach used for spoiling transverse magnetization[116]. As first proposed by Zur et al[208]., RF spoiling methods use a pseudo-random sequence of phase increments of the RF excitation. The phase sequence is defined by the difference between the n^{th} and the $(n+1)^{th}$ RF excitation, i.e.: $\Phi_{RF}(n) = \Phi_{RF}(n-1) + \Phi_0 + n \cdot \Delta\Phi$ (n=0, ….). If the RF phase increment ($\Delta\Phi$) is chosen carefully, transverse magnetization accumulates in an incoherent manner and is effectively spoiled.

The choice of RF phase increment is important for effective RF spoiling. Specific choices of RF phase increment (e.g. 117°) lead to excellent RF spoiling and the signal closely approximates the ideal SGRE signal magnitude[116]. Other choices of RF phase increment may lead to less effective RF spoiling[116]. Importantly, we note that the phase of gradient echo signals in the context of RF spoiling has not been well described.

In this study, we investigate the effects of the RF phase increment on the phase of the complex-valued gradient echo signal. Figure 6.1 plots the results of a Bloch equation simulation showing both the signal magnitude (η) and phase (θ) of the gradient echo signal, using the RF phase increment method proposed by Zur et al[208].. In this computer simulation, an ensemble of 1000 spins periodically experienced a sequence consisting of an RF pulse, T_1 and T_2 relaxation, and at the end of each repetition, a 2π phase dispersion across the isochromats due to an unbalanced readout gradient. Note that the acquisition reference frame matches the excitation phase.

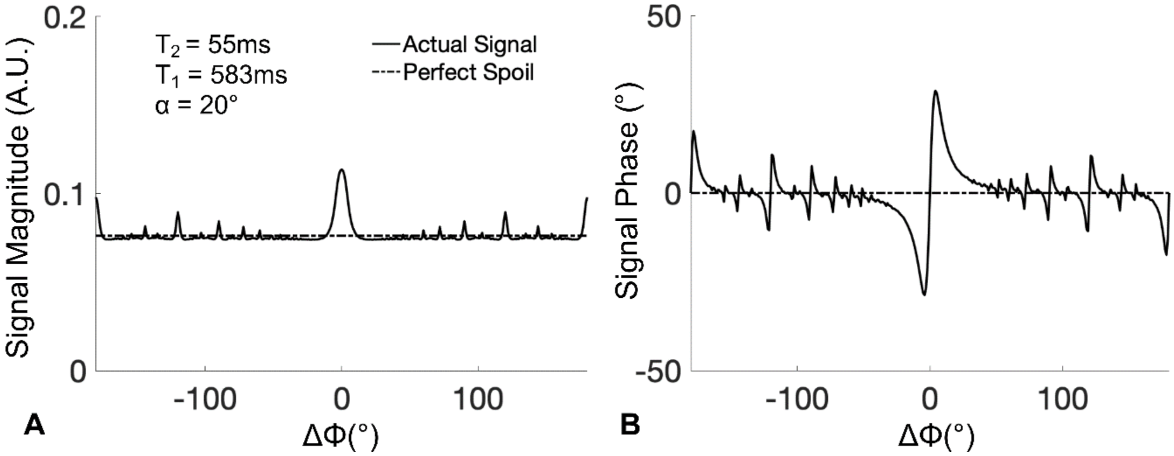

Figure 6.1 GRE signal magnitude (A) and phase (B) over the full range of RF phase increments (ΔΦ), according to the method of Zur et al[208]. By varying the RF phase increment, large variations in the magnitude and phase of the GRE signal are observed. Signal shown in this plot was generated using a Bloch equation simulation assuming T_1=583ms and T_2=55ms to simulate normal liver tissue[21] at 1.5T, with TR=10ms and flip angle=20°.

Figure 6.2 focuses on a narrow range of small RF phase increments, also with varying T_1, T_2 and flip angle. As can be seen in Figure 6.2, significant variations in the signal phase occur with changes in T_2 and flip angle, and to a much lesser extent with T_1. The largest signal phase was observed with small RF phase increments between 1° to 4°. Various combinations of T_2 (25ms, 55ms, 115ms), T_1 (500ms, 900ms, 1400ms) and flip angle (5°, 10°, 15°) are used in the simulation assuming a TR of 10ms and simulated TE of 0ms to ignore the effects of T_2* decay, for simplicity.

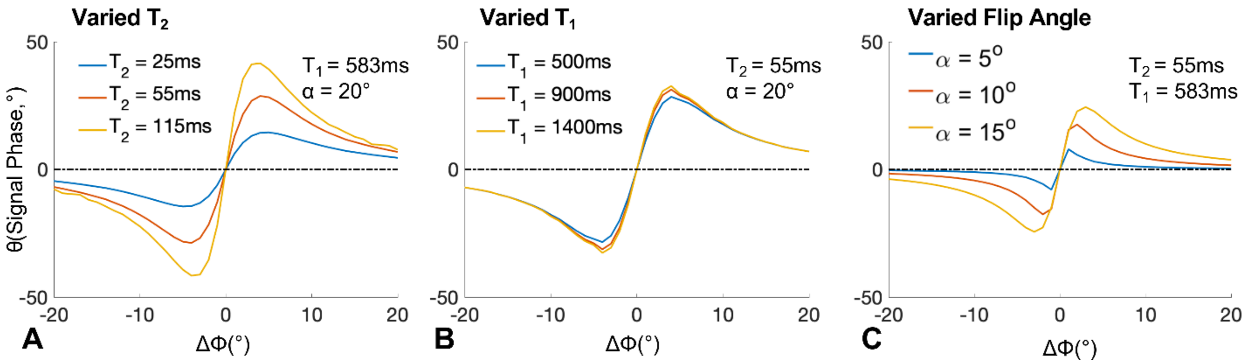

Figure 6.2 GRE signal phase is heavily influenced by T_2 (A), but only minimally by T_1 (B) for very small RF phase increments (ΔΦ), forming the basis for the proposed T_2 mapping method. The phase of the GRE signal over the low range of RF phase increments were generated using Bloch equation simulations with physiological T_1 and T_2 values and TR=10ms. The dotted lines are the case where transverse magnetization is spoiled perfectly.

The effects of T_2, T_1 and flip angle are also plotted in Figure 6.3, demonstrating not only a strong dependence of the signal phase on T_2 and flip angle, but also a relatively weak dependence on T_1. We can express the steady-state gradient echo signal acquired with an RF phase increment as:

$$S(\Delta\Phi, \alpha, TR; M_0, T_1, T_2) = M_0 \cdot \eta(\Delta\Phi, \alpha, TR; T_1, T_2) \cdot e^{i[\theta(\Delta\Phi, \alpha, TR; T_1, T_2) + \theta']} \quad [5.1]$$

where $\eta(\Delta\Phi, \alpha, TR; T_1, T_2)$ is the signal magnitude relative to M_0, $\theta(\Delta\Phi, \alpha, TR; T_1, T_2)$ is the signal phase immediately after excitation and is dependent on T_2, T_1, flip angle (α) and θ', which is the local background phase caused by complex coil sensitivity, eddy currents, magnetic field inhomogeneities, etc.

To the best of our knowledge, simple analytical forms of $\eta(\Delta\Phi,\alpha,TR;T_1, T_2)$ and $\theta(\Delta\Phi, \alpha,TR;T_1,T_2)$ have not been derived. In this work, calculation of these two functions is based on the use of a lookup table. Lookup tables are constructed from Bloch equation simulations based on wide ranges of possible T_1 and T_2 values, and the known acquisition parameters used in the experiment: $\Delta\Phi$, α, TR. All lookup tables used in this work are constructed using the same Bloch equation simulation described above.

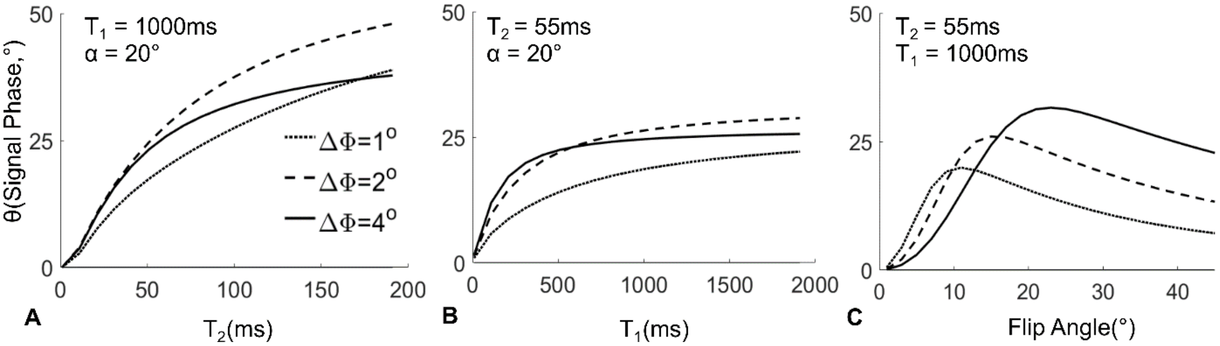

Figure 6.3 GRE signal phase (A) increases monotonically with increasing T_2 for small RF phase increments ($\Delta\Phi$), e.g. 1-4°. Using a small RF phase increment (e.g. 2°), the signal phase is sensitive to T_2 over a wide range of T_2 values, a property that is favorable for encoding T_2 information. Note also that the signal phase is relatively insensitive to varying T_1 (B) and flip angle (for midrange flip angles such as 18°) for phase increments of 1° and 2°. The phase and magnitude of the GRE signal over the low range of RF phase increments were generated using Bloch equation simulations with physiological T_1 and T_2 values and TR=10ms.

Figure 6.3 depicts in greater detail the dependence of the signal phase with respect to T_2, T_1 and flip angle over a few small RF phase increments. A pronounced monotonic increase in the observed phase with T_2 is noted over a wide range of physiological T_2 values[131] with RF phase increments between 1° and 4°. For an RF phase increment of 2°, the signal phase is consistently sensitive to T_2 over a wide range of T_2 values (Figure 6.3A). Unlike the strong dependence on T_2, the signal phase changes minimally over a wide range of T_1 values between 1000ms and 2000ms

(Figure 6.3B). Given these observations, a small RF phase increment such as 2° will encode the tissue T_2 into the signal phase.

In actual MRI acquisitions the received signal phase contains an additional background phase term, i.e.: θ'(Eq. 5.1). Estimates of the signal phase resulting from T_2 of the tissue must be isolated from the background phase. In this work we propose the following method to isolate θ from θ', and subsequently estimate tissue T_2.

Proposed Phase-based T_2 Mapping

In principle, two identical acquisitions with equal and opposite RF phase increments will generate equal but opposite phase responses (Figure 6.2), i.e.: $\theta(\Delta\Phi, \alpha, TR; T_1, T_2) = -\theta(-\Delta\Phi, \alpha, TR; T_1, T_2)$. Using two such acquisitions, θ can be isolated from M_0, η and θ' in Eq.5.1 by taking the phase difference of two gradient echo signals acquired with opposite RF phase increments, and with all other acquisition parameters identical, i.e.:

$$\hat{\theta}(\Delta\Phi, \alpha, \mathrm{TR}; \mathrm{T}_1, \mathrm{T}_2) = (\angle S(\Delta\Phi, \alpha, \mathrm{TR}; \mathrm{T}_1, \mathrm{T}_2) - \angle S(-\Delta\Phi, \alpha, \mathrm{TR}; \mathrm{T}_1, \mathrm{T}_2))/2 \quad [5.2]$$

Using a well-chosen RF phase increment (e.g. $\Delta\Phi$=2 °) and a relatively large flip angle (e.g. α=18 °), the estimated signal phase can be used to estimate T_2. Based on the model presented above, it is expected that only a small error might occur in the T_2 estimate related to T_1 and unanticipated errors in flip angle (Figure 6.3B,C). Note that the same figure shows a maximum signal phase of 50°, which will result in a phase difference of 100° between two signals. This phase difference is well below 2π, suggesting that even with higher T_2 values, there should be no risk of phase wrap in the proposed method.

In this work, we propose to estimate T_2 from $\hat{\theta}$ through the use of a lookup table generated from a Bloch equation simulation that uses the known TR and flip angle of the acquisition. We note that the phase is weakly dependent on T_1, and therefore T_1 values measured using other methods or values reported in the literature for the anatomy of interest can be used to generate the lookup table.

Synthetic T_2-weighted Images

In addition to the phase maps used to generate the T_2 map, magnitude images are also acquired. By multiplying these magnitude images with the inferred T_2 decay from the phase-based T_2 map, synthetic T_2-weighted images can be generated. The synthesis of the signal in each voxel can be expressed as:

$$S_{syn} = |S| \times e^{-\mathrm{TEv}/\widehat{T_2}} \qquad [5.3]$$

where S_{syn} is the synthesized T_2-weighted signal, TE_v is the virtual echo time, S denotes the signal acquired with one (or a combination) of the images acquired at the two phase increments. $\widehat{T_2}$ denotes the estimated phase-based T_2 value.

6.4 Methods

Phantom Experiments

The accuracy of the proposed method was evaluated using a phantom constructed with varying concentrations of agarose and $NiCl_2$ to modulate the T_2 and T_1 relatively independently[209]. The T_1 was varied such that the confounding effect of T_1 variation in the proposed method can be demonstrated. A 4×4 grid of cylindrical vial agarose gel phantom was constructed for this experiment. Each vial is approximately 3cm in diameter and 4.8cm in height. Each column was constructed with a varying concentration of agarose (0.5%, 1%, 2%, 4%) to modulate T_2. Each row is doped with a varying concentration of $NiCl_2$ (0mM, 0.5mM, 1mM, 2mM) to modulate T_1.

All phantom experiments were performed on a clinical 3.0T MRI system (Signa Premier, GE Healthcare, Waukesha, WI) using a high channel density posterior and anterior receive array coil with up to 90 independent coil elements (Air coil, GE Healthcare, Waukesha, WI). Single-echo SE-based T_2 mapping was performed to provide a reference standard. Echo times of 11ms, 50ms, 100ms, 150ms were acquired with TR of 6000ms. Other acquisition parameters include: axial acquisition; field of view (FOV)=18cm×18cm; matrix=128×128; slices=1; slice thickness=15mm; receiver bandwidth=±83.33kHz. Signals were fit to a mono-exponential decay signal model offline in Matlab (MathWorks, Natick, MA) to estimate T_2 on a voxel by voxel basis. A circular ROI was drawn in each vial. The T_2 measurements were averaged in each ROI for comparison with the proposed method.

T_1 maps of the phantoms were generated using inversion recovered fast spin-echo (FSE-IR) MRI. Acquisition parameters were as follows: inversion time=50ms, 500ms, 1000ms, 1500ms, 2500ms, 3500ms, 4000ms; TR=15000ms; FOV=18cm×18cm; matrix=256×256; slices=1; slice thickness=15mm; receiver bandwidth=±25kHz. T_1 estimation was performed on a voxel by voxel basis using the standard inversion recovery signal model[210].

GRE images for phase-based T_2 map were acquired using an axial acquisition; TR=5.0ms; FOV=18cm×18cm×24cm; matrix=128×128×24; receiver bandwidth=±50.1kHz; number of signal averages=4. Two complex GRE datasets with $\Delta\Phi_1=2°$ and $-2°$, each with 18° flip angle were acquired for the proposed method. The sum of squares image was used as a virtual body coil image. The complex sensitivity map was generated using the source images with one RF phase schedule (the first echo if multiple echoes are acquired) and used to combine complex channel images for both sets of images with difference RF phase schedule, and all acquired echoes. This process was used to generate complex coil combined images. T_2 maps were reconstructed as described in the theory section. For the reconstruction of phase-based T_2 maps, a T_1 of 1850ms was assumed (mid-point of the range of the T_1 measured in the phantom, as reported in the Results section).

For each reconstruction by the proposed method, T_2 measurements were averaged in a circular ROI in each vial, on the center slice. Linear regression was used to compare the T_2 measurements obtained using the proposed phase-based method and SE-based T_2 mapping.

In Vivo Experiments

The proposed methods were also evaluated in healthy volunteers to demonstrate in vivo feasibility. All human imaging was performed after obtaining approval from our institutional review board (IRB) and informed written consent. All in vivo experiments were performed on 3.0T clinical MRI systems (abdomen, pelvis, brain experiments on Signa Premier; knee experiments on Discovery MR 750w, GE Healthcare, Waukesha, WI). Various phased array receive coils appropriate for the specific anatomy were used including: 8-channel head coil (brain), 8-channel knee coil (knee) and high channel density posterior and anterior receive array coils with up to 90 independent coil elements (Air coil, GE Healthcare, Waukesha, WI) for the abdomen and pelvis.

For the proposed method, the choice of RF phase increment and flip angle are as follows: $\Delta\Phi = 2°$ and $-2°$, each with an 18° flip angle.

In the knee volunteer experiments, a total of 6 knees were scanned in 4 volunteers (4 males, ages 28-35). The acquisition parameters of the proposed method are as follows: 3D acquisition; sagittal plane; FOV=14cm×14cm×9.6cm; TR=5.9ms; matrix=256×256×32; bandwidth=±90.91kHz; signal averages=3; acquisition time=4:48 minutes. Due to the difficulty of limiting motion over long acquisition times, a commercial multi-echo SE T_2 mapping was used as reference instead of single-echo SE. Acquisition parameters include: sagittal plane; FOV=14cm×14cm; slice thickness=2.7mm; gap=0.3mm; slices=28; TR=1.0s; acquisition matrix=256×256; echo times=8.6ms, 14.8ms, 22.2ms, 29.5ms, 36.9ms, 44.3ms, 51.7ms, 59.1ms; bandwidth=±31.25kHz; signal averages=1; exam time=12:56 minutes. The acquisition volumes of the two methods were precisely colocalized.

Phase-based T_2 maps were reconstructed as described in the theory section. T_1 of 1198ms was assumed (midpoint between the T_1 of the medial femoral cartilage and patella). The reference T_2 map from multi-echo SE images were calculated by fitting the signal to a single-exponential decay model to minimize least square error on a voxel by voxel basis. To compare the proposed method and the reference, T_2 measurements were averaged inside ROIs drawn directly on the T_2 maps in the following regions described by Fang Liu et, al[211]: medial femoral central (MFC) condyle, medial femoral posterior (MFP) condyle, medial tibial plateau (MTP), patella-deep (PAT-D), patella-superficial (PAT-S), lateral femoral central (LFC) condyle, lateral femoral posterior (LFP) condyle, lateral tibial plateau (LTP), as well as T_2 measurements from the gastrocnemius muscle (MUS). For each individual region, box-whisker plots were created to demonstrate the distribution of T_2 measurements by the two compared methods. A Student’s t-test was performed for paired samples. For measurements across all the regions, the Pearson coefficient was computed.

A brain study was performed on one volunteer (male, age 30). The acquisition parameters of the proposed method were as follows: 3D acquisition; axial plane; FOV=24cm×24cm×12.8cm; TR=5.6ms; acquisition matrix=256×256×32; bandwidth=±90.91kHz; signal averages=3; exam time=4:30 minutes. Single-echo SE T_2 mapping was used as reference for T_2 measurements, acquisition parameters include: axial plane; FOV=24cm×24cm; slice thickness=3.6mm; slice spacing=0.4mm; number of slices=22; TR=6s; acquisition matrix=256×256; echo times=11ms, 70ms; bandwidth=±31.25kHz; signal averages=1; acquisition time=24:00 minutes. The acquisition volumes of the two methods were precisely colocalized.

Phase-based T_2 maps were reconstructed as described in the theory section. T_1 of 915ms was assumed (midpoint between the T_1 of white matter and the putamen at the age of 20)[212]. The reference T_2 map was reconstructed using least square error fitting to a single-exponential model. Synthetic T_2-weighted images were also generated with virtual TE values of 70ms and 100ms as described in the theory section.

For imaging in the abdomen and pelvis, separation of water and fat signals was performed by combining the proposed method with a multi-echo 3D GRE chemical shift encoded (CSE) acquisition. Abdomen (male, age 54) and pelvis (male, age 47) experiments were conducted on one volunteer. The acquisition parameters in the abdomen included: axial plane; FOV=40cm×32cm×26cm; TR=6.5ms; acquisition matrix=100×80×26; 5 echoes with echo times=0.9ms, 2.0ms, 3.0ms, 4.0ms, 5.1ms; bandwidth=±100kHz; signal averages=1; exam time=20 seconds in a single breath-hold. In the pelvis, the same acquisition parameters were used with the following exceptions: slice thickness=8mm; slices=32, TR=6.4ms; bandwidth=±90.91kHz; exam time of 25 seconds in a breath-hold.

For the image reconstruction, the proposed method was combined with CSE-MRI. Using complex fitting with single R2* least-squares fitting reconstruction[123] from the ISMRM Fat-Water Toolbox[151](http://ismrm.org/workshops/FatWater12/data.htm), water and fat signals were separated. The magnitudes and phases of each chemical species were then used to reconstruct individual T_2 maps for each chemical species.

Single voxel multi-TE stimulated echo acquisition mode (STEAM)-MR spectroscopy[150] (MRS) was acquired in the liver and the spleen to provide reference values for phase-based T_2 measurements. STEAM-MRS data was acquired with the following parameters: TR=3500ms; TE=10ms, 15ms, 20ms, 25ms, 30ms; number of points=2048; spectral width=5000Hz; 5ms mixing time. The voxel size was 15mm×15mm×20mm in the liver and 15mm×15mm×10mm in the spleen. Signal magnitude as well as T_2 of water and fat signal was estimated jointly using non-linear least square fitting[213].

Simulation experiment to evaluate the sensitivity of phase to motion:

Although no apparent effect of motion was observed in vivo (below), it is well known that GRE acquisitions with unbalanced gradients and no RF spoiling (i.e. unspoiled GRE) can be sensitive to motion[214,215]. In the presence of unbalanced gradients, moving spins will accrue a different phase during each TR. This phase accrual may impact the T_2-dependent phase of the method proposed in the current work, potentially confounding T_2 measurements.

For the proposed method, phase accrual resulting from the unbalanced readout gradient is a linear function of the voxel location. Assuming that the phase dispersion from the unbalanced gradient is 2π across the voxel in the readout direction, the additional phase accrual from the overall voxel can be written as: $n \times TR \times Vx \times 2\pi/\Delta X$, for a voxel moving from the image isocenter, where Vx is the velocity of the voxel in the readout direction and ΔX is the voxel dimension in the readout direction. This effect potentially confounds quantification of the phase shift used to encode $T_{2.}$

To assess the magnitude of velocity effects on T_2 quantification, we performed a Bloch equation simulation experiment where the effects of the first order motion (velocity) in the readout direction were modeled. This simulation was performed using a modification of the simulation described in the Theory section. In addition to a 2π phase dispersion, a velocity dependent common phase was added to all isochromats in a voxel at the end of each repetition. This simulation experiment was conducted with velocity values ranging from -1mm/s to 1mm/s, with a 2mm voxel dimension. Other parameters used in the simulation included: flip angle = 18°, TR = 5ms, $\Delta\Phi=\pm2°$, T_2=50ms, and T_1=1000ms. Signal phase attributed to T_2 was estimated from the phase difference between the two signals (i.e. with $\Delta\Phi=\pm2°$) divided by 2, and compared with a T_2 lookup table for T_2 estimation, using the proposed method described in the Theory section. The lookup table was generated using Bloch equation simulation without motion and the same acquisition parameters over a wide range of tissue relaxation parameters.

6.5 Results

Phantom experiments:

In the phantom experiment the T_1 of the phantom vials were estimated by FSE-IR to be 873ms, 932ms, 829ms, 925ms corresponding to agar concentrations of 0.5%, 1%, 2%, 4%, respectively, in phantoms with 2mM $NiCl_2$; 1390ms, 1315ms, 1279ms, 1332ms in phantoms with 1mM $NiCl_2$; 1725ms, 1698ms, 2053ms, 1792ms in phantoms with 0.5mM $NiCl_2$; 2848ms, 2902ms, 2788ms, 2888ms in phantoms with 0mM $NiCl_2$. The proposed method (which did not correct for T_1 effect in the signal phase) demonstrated close agreement with reference T_2 estimates (Figure 6.4) (slope=1.03±0.07, intercept=-3.24±5.67). For vials of vastly different T_1 measurements (2mM $NiCl_2$ and 0.5mM $NiCl_2$), the T_2 measurements show slightly higher deviation from the reference at high T_2 values.

In vivo experiments:

In the knee imaging experiments, the proposed method produced high quality T_2 maps in all knees (Figure 6.5), including high apparent SNR and excellent depiction of anatomical detail. In areas where water signal is dominant (cartilage and muscle), similar T_2 values were observed between the proposed method and the multi-echo SE T_2 map used as a reference.

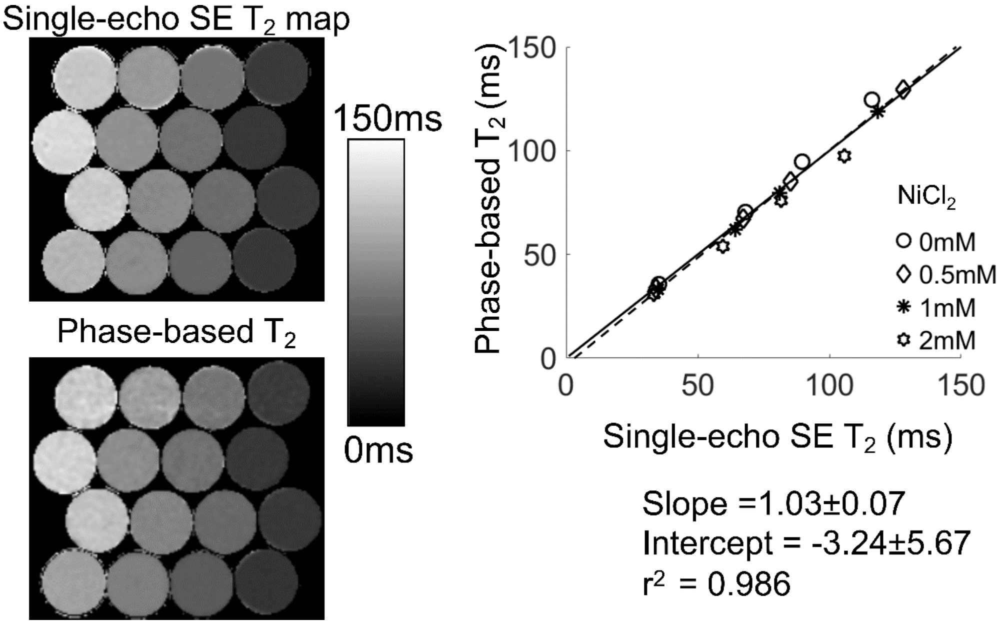

Figure 6.4 T_2 maps generated using the proposed method provided accurate T_2 measurements agreeing closely with spin-echo T_2 mapping. Phantom T_2 maps generated using single-echo SE MRI and the center slice of the phase-based T_2 mapping are shown. The agreement between the phase-based T_2 map and single-echo SE MRI was evidenced by linear regression between T_2 values averaged in ROIs drawn in the center of the vials, with a slope and intercept statistically equal to one and zero, respectively.

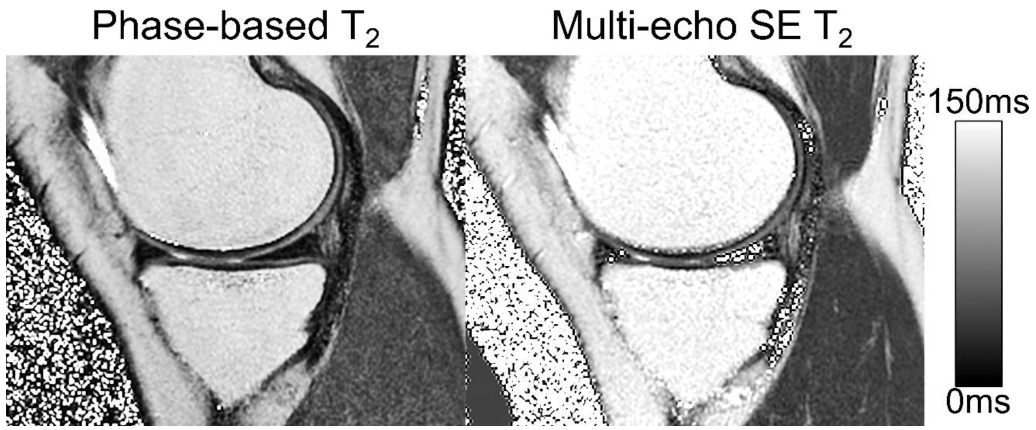

Figure 6.5 T_2 map generated with the phase-based T_2 mapping showed excellent image quality in all six knees. Similar intensities can be observed in regions with dominant water signal such as cartilage and the muscle. An example of T_2 maps generated using multi-echo SE MRI and the proposed method are shown.

In Figure 6.6, the box-whisker plot and scatter plot showed strong correlation between the phase-based T_2 and the reference T_2 measurements (Pearson correlation coefficient = 0.86), with slope=0.78±0.12 and intercept=3.24±4.84. Quantitative T_2 values measured using the proposed method were very similar to the multi-echo SE based T_2 measurements, although many of these measurements showed statistical differences.

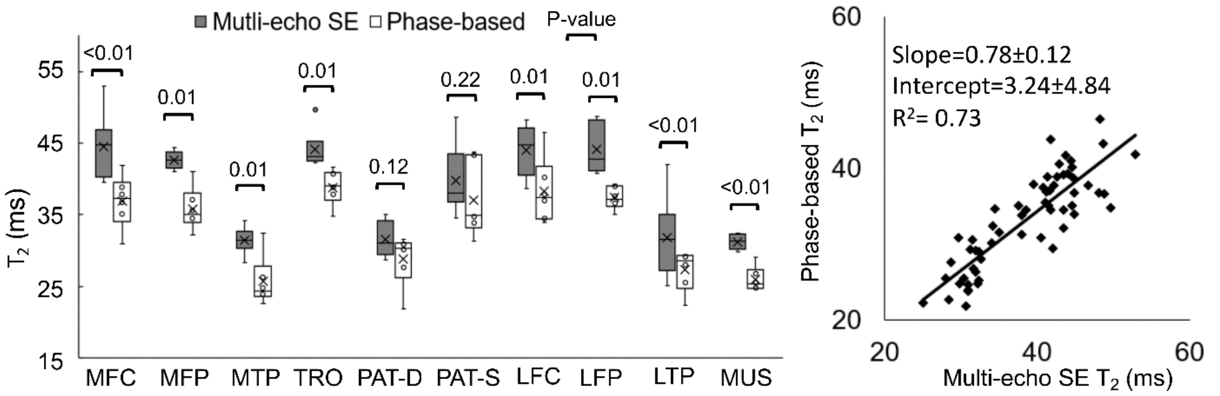

Figure 6.6 The box and whisker plot and scatter plot showed strong correlation between the phase-based T_2 and the multi-echo SE T_2 with a high Pearson correlation coefficient (0.86). Measurements made in 10 different regions on each of six different knees. The regions measured

were medial femoral central condyle (MFC), medial femoral posterior condyle (MFP), medial tibial plateau (MTP), patella-deep (PAT-D), patella-superficial (PAT-S), lateral femoral central condyle (LFC), lateral femoral posterior (LFP), lateral tibial plateau (LTP), gastrocnemius muscle (MUS).

Similarly, high quality T_2 maps were generated by the proposed method in the brain (Figure 5.7). However, some discrepancies in T_2 values were observed between the two methods, especially in the grey matter. Average T_2 values in regions of interest (ROIs) were 39ms (phase-based) and 53ms (SE) in the genu of corpus callosum; 40ms (phase-based) and 61ms (SE) in the splenium of corpus callosum; 47ms (phase-based) and 59ms (SE) in the white matter; 35ms (phase-based) and 40ms (SE) in the globus pallidus of basal ganglia; 45ms (phase-based) and 54ms(SE) in the putamen of basal ganglia.

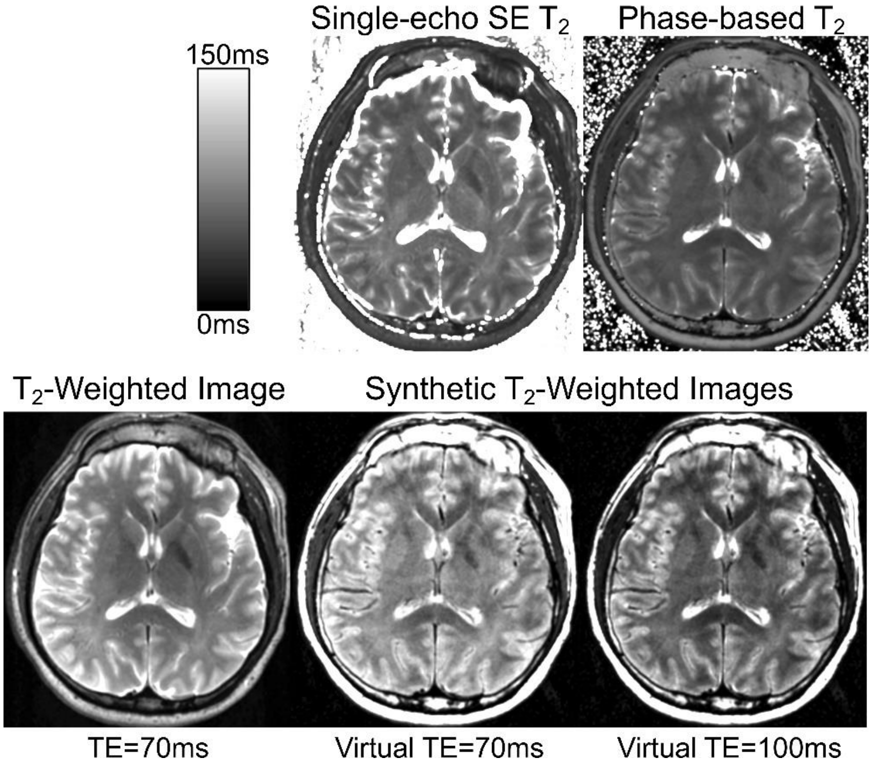

Figure 6.7 High quality T_2 maps were generated in the brain using the proposed phase-based method. The phase-based T_2 appeared lower than the reference T_2 map especially in the grey matter. The magnitude image used in the proposed method is also shown. Synthesized T_2-weighted images (virtual TE=70ms, TE=100ms) showed overall similar appearance although with less grey-white matter contrast than T_2-weighted SE at the same TE (70ms).

Synthetic T_2-weighted images generated from the phase-based T_2 map and the simultaneously acquired magnitude images are also shown with two different virtual echo times (70ms, 100ms). Compared with a T_2-weighted SE image with TE of 70ms, the synthesized T_2-weighted image with virtual TE of 70ms showed overall similar appearance, although with slightly reduced apparent gray-white matter contrast..

In the abdomen and pelvis, 3D spatially resolved T_2 maps generated from separated water signal were successfully reconstructed after water-fat separation (Figure 6.8). Close agreement between T_2 value of the water signal estimated by the proposed method and MRS was observed, with estimates of 20ms and 22ms respectively, using a co-localized voxel. Similarly, in the spleen, the proposed method measured a T_2 value of 38ms compared to 34ms with MRS.

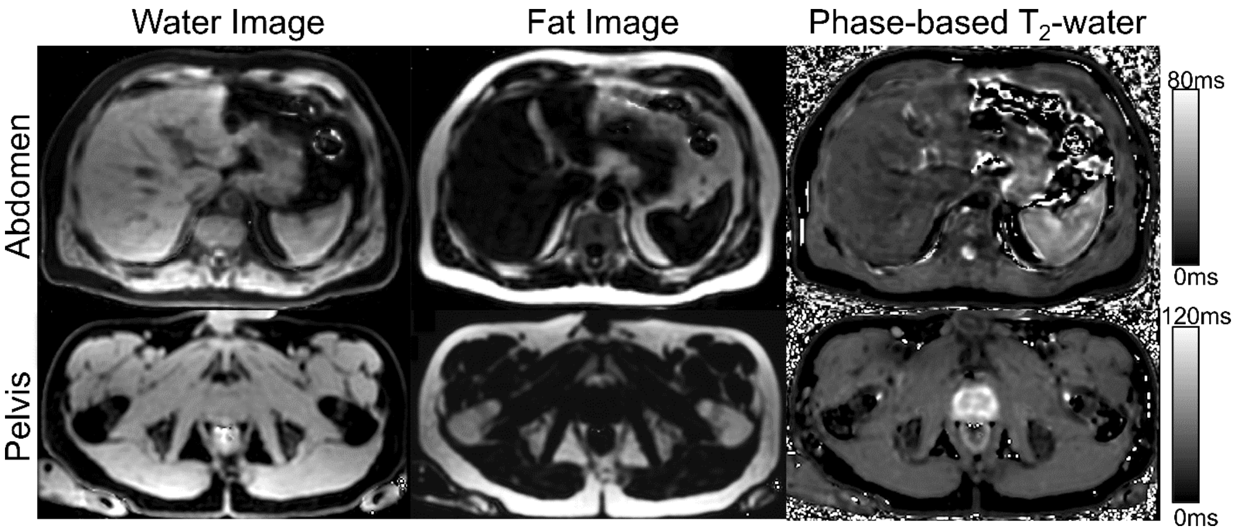

Figure 6.8 The proposed phase-based 3D T_2 mapping combined with CSE-MRI water-fat separation is feasible over the entire abdomen or the pelvis within a single breath-hold. Water and fat images were calculated from multi-echo gradient echo images with varied RF phase increments. A phase-based T_2 map for water signal was also generated from the water phase of different RF phase increments. Simultaneous R_2^* and B_0 field maps were also generated, but not included for brevity.

Finally, in the peripheral zone of the prostate, phase-based T_2 measurements (72ms) were comparable to values reported in literature (74±9ms in the prostate)[131].

Simulation experiment to study the sensitivity of signal phase to motion:

As shown in Figure 9, the signal phase in the proposed method was sensitive to motion. For example, a velocity of 1mm/s lead to a 3.6° change in the signal phase, relative to no motion. Accordingly, the apparent T_2 estimation was reduced from 50ms to 42ms.

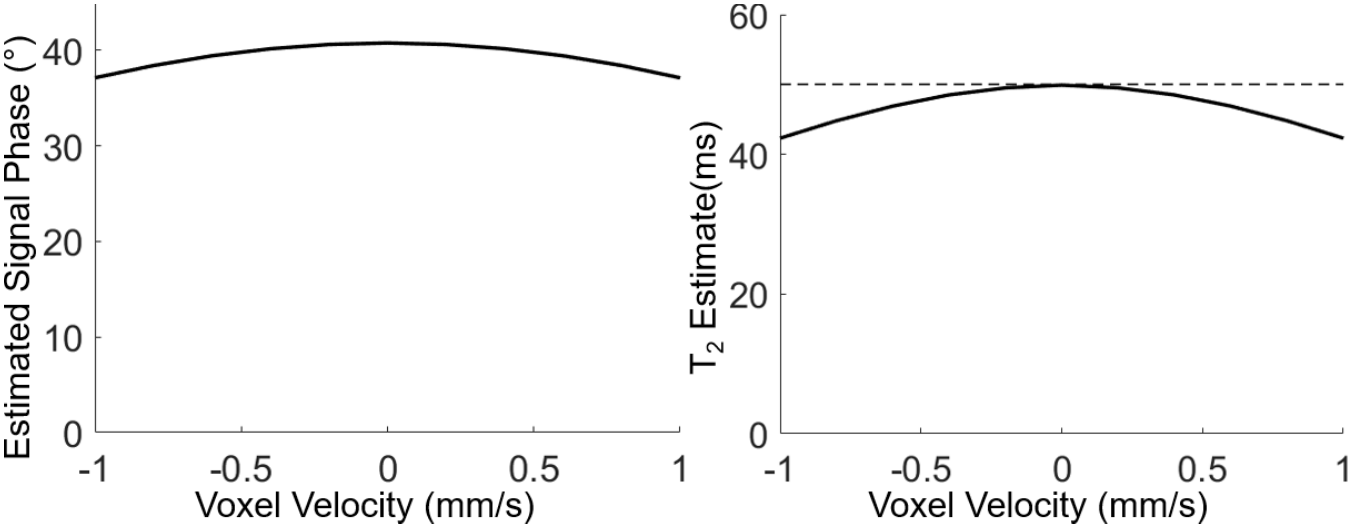

Figure 6.9 Sensitivity of the proposed method to motion. Signal phase generated using Bloch-equation simulation modeling constant velocity leads to small errors in the apparent T_2-dependent phase and subsequent underestimation of T_2.

6.6 Discussion

We have proposed and successfully demonstrated preliminary feasibility of a phase-based T_2 mapping technique based on GRE imaging. The theory and technique for encoding T_2 information into the signal phase of a gradient echo acquisition were developed. We demonstrated that using a small RF phase increment in gradient echo acquisitions, a signal phase that increases monotonically with the transverse relaxation time can be generated. This behavior forms the basis of the proposed method for encoding information into the GRE signal phase. The feasibility of the proposed method was successfully demonstrated in phantoms and in vivo experiments, including in combination with chemical shift encoded water-fat separation. Further, the proposed approach can be used to generate high quality synthetic T_2 weighted images that can be acquired in relatively short acquisition times.

Compared with traditional SE-based T_2 mapping and T_2-prep-based methods, the proposed method reduces acquisition time and would potentially render quantitative T_2 mapping feasible for many clinical applications, including those that require short breath-holds. Compared with DESPOT2, the proposed method requires fewer GRE source images for parametric mapping and consequently shorter acquisition time. Further, the proposed method is also immune to signal voids caused by banding artifacts seen with bSSFP methods. Compared with the TESS T_2 mapping technique, T_2-weighting and T_2*-weighting in the signals of the proposed method are naturally separated, because the T_2 information is contained in the signal phase, which is not affected by T_2* effects. Compared with the TESS T_2 mapping technique, T_2 weighting and T_2* weighting in the signals of the proposed method are naturally separated. The proposed technique is also compatible with CSE-MRI, which is useful in many extra-cranial imaging applications, particularly in the abdomen and pelvis. This feature would enable simultaneous generation of T_2 maps for both water and fat signals as well as the R_2* and B_0 field map.

In this work, the proposed GRE-based method was able to shorten the minimum acquisition time compared to spin-echo-based T_2-mapping methods. Among the steady-state methods, DESPOT2 requires at least three of more acquisitions. The proposed phase-based T_2 mapping technique requires two acquisitions, while DESS and TESS require only one. The number of acquisitions required would normally determine the minimum acquisition time needed to create a T_2 map of a certain resolution and FOV. However, it is worth noting that the relative advantage of DESS and TESS in this comparison is offset by their generally longer TR (14ms, 20ms, 26ms, 21ms) [113,114,206,207] compared to DESPOT2 (e.g. 3.6ms) [112] and the phase-based T_2 mapping (e.g. 5.9ms, 5.6ms and 6.5ms in this work). Further, depending on the application, multiple signal averages are often acquired, when there is sufficient acquisition time (e.g. in the knee and in the brain). In such applications, the SNR efficiency is a more important measure of acquisition speed. Rigorous evaluation of the SNR performance of the proposed method is beyond the scope of this work but will be an important component of future investigations.

Small discrepancies between the T_2 measured with the proposed method and SE-based methods was observed, particularly in the brain. While the reasons for these discrepancies are unclear, possible reasons include multi-component T_2 effects, magnetization transfer, B_1 inhomogeneities, motion, or combinations of these factors. Further work will be needed to determine the cause of these discrepancies.

Previous studies have demonstrated that motion can lead to change in the signal magnitude in steady-state acquisitions using unbalanced gradient echo acquisitions and pseudo-random RF phase spoiling. In this work, we have performed preliminary Bloch equation simulations modeling constant linear motion, demonstrating that small changes in the signal phase may result from motion, leading to underestimation of T_2. Although no definite effects of motion on artifacts or T_2 estimation accuracy were observed in the experimental studies, some underestimation of T_2, relative to references standard measurements was observed in cartilage and in the brain. It is uncertain whether this apparent underestimation in T_2 was related to motion or not. Future rigorous evaluation of the potential effects of motion on T_2 estimation is warranted, especially for applications where tissue motion may be an important factor, eg. heart, flowing blood.

There are several limitations of this work. First, although the feasibility of this method has been successfully demonstrated, considerable technical optimization and substantial further clinical validation is needed. Further studies will be needed to evaluate the technical accuracy and noise performance of the proposed method, as well as to optimize acquisition parameters. In addition, the precise impact of B_1 inhomogeneities, variation in T_1 of the tissues, magnetization transfer effects[216] and multi-exponential relaxation[211] requires further evaluation. These effects may explain the apparent discrepancies between the T_2 measurements in the brain between the proposed phase-based method and conventional SE-based T_2 mapping.

Another major limitation of the proposed method is that the T_2 mapping algorithm requires knowledge or assumption of the T_1 of tissue to map the signal phase into a T_2 value. Although the signal phase is relatively independent of T_1 for long T_1 values, this is not the case for shorter T_1 values. Thus, the overall accuracy of this method is unknown for T_2 quantification, especially in tissues with short T_1 values.

Further, the proposed method can be used to generate synthetic T_2-weighted images. However, due to the relatively large flip angle in the proposed method, the source magnitude images are T_1-weighted. For this reason, the T_2-weighted images synthesized from the phased-based T_2 maps and simultaneously acquired magnitude images will be T_1-weighted as well, similar to short tau inversion recovery (STIR) based methods.

In addition, the proposed method currently requires the use of 3D acquisitions, due to the need for a uniform flip angle across the tissue of interest. Extension to 2D imaging should be feasible but will require more complex lookup table construction that accounts for acquisition slice profiles.

In conclusion, we have presented and successfully demonstrated the feasibility of a novel phase-based T_2 mapping method based on gradient echo imaging. This approach has the potential for rapid, 3D mapping of T_2 in tissue. Further technical development, optimization and clinical validation are needed.

6.7 Acknowledgement

The authors wish to thank David Harris, PhD for his assistance with preparing and reviewing this manuscript. We acknowledge the use of the ISMRM Fat-Water Toolbox (http://ismrm.org/workshops/FatWater12/data.htm) for some of the reconstruction methods described in this article. The authors also wish to acknowledge support from the NIH (R01 DK100651, R01 DK088925, R01 DK117354, K24 DK102595, and R41 EB025729).

Chapter 7 : Summary and Future Works

7.1 Summary

In this work, together with members of the Liver Imaging Research Program, I have made several contributions to the improvement and development of MRI based non-invasive imaging biomarkers for the assessment of non-alcoholic fatty liver disease (NAFLD) and liver fibrosis.

The comparison between pre-calibrated fat spectral models in computer simulations and in vivo confirmed the necessity of using a multi-peak spectral model of fat in chemical shift encoded (CSE)-MRI. The close similarity in performance in fat quantification using most of the multi-peak models and even the slight outlying performance by 7-peak model provided insight to guide the standardization of CSE-MRI based fat quantification for the assessment of NAFLD.

The computer simulation in chapter 4 along with emerging studies evidencing the wide variation of indigenous parenchymal T_1 suggest a need for a T1-corrected CSE-MRI fat quantification technique. A T_1-corrected variable flip angle (VFA)-CSE-MRI fat quantification was developed and rigorously evaluated using computer simulations, phantom and in vivo experiments. Although a potential bias was suspected in this proposed technique in cases of low proton density fat fraction (PDFF), this technique has the potential to accurately assess NAFLD in cases of non-typical parenchymal T_1.

A diffusion phantom that provides reproducible unrestricted Gaussian diffusion with tunable apparent diffusion coefficient (ADC) values spanning the entire physiological ADC range was developed and validated. This phantom has the potential to fulfill the need of a controlled environment for the development of quantitative diffusion MRI corrected for potential confounding factors. Such diffusion MRI techniques may further improve the accuracy of the staging of fibrosis.

Finally, a novel phase-based T_2 mapping technique feasible for mapping the entire liver in a single breath-hold compatible with simultaneous CSE-MRI was developed. The T_2 measured of only water signal (corrected for the effect of steatosis) in conjunction with the iron concentration derived from R2* may help advance T_2 as an imaging biomarker for the staging of liver fibrosis in particular, and tissue characterization in general.

7.2 Future Works

Improving the Accuracy of T_1-corrected VFA-CSE-MRI Fat Quantification

In chapter 4 of this dissertation, despite the accurate fat quantification by the proposed T_1-corrected VFA-CSE-MRI, a small bias was identified with the in vivo PDFF measurements. This may have resulted from the erratic T_{1F} estimate when the fat signal is below noise level, or from a mechanism similar to the noise related bias in low flip angle (LFA)-CSE-MRI as the assumption of common phase between water and fat is no longer valid. A dedicated phantom study or simulation experiment with varying imposed constraint on the T_{1F} estimates and varying level of SNR may provide meaningful insight into the source of this bias. A patient study with a larger sample size would also be needed to confirm the phantom and simulation results and give way to a more accurate VFA-CSE-MRI technique with improved reconstruction.

Liver T_1-mapping

T_1 estimates of individual chemical species are the useful byproducts produced by the T_1-corrected fat quantification technique developed in chapter 4. Although these T_1 values are produced with a signal model assuming known flip angles, i.e., uncorrected for B_1 inhomogeneity, outlying T_{1W} (parenchymal T_1) values were found in patients with confirmed non-alcoholic steatohepatitis (NASH) and cholangiocarcinoma. It is possible that T_{1W} measured using this technique at 1.5T has diagnostic value even without B_1 inhomogeneity correction. If this approach is feasible, high SNR may be preserved in the T_1 estimate by avoiding additional degrees of freedom in the signal model.

To investigate the feasibility of detection of hepatic inflammation and abnormal uptake of liver specific contrast agents using the T_{1W} estimated by the proposed T_1-corrected fat quantification technique at 1.5T, the accuracy of T_1 estimates need to be evaluated in the phantom. The same doped agar-peanut oil phantom described in chapter 4 can be used. A reference T_{1W} can be obtained by applying B_1-correction based on a separate Bloch-Siegert shift acquisition[217]. A more reliable reference can be obtained using Inversion recovered fast spin echo (FSE) T_1 mapping for agar phantom without fat.

Due to the lack of gold standard of liver parenchymal T_1 measurement, the effect of B_1 inhomogeneity in vivo can only be evaluated indirectly by measuring the spatial and inter-subject variation of transmit B_1. This information can be then used to evaluate the bias caused by B_1 inhomogeneity a computer simulation.

At higher field strengths (e.g. 3T or more), due to the shorter wave length of RF excitation pulse, transmit B_1 amplitude is generally more spatially inhomogeneous. B_1-correction is likely necessary for these applications. A combination of CSE-MRI with the variable flip angle-actual flip[218] (VAFI) angle imaging may provide the B_1-corrected T_{1W} mapping. A separate B_1 calibration scan with motion registration is another potential solution to the problem.

Acetone-H_2O Phantom

The acetone-D_2O phantom developed in chapter 5 has a limited shelf-life. Although cold-storage can extend the shelf-life, a phantom unaffected by the molecular exchange of hydrogen between D_2O and acetone will be advantageous. Some preliminary results[219] presented at the 24th annual meeting of the international society for the magnetic resonance in medicine showed the feasibility of replacing acetone-D_2O mixture with an acetone-H_2O mixture doped with manganese chloride. More rigorous evaluation of this acetone-H_2O phantom may validate it for its application in the development of quantitative diffusion MRI. Further, restricted diffusion may be introduced into this phantom using 3D-printed polyethylene structure.

T_2-based Staging of Liver Fibrosis

The potential of T_2-based staging of liver fibrosis has only been shown in mouse models so far. A clinical study where the T_2 and histological analysis of liver fibrosis are compared, similar to those performed comparing intravoxel incoherent motion (IVIM), magnetic resonance elastography (MRE) and liver biopsy, has yet to be conducted. In the design of this study, the phase-based T_2 mapping technique, multi-echo spin-echo T_2 mapping, and liver biopsy can be performed in parallel with canonical CSE-MRI to provide a reference for steatosis and iron concentration. In addition to the association between T_2 and the severity of fibrosis, the confounding effect of steatosis and iron can be at the same statistically analyzed.

Quantification of Liver Iron Concentration

The reciprocal of T_2 (R_2) was a widely accepted MRI biomarker for liver iron overload before the emergence of R_2*[23]. The main limitation of using R_2 is the lengthy exam time required by multi-echo spine-echo (SE) acquisitions[23]. The phase-based T_2 mapping technique developed in chapter 6 has overcome this difficulty and could be used for the spatially resolved quantification of liver iron concentration over the entire liver. Prospective clinical studies are required to calibrate the measured R_2 compared with iron concentration measured with a reliable reference.

Importantly, in addition to R_2 and R_2* as mentioned in chapter 6, this phase-based T_2 mapping technique due to its compatibility with CSE-MRI, is capable of producing simultaneous B_0 field-map, which can be used to estimate a spatially resolved quantitative susceptibility map (QSM). This feature is likely to enable a simultaneous voxel by voxel quantification of three different iron related parameters, i.e.: R_2, R_2* and susceptibility.

As a result of the different mechanisms of relaxation, R2 and R_2* have shown differential sensitivity to the quantities of hemosiderin and ferritin as two different proteins used to store excessive iron, which are the most common forms of iron deposition in the liver[24]. QSM is, in theory, a measure of all iron including that found in hemosiderin, ferritin, transferrin (another protein used for the transferring of iron), and labile iron. The simultaneous quantification of all three parameters is likely to give a more complete characterization the iron tissue content. Further technical development is required to develop confounder corrected and accurate technique used for R_2, R_2* and susceptibility quantification. Comparisons between the these simultaneously obtained parameters and histology is required to calibrate more specific assessments of different forms of iron deposition.

List of Publications and Conference Abstracts

Published Manuscripts

1. **Wang X**, Hernando D, Reeder SB. Sensitivity of chemical shift-encoded fat quantification to calibration of fat MR spectrum. Magnetic Resonance in Medicine. 75(2);845-851;2016.
2. **Wang X**, Reeder SB, Hernando D. An acetone-based phantom for quantitative diffusion MRI. Journal of Magnetic Resonance Imaging. 46(6);1683-1692;2017.
3. Knobloch G, Colgan T, Wiens CN, **Wang X**, Schubert T, Hernando D, Sharma S, Reeder SB. Relaxivity of Ferumoxytol at 1.5 T and 3.0 T. Investigative Radiology. 53(5);257-263;2018.
4. Peña-Nogales Ó, Zhang Y, **Wang X**, De Luis-Garcia R. Optimized Diffusion-Weighting Gradient Waveform Design (ODGD) formulation for motion compensation and concomitant gradient nulling. Magnetic Resonance in Medicine. 81(2);989-1003;2019.

Manuscript under Revision

1. Knobloch G, Colgan TJ, **Wang X**, Woo KM, Schubert T, Reeder S. Combined Gadoxetic Acid and Gadobenate Dimeglumine Enhanced Liver MRI: A Parameter Optimization Study. Abdominal Radiology. 2019.

2. **Wang X**, Colgan TJ, Hinshaw LA, Roberts NT, Henze Bancroft LC, Hamilton G, Hernando D, Reeder SB. T1-Corrected Quantitative Chemical Shift Encoded Magnetic Resonance Imaging. Magnetic Resonance in Medicine. 2019.

3. **Wang X**, Hernando D, Reeder SB. Phase-based T2 Mapping with Gradient Echo Imaging. Magnetic Resonance in Medicine. 2019.

Conference Abstracts

1. **Wang X**, Bancroft LH, Kecskemeti S, Reeder S, Block W. Prediction and Removal of Aliased Signal in Undersampled IDEAL: Simulation Using a Digital Breast Phantom. In: Fat-Water Separation: Insights, Applications & Progress in MRI. Long Beach, CA, USA; 2012. (abstract 32).
2. **Wang X**, Hernando D, Reeder SB. Evaluation of Sensitivity of Fat Fraction Measurement to Fat Spectral Model Precalibration In: Proceedings of the 23rd Annual Meeting of ISMRM. Milan, Italy; 2014. (abstract 3598).
3. **Wang X**, Reeder S, Hernando D. A novel phantom for quantitative diffusion MRI based on acetone and deuterium oxide. In: Proceedings of the 24th Annual Meeting of ISMRM. Toronto, Ontario, Canada; 2015. (abstract 0159).**(Oral Presentation)**
4. **Wang X**, Hernando D, Reeder SB. T1 Corrected Fat Quantification Using a Dual Flip Angle Acquisition and Joint Fit Reconstruction. In: Proceedings of the 24th Annual Meeting of ISMRM. Toronto, Ontario, Canada; 2015. (abstract 3661).
5. **Wang X**, Reeder SB, Hernando D. Single MR spectral peak diffusion phantom with wide ADC range based on acetone, H2O and manganese chloride. In: Proceedings of the 25th Annual Meeting of ISMRM. Singapore, Singapore; 2016. (abstract 0921). **(Oral Presentation)**
6. **Wang X**, Sharma S, Bashir MR, et al. Multi-Center Validation of an Acetone-D2O Quantitative Diffusion Phantom. In: Proceedings of the 25th Annual Meeting of ISMRM. Singapore, Singapore; 2016. (abstract 3485).
7. **Wang X**, Wiens CN, Reeder SB. Fast T1 Correction for Fat Quantification using a Dual-TR Chemical Shift Encoded MRI Acquisition. In: Proceedings of the 26th Annual Meeting of ISMRM. Honolulu, HI, USA; 2017. (abstract 3961).
8. Bancroft LH, Hernando D, **Wang X**, Reeder SB, Strigel RM. Quantifying Fibroglandular Tissue Volume using Chemical-Shift Encoded MRI: Validation in a Phantom. In: Proceedings of the 26th Annual Meeting of ISMRM. Honolulu, HI, USA; 2017. (abstract 2112).

9. Roberts N, Colgan T, **Wang X**, Hernando D, Reeder B. B1- and Fat-Corrected T1 Mapping Using Chemical-Shift Encoded MRI. In: Proceedings of the 27th Annual Meeting of ISMRM. Paris, France; 2018. (abstract 4243).
10. Knobloch G, Colgan T, **Wang X**, Tilman S, Hernando D, Reeder SB. Combined Gadoxetic Acid and Gadobenate Dimeglumine Enhanced Liver MRI for Liver Metastasis Detection: A Parameter Optimization Study. In: Proceedings of the 27th Annual Meeting of ISMRM. Paris, France; 2018. (abstract 0075).
11. **Wang X**, Hernando D, Reeder SB. In vivo feasibility of T1-corrected Dual-TR Chemical Shift Encoded Fat Quantification Method. In: Proceedings of the 27th Annual Meeting of ISMRM. Paris, France; 2018. (abstract 2775).
12. Knobloch G, Colgan T, Wiens CN, **Wang X**, Tilman S, Hernando D, Reeder SB. Relaxivity of Ferumoxytol at 1.5T and 3.0T. In: Proceedings of the 27th Annual Meeting of ISMRM. Paris, France; 2018. (abstract 5029).
13. Zhang Y, **Wang X**, Taviani V, Hernando D. STimulated Echo based Mapping (STEM) of T1, T2 and Apparent Diffusion Coefficient. In: Proceedings of the 27th Annual Meeting of ISMRM. Paris, France; 2018. (abstract 5638).
14. **Wang X**, Hernando D, Reeder SB. A Novel Phase Based T2 Mapping Technique Using Gradient Echo Imaging. In: Proceedings of the 28th Annual Meeting of ISMRM. Montréal, QC, Canada; 2019. (abstract 0942). **(Oral Presentation)**
15. Zhao R, Zhang Y, **Wang X**, Kevin J, Reeder SB, Hernando D. Motion-Robust, High-SNR Fat Quantification using a Variable Flip Angle Approach. In: Proceedings of the 28th Annual Meeting of ISMRM. Montréal, QC, Canada; 2019. (abstract 1155).
16. Roberts N, Hernando D, Colgan T, **Wang X**, Reeder SB. Simultaneous B1- and Fat-Corrected T1 Mapping Using Chemical-Shift Encoded MRI. In: Proceedings of the 28th Annual Meeting of ISMRM. Montréal, QC, Canada; 2019. (abstract 4673).

Bibliography

1. Angulo P. Nonalcoholic Fatty Liver Disease. *New England Journal of Medicine*. 2002;346(16):1221-1231. doi:10.1056/NEJMra011775
2. Szczepaniak LS, Nurenberg P, Leonard D, et al. Magnetic resonance spectroscopy to measure hepatic triglyceride content: prevalence of hepatic steatosis in the general population. *American Journal of Physiology-Endocrinology and Metabolism*. 2005;288(2):E462-E468. doi:10.1152/ajpendo.00064.2004
3. Ford ES. Risks for All-Cause Mortality, Cardiovascular Disease, and Diabetes Associated With the Metabolic Syndrome: A summary of the evidence. *Diabetes Care*. 2005;28(7):1769-1778. doi:10.2337/diacare.28.7.1769
4. Marchesini G, Brizi M, Bianchi G, et al. Nonalcoholic Fatty Liver Disease: A Feature of the Metabolic Syndrome. *Diabetes*. 2001;50(8):1844-1850. doi:10.2337/diabetes.50.8.1844
5. Falchuk KR, Fiske SC, Haggitt RC, Federman M, Trey C. Pericentral hepatic fibrosis and intracellular hyalin in diabetes mellitus. *Gastroenterology*. 1980;78(3):535-541. doi:10.1016/0016-5085(80)90869-0
6. Sheth SG. Nonalcoholic Steatohepatitis. *Ann Intern Med*. 1997;126(2):137. doi:10.7326/0003-4819-126-2-199701150-00008
7. Cotrim HP, Oliveira CP, Coelho HSM, et al. Nonalcoholic steatohepatitis and hepatocellular carcinoma: Brazilian survey. *Clinics (Sao Paulo)*. 2016;71(5):281-284. doi:10.6061/clinics/2016(05)07
8. Albano E, Mottaran E, Occhino G, Reale E, Vidali M. Review article: role of oxidative stress in the progression of non-alcoholic steatosis. *Alimentary Pharmacology & Therapeutics*. 2005;22(s2):71-73. doi:10.1111/j.1365-2036.2005.02601.x
9. Romero-Gómez M, Zelber-Sagi S, Trenell M. Treatment of NAFLD with diet, physical activity and exercise. *Journal of Hepatology*. 2017;67(4):829-846. doi:10.1016/j.jhep.2017.05.016
10. Vilar-Gomez E, Martinez-Perez Y, Calzadilla-Bertot L, et al. Weight Loss Through Lifestyle Modification Significantly Reduces Features of Nonalcoholic Steatohepatitis. *Gastroenterology*. 2015;149(2):367-378.e5. doi:10.1053/j.gastro.2015.04.005
11. Marchesini G, Brizi M, Morselli-Labate AM, et al. Association of nonalcoholic fatty liver disease with insulin resistance. *The American Journal of Medicine*. 1999;107(5):450-455. doi:10.1016/S0002-9343(99)00271-5
12. Marchesini G, Bianchi G, Tomassetti S, Zoli M, Melchionda N. Metformin in non-alcoholic steatohepatitis. *The Lancet*. 2001;358(9285):893-894. doi:10.1016/S0140-6736(01)06042-1
13. Caldwell SH, Hespenheide EE, Redick JA, Iezzoni JC, Battle EH, Sheppard BL. A pilot study of a thiazolidinedione, troglitazone, in nonalcoholic steatohepatitis. *The American journal of gastroenterology*. 2001;96(2):519.
14. Bugianesi E, Marzocchi R, Villanova N, Marchesini G. Non-alcoholic fatty liver disease/non-alcoholic steatohepatitis (NAFLD/NASH): treatment. *Best Practice & Research Clinical Gastroenterology*. 2004;18(6):1105-1116. doi:10.1016/j.bpg.2004.06.025
15. Schaffner F, Klion FM. Chronic hepatitis. *Annual review of medicine*. 1968;19(1):25–38.

16. Bataller R, Brenner DA. Liver fibrosis. *J Clin Invest*. 2005;115(2):209-218. doi:10.1172/JCI24282
17. Poynard T, Lebray P, Ingiliz P, et al. Prevalence of liver fibrosis and risk factors in a general population using non-invasive biomarkers (FibroTest). *BMC Gastroenterology*. 2010;10(1):40. doi:10.1186/1471-230X-10-40
18. Scaglione S, Kliethermes S, Cao G, et al. The Epidemiology of Cirrhosis in the United States. doi:info:doi/10.1097/MCG.0000000000000208
19. Arthur MJP. Reversibility of liver fibrosis and cirrhosis following treatment for hepatitis C. *Gastroenterology*. 2002;122(5):1525-1528. doi:10.1053/gast.2002.33367
20. Parés A, Caballería J, Bruguera M, Torres M, Rodés J. Histological course of alcoholic hepatitis: Influence of abstinence, sex and extent of hepatic damage. *Journal of Hepatology*. 1986;2(1):33-42. doi:10.1016/S0168-8278(86)80006-X
21. Poynard T, McHutchison J, Manns M, et al. Impact of pegylated interferon alfa-2b and ribavirin on liver fibrosis in patients with chronic hepatitis C. *Gastroenterology*. 2002;122(5):1303-1313. doi:10.1053/gast.2002.33023
22. Dixon JB, Bhathal PS, Hughes NR, O’Brien PE. Nonalcoholic fatty liver disease: Improvement in liver histological analysis with weight loss. *Hepatology*. 2004;39(6):1647-1654. doi:10.1002/hep.20251
23. Hernando D, Levin YS, Sirlin CB, Reeder SB. Quantification of liver iron with MRI: State of the art and remaining challenges. *Journal of Magnetic Resonance Imaging*. 2014;40(5):1003-1021. doi:10.1002/jmri.24584
24. Wood JC. Impact of Iron Assessment by MRI. *Hematology*. 2011;2011(1):443-450. doi:10.1182/asheducation-2011.1.443
25. Kleiner DE, Brunt EM, Natta MV, et al. Design and validation of a histological scoring system for nonalcoholic fatty liver disease. *Hepatology*. 2005;41(6):1313-1321. doi:10.1002/hep.20701
26. Brunt EM, Janney CG, Di Bisceglie AM, Neuschwander-Tetri BA, Bacon BR. Nonalcoholic steatohepatitis: a proposal for grading and staging the histological lesions. *The American journal of gastroenterology*. 1999;94(9):2467.
27. Reeder SB, Sirlin CB. Quantification of Liver Fat with Magnetic Resonance Imaging. *Magnetic Resonance Imaging Clinics*. 2010;18(3):337-357. doi:10.1016/j.mric.2010.08.013
28. Saadeh S, Younossi ZM, Remer EM, et al. The utility of radiological imaging in nonalcoholic fatty liver disease. *Gastroenterology*. 2002;123(3):745-750. doi:10.1053/gast.2002.35354
29. Graif M, Yanuka M, Baraz M, et al. Quantitative estimation of attenuation in ultrasound video images: correlation with histology in diffuse liver disease. *Invest Radiol*. 2000;35(5):319-324.
30. Limanond P, Raman SS, Lassman C, et al. Macrovesicular Hepatic Steatosis in Living Related Liver Donors: Correlation between CT and Histologic Findings. *Radiology*. 2004;230(1):276-280. doi:10.1148/radiol.2301021176
31. Hines CDG, Frydrychowicz A, Hamilton G, et al. T1 independent, T2* corrected chemical shift based fat–water separation with multi-peak fat spectral modeling is an accurate and precise measure of hepatic steatosis. *Journal of Magnetic Resonance Imaging*. 2011;33(4):873-881. doi:10.1002/jmri.22514
32. Yokoo T, Bydder M, Hamilton G, et al. Nonalcoholic Fatty Liver Disease: Diagnostic and Fat-Grading Accuracy of Low-Flip-Angle Multiecho Gradient-Recalled-Echo MR Imaging at 1.5 T. *Radiology*. 2009;251(1):67-76. doi:10.1148/radiol.2511080666

33. Meisamy S, Hines CDG, Hamilton G, et al. Quantification of Hepatic Steatosis with T1-independent, T2*-corrected MR Imaging with Spectral Modeling of Fat: Blinded Comparison with MR Spectroscopy. *Radiology*. 2011;258(3):767-775. doi:10.1148/radiol.10100708
34. Yokoo T, Shiehmorteza M, Hamilton G, et al. Estimation of Hepatic Proton-Density Fat Fraction by Using MR Imaging at 3.0 T. *Radiology*. 2011;258(3):749-759. doi:10.1148/radiol.10100659
35. Zhong X, Nickel MD, Kannengiesser SAR, Dale BM, Kiefer B, Bashir MR. Liver fat quantification using a multi-step adaptive fitting approach with multi-echo GRE imaging. *Magnetic Resonance in Medicine*. 2014;72(5):1353-1365. doi:10.1002/mrm.25054
36. Kühn J-P, Hernando D, Muñoz del Rio A, et al. Effect of Multipeak Spectral Modeling of Fat for Liver Iron and Fat Quantification: Correlation of Biopsy with MR Imaging Results. *Radiology*. 2012;265(1):133-142. doi:10.1148/radiol.12112520
37. Rockey DC, Caldwell SH, Goodman ZD, Nelson RC, Smith AD. Liver biopsy. *Hepatology*. 2009;49(3):1017-1044. doi:10.1002/hep.22742
38. Thampanitchawong P, Piratvisuth T. Liver biopsy: complications and risk factors. *World J Gastroenterol*. 1999;5(4):301-304. doi:10.3748/wjg.v5.i4.301
39. Fontana RJ, Lok ASF. Noninvasive monitoring of patients with chronic hepatitis C. *Hepatology*. 2002;36(S1):S57-S64. doi:10.1002/hep.1840360708
40. Saverymuttu SH, Joseph AE, Maxwell JD. Ultrasound scanning in the detection of hepatic fibrosis and steatosis. *Br Med J (Clin Res Ed)*. 1986;292(6512):13-15. doi:10.1136/bmj.292.6512.13
41. Singh S, Venkatesh SK, Wang Z, et al. Diagnostic Performance of Magnetic Resonance Elastography in Staging Liver Fibrosis: A Systematic Review and Meta-analysis of Individual Participant Data. *Clinical Gastroenterology and Hepatology*. 2015;13(3):440-451.e6. doi:10.1016/j.cgh.2014.09.046
42. Yin M, Talwalkar JA, Glaser KJ, et al. Assessment of Hepatic Fibrosis With Magnetic Resonance Elastography. *Clinical Gastroenterology and Hepatology*. 2007;5(10):1207-1213.e2. doi:10.1016/j.cgh.2007.06.012
43. Friedrich–Rust M, Ong M, Martens S, et al. Performance of Transient Elastography for the Staging of Liver Fibrosis: A Meta-Analysis. *Gastroenterology*. 2008;134(4):960-974.e8. doi:10.1053/j.gastro.2008.01.034
44. Leitão HS, Doblas S, Garteiser P, et al. Hepatic Fibrosis, Inflammation, and Steatosis: Influence on the MR Viscoelastic and Diffusion Parameters in Patients with Chronic Liver Disease. *Radiology*. 2016;283(1):98-107. doi:10.1148/radiol.2016151570
45. Park HS, Kim YJ, Yu MH, Choe WH, Jung SI, Jeon HJ. Three-Tesla magnetic resonance elastography for hepatic fibrosis: Comparison with diffusion-weighted imaging and gadoxetic acid-enhanced magnetic resonance imaging. *World J Gastroenterol*. 2014;20(46):17558-17567. doi:10.3748/wjg.v20.i46.17558
46. Watanabe H, Kanematsu M, Goshima S, et al. Staging Hepatic Fibrosis: Comparison of Gadoxetate Disodium–enhanced and Diffusion-weighted MR Imaging—Preliminary Observations. *Radiology*. 2011;259(1):142-150. doi:10.1148/radiol.10100621
47. Ding Y, Rao S, Yang L, Chen C, Zeng M. Comparison of the effect of region-of-interest methods using gadoxetic acid-enhanced MR imaging with diffusion-weighted imaging on staging hepatic fibrosis. *Radiol med*. 2016;121(11):821-827. doi:10.1007/s11547-016-0669-7

48. Jiang H, Chen J, Gao R, Huang Z, Wu M, Song B. Liver fibrosis staging with diffusion-weighted imaging: a systematic review and meta-analysis. *Abdom Radiol*. 2017;42(2):490-501. doi:10.1007/s00261-016-0913-6
49. Taouli B, Koh D-M. Diffusion-weighted MR Imaging of the Liver. *Radiology*. 2009;254(1):47-66. doi:10.1148/radiol.09090021
50. Zhang B, Liang L, Dong Y, et al. Intravoxel Incoherent Motion MR Imaging for Staging of Hepatic Fibrosis. *PLOS ONE*. 2016;11(1):e0147789. doi:10.1371/journal.pone.0147789
51. Luetkens JA, Klein S, Träber F, et al. Quantification of Liver Fibrosis at T1 and T2 Mapping with Extracellular Volume Fraction MRI: Preclinical Results. *Radiology*. 2018;288(3):748-754. doi:10.1148/radiol.2018180051
52. Guimaraes AR, Siqueira L, Uppal R, et al. T2 relaxation time is related to liver fibrosis severity. *Quant Imaging Med Surg*. 2016;6(2):103-114. doi:10.21037/qims.2016.03.02
53. Guimaraes AR, Siqueira L, Uppal R, et al. T2 relaxation time is related to liver fibrosis severity. *Quant Imaging Med Surg*. 2016;6(2):103-114. doi:10.21037/qims.2016.03.02
54. Dixon WT. Simple proton spectroscopic imaging. *Radiology*. 1984;153(1):189-194. doi:10.1148/radiology.153.1.6089263
55. Glover GH, Schneider E. Three-point dixon technique for true water/fat decomposition with B0 inhomogeneity correction. *Magnetic Resonance in Medicine*. 1991;18(2):371-383. doi:10.1002/mrm.1910180211
56. Hernando D, Kellman P, Haldar JP, Liang Z-P. Robust water/fat separation in the presence of large field inhomogeneities using a graph cut algorithm. *Magnetic Resonance in Medicine*. 2010;63(1):79-90. doi:10.1002/mrm.22177
57. Reeder SB, Yu H, Johnson JW, et al. T1- and T2-weighted fast spin-echo imaging of the brachial plexus and cervical spine with IDEAL water–fat separation. *Journal of Magnetic Resonance Imaging*. 2006;24(4):825-832. doi:10.1002/jmri.20721
58. Ma J. Breath-hold water and fat imaging using a dual-echo two-point dixon technique with an efficient and robust phase-correction algorithm. *Magnetic Resonance in Medicine*. 2004;52(2):415-419. doi:10.1002/mrm.20146
59. Yu H, Reeder SB, Shimakawa A, Brittain JH, Pelc NJ. Field map estimation with a region growing scheme for iterative 3-point water-fat decomposition. *Magnetic Resonance in Medicine*. 2005;54(4):1032-1039. doi:10.1002/mrm.20654
60. Lu W, Hargreaves BA. Multiresolution field map estimation using golden section search for water-fat separation. *Magnetic Resonance in Medicine*. 2008;60(1):236-244. doi:10.1002/mrm.21544
61. Reeder SB, Hu HH, Sirlin CB. Proton density fat-fraction: A standardized mr-based biomarker of tissue fat concentration. *Journal of Magnetic Resonance Imaging*. 2012;36(5):1011-1014. doi:10.1002/jmri.23741
62. Bydder M, Yokoo T, Hamilton G, et al. Relaxation effects in the quantification of fat using gradient echo imaging. *Magnetic Resonance Imaging*. 2008;26(3):347-359. doi:10.1016/j.mri.2007.08.012
63. Hines CDG, Yu H, Shimakawa A, et al. Quantification of Hepatic Steatosis with 3-T MR Imaging: Validation in ob/ob Mice. *Radiology*. 2009;254(1):119-128. doi:10.1148/radiol.09090131
64. Chebrolu VV, Hines CDG, Yu H, et al. Independent estimation of T*2 for water and fat for improved accuracy of fat quantification. *Magnetic Resonance in Medicine*. 2010;63(4):849-857. doi:10.1002/mrm.22300

65. Horng DE, Hernando D, Hines CDG, Reeder SB. Comparison of R2* correction methods for accurate fat quantification in fatty liver. *Journal of Magnetic Resonance Imaging*. 2013;37(2):414-422. doi:10.1002/jmri.23835
66. Hamilton G, Yokoo T, Bydder M, et al. In vivo characterization of the liver fat 1H MR spectrum. *NMR in Biomedicine*. 2011;24(7):784-790. doi:10.1002/nbm.1622
67. Yu H, Shimakawa A, McKenzie CA, Brodsky E, Brittain JH, Reeder SB. Multiecho water-fat separation and simultaneous R estimation with multifrequency fat spectrum modeling. *Magnetic Resonance in Medicine*. 2008;60(5):1122-1134. doi:10.1002/mrm.21737
68. Hernando D, Hines CDG, Yu H, Reeder SB. Addressing phase errors in fat-water imaging using a mixed magnitude/complex fitting method. *Magnetic Resonance in Medicine*. 2012;67(3):638-644. doi:10.1002/mrm.23044
69. Liu C-Y, McKenzie CA, Yu H, Brittain JH, Reeder SB. Fat quantification with IDEAL gradient echo imaging: Correction of bias from T1 and noise. *Magnetic Resonance in Medicine*. 2007;58(2):354-364. doi:10.1002/mrm.21301
70. Yu H, McKenzie CA, Shimakawa A, et al. Multiecho reconstruction for simultaneous water-fat decomposition and T2* estimation. *Journal of Magnetic Resonance Imaging: An Official Journal of the International Society for Magnetic Resonance in Medicine*. 2007;26(4):1153–1161.
71. Ren J, Dimitrov I, Sherry AD, Malloy CR. Composition of adipose tissue and marrow fat in humans by 1H NMR at 7 Tesla. *J Lipid Res*. 2008;49(9):2055-2062. doi:10.1194/jlr.D800010-JLR200
72. Wokke BH, Bos C, Reijnierse M, et al. Comparison of dixon and T1-weighted MR methods to assess the degree of fat infiltration in duchenne muscular dystrophy patients. *Journal of Magnetic Resonance Imaging*. 2013;38(3):619–624.
73. Deoni SCL, Peters TM, Rutt BK. High-resolution T1 and T2 mapping of the brain in a clinically acceptable time with DESPOT1 and DESPOT2. *Magnetic Resonance in Medicine*. 2005;53(1):237-241. doi:10.1002/mrm.20314
74. Bernstein MA, King KF, Zhou XJ. *Handbook of MRI Pulse Sequences*. Elsevier; 2004.
75. Torrey HC. Bloch Equations with Diffusion Terms. *Phys Rev*. 1956;104(3):563-565. doi:10.1103/PhysRev.104.563
76. Stejskal EO, Tanner JE. Spin Diffusion Measurements: Spin Echoes in the Presence of a Time-Dependent Field Gradient. *J Chem Phys*. 1965;42(1):288-292. doi:10.1063/1.1695690
77. Le Bihan D, Breton E, Lallemand D, Aubin ML, Vignaud J, Laval-Jeantet M. Separation of diffusion and perfusion in intravoxel incoherent motion MR imaging. *Radiology*. 1988;168(2):497-505. doi:10.1148/radiology.168.2.3393671
78. Zhang S, Jia Q, Zhang Z, et al. Intravoxel incoherent motion MRI: emerging applications for nasopharyngeal carcinoma at the primary site. *Eur Radiol*. 2014;24(8):1998-2004. doi:10.1007/s00330-014-3203-0
79. Taouli B, Vilgrain V, Dumont E, Daire J-L, Fan B, Menu Y. Evaluation of Liver Diffusion Isotropy and Characterization of Focal Hepatic Lesions with Two Single-Shot Echo-planar MR Imaging Sequences: Prospective Study in 66 Patients. *Radiology*. 2003;226(1):71-78. doi:10.1148/radiol.2261011904
80. Kim T, Murakami T, Takahashi S, Hori M, Tsuda K, Nakamura H. Diffusion-weighted single-shot echoplanar MR imaging for liver disease. *American Journal of Roentgenology*. 1999;173(2):393-398. doi:10.2214/ajr.173.2.10430143

81. Bruegel M, Holzapfel K, Gaa J, et al. Characterization of focal liver lesions by ADC measurements using a respiratory triggered diffusion-weighted single-shot echo-planar MR imaging technique. *Eur Radiol*. 2008;18(3):477-485. doi:10.1007/s00330-007-0785-9
82. Parikh T, Drew SJ, Lee VS, et al. Focal Liver Lesion Detection and Characterization with Diffusion-weighted MR Imaging: Comparison with Standard Breath-hold T2-weighted Imaging. *Radiology*. 2008;246(3):812-822. doi:10.1148/radiol.2463070432
83. Gourtsoyianni S, Papanikolaou N, Yarmenitis S, Maris T, Karantanas A, Gourtsoyiannis N. Respiratory gated diffusion-weighted imaging of the liver: value of apparent diffusion coefficient measurements in the differentiation between most commonly encountered benign and malignant focal liver lesions. *Eur Radiol*. 2008;18(3):486-492. doi:10.1007/s00330-007-0798-4
84. Namimoto T, Yamashita Y, Sumi S, Tang Y, Takahashi M. Focal liver masses: characterization with diffusion-weighted echo-planar MR imaging. *Radiology*. 1997;204(3):739-744. doi:10.1148/radiology.204.3.9280252
85. Schmid-Tannwald C, Jiang Y, Dahi F, Rist C, Sethi I, Oto A. Diffusion-Weighted MR Imaging of Focal Liver Lesions in the Left and Right Lobes: Is There a Difference in ADC Values? *Academic Radiology*. 2013;20(4):440-445. doi:10.1016/j.acra.2012.10.012
86. Kwee TC, Takahara T, Niwa T, et al. Influence of cardiac motion on diffusion-weighted magnetic resonance imaging of the liver. *Magn Reson Mater Phy*. 2009;22(5):319-325. doi:10.1007/s10334-009-0183-1
87. Liau J, Lee J, Schroeder ME, Sirlin CB, Bydder M. Cardiac motion in diffusion-weighted MRI of the liver: artifact and a method of correction. *Journal of Magnetic Resonance Imaging*. 2012;35(2):318-327. doi:10.1002/jmri.22816
88. Mazaheri Y, Do RKG, Shukla-Dave A, Deasy JO, Lu Y, Akin O. Motion Correction of Multi-b-value Diffusion-weighted Imaging in the Liver. *Academic Radiology*. 2012;19(12):1573-1580. doi:10.1016/j.acra.2012.07.005
89. Ozaki M, Inoue Y, Miyati T, et al. Motion artifact reduction of diffusion-weighted MRI of the liver: Use of velocity-compensated diffusion gradients combined with tetrahedral gradients. *Journal of Magnetic Resonance Imaging*. 2013;37(1):172-178. doi:10.1002/jmri.23796
90. Nasu K, Kuroki Y, Fujii H, Minami M. Hepatic pseudo-anisotropy: a specific artifact in hepatic diffusion-weighted images obtained with respiratory triggering. *Magn Reson Mater Phy*. 2007;20(4):205. doi:10.1007/s10334-007-0084-0
91. Nasu K, Kuroki Y, Sekiguchi R, Nawano S. The Effect of Simultaneous Use of Respiratory Triggering in Diffusion-weighted Imaging of the Liver. *Magnetic Resonance in Medical Sciences*. 2006;5(3):129-136. doi:10.2463/mrms.5.129
92. Choi JS, Kim M-J, Chung YE, et al. Comparison of breathhold, navigator-triggered, and free-breathing diffusion-weighted MRI for focal hepatic lesions. *Journal of Magnetic Resonance Imaging*. 2013;38(1):109-118. doi:10.1002/jmri.23949
93. Murphy P, Wolfson T, Gamst A, Sirlin C, Bydder M. Error model for reduction of cardiac and respiratory motion effects in quantitative liver DW-MRI. *Magnetic Resonance in Medicine*. 2013;70(5):1460-1469. doi:10.1002/mrm.24563
94. Poyraz AK, Onur MR, Kocakoç E, Oğur E. Diffusion-weighted MRI of fatty liver. *Journal of Magnetic Resonance Imaging*. 2012;35(5):1108-1111. doi:10.1002/jmri.23519
95. d'Assignies G, Ruel M, Khiat A, et al. Noninvasive quantitation of human liver steatosis using magnetic resonance and bioassay methods. *Eur Radiol*. 2009;19(8):2033-2040. doi:10.1007/s00330-009-1351-4

96. Taviani V, Hernando D, Reeder S. Single-Voxel Diffusion-Weighted MR Spectroscopy for Fat-Corrected ADC Measurement. In: Salt Lake City, Utah, U.S.A; 2013:597.
97. Hansmann J, Hernando D, Reeder SB. Fat confounds the observed apparent diffusion coefficient in patients with hepatic steatosis. *Magnetic Resonance in Medicine*. 2013;69(2):545-552. doi:10.1002/mrm.24535
98. Pierpaoli C, Sarlls J. Polyvinyllpyrrolidone (PVP) Water Solutions as Isotropic Phantoms for Diffusion MRI Studies. In: Honolulu, Hawaii, U.S.A; 2009:1414.
99. Chenevert TL, Galbán CJ, Ivancevic MK, et al. Diffusion coefficient measurement using a temperature-controlled fluid for quality control in multicenter studies. *Journal of Magnetic Resonance Imaging*. 2011;34(4):983-987. doi:10.1002/jmri.22363
100. Lavdas I, Behan KC, Papadaki A, McRobbie DW, Aboagye EO. A phantom for diffusion-weighted MRI (DW-MRI). *Journal of Magnetic Resonance Imaging*. 2013;38(1):173-179. doi:10.1002/jmri.23950
101. Butts K, Crespigny A de, Pauly JM, Moseley M. Diffusion-weighted interleaved echo-planar imaging with a pair of orthogonal navigator echoes. *Magnetic Resonance in Medicine*. 1996;35(5):763-770. doi:10.1002/mrm.1910350518
102. Niendorf T, Dijkhuizen RM, Norris DG, Campagne M van L, Nicolay K. Biexponential diffusion attenuation in various states of brain tissue: Implications for diffusion-weighted imaging. *Magnetic Resonance in Medicine*. 1996;36(6):847-857. doi:10.1002/mrm.1910360607
103. Moseley ME, Cohen Y, Mintorovitch J, et al. Early detection of regional cerebral ischemia in cats: Comparison of diffusion- and T2-weighted MRI and spectroscopy. *Magnetic Resonance in Medicine*. 1990;14(2):330-346. doi:10.1002/mrm.1910140218
104. Guo Y, Cai Y-Q, Cai Z-L, et al. Differentiation of clinically benign and malignant breast lesions using diffusion-weighted imaging. *Journal of Magnetic Resonance Imaging*. 2002;16(2):172-178. doi:10.1002/jmri.10140
105. Bodammer N, Kaufmann J, Kanowski M, Tempelmann C. Eddy current correction in diffusion-weighted imaging using pairs of images acquired with opposite diffusion gradient polarity. *Magnetic Resonance in Medicine*. 2004;51(1):188-193. doi:10.1002/mrm.10690
106. Laubach HJ, Jakob PM, Loevblad KO, et al. A Phantom for diffusion-weighted imaging of acute stroke. *Journal of Magnetic Resonance Imaging*. 1998;8(6):1349-1354. doi:10.1002/jmri.1880080627
107. Boss M, Chenevert T, Waterton J, et al. Temperature-controlled Isotropic Diffusion Phantom with Wide Range of Apparent Diffusion Coefficients for Multicenter Assessment of Scanner Repeatability and Reproducibility. In: ; 2014.
108. Jensen JH, Helpern JA, Ramani A, Lu H, Kaczynski K. Diffusional kurtosis imaging: The quantification of non-gaussian water diffusion by means of magnetic resonance imaging. *Magnetic Resonance in Medicine*. 2005;53(6):1432-1440. doi:10.1002/mrm.20508
109. Holz M, R. Heil S, Sacco A. Temperature-dependent self-diffusion coefficients of water and six selected molecular liquids for calibration in accurate 1H NMR PFG measurements. *Physical Chemistry Chemical Physics*. 2000;2(20):4740-4742. doi:10.1039/B005319H
110. Hara M, Kuroda M, Ohmura Y, et al. A new phantom and empirical formula for apparent diffusion coefficient measurement by a 3 Tesla magnetic resonance imaging scanner. *Oncology Letters*. 2014;8(2):819-824. doi:10.3892/ol.2014.2187

111. Altbach MI, Outwater EK, Trouard TP, et al. Radial fast spin-echo method for T2-weighted imaging and T2 mapping of the liver. *Journal of Magnetic Resonance Imaging*. 2002;16(2):179-189. doi:10.1002/jmri.10142
112. Deoni SCL, Rutt BK, Peters TM. Rapid combined T1 and T2 mapping using gradient recalled acquisition in the steady state. *Magnetic Resonance in Medicine*. 2003;49(3):515-526. doi:10.1002/mrm.10407
113. Welsch GH, Scheffler K, Mamisch TC, et al. Rapid estimation of cartilage T2 based on double echo at steady state (DESS) with 3 Tesla. *Magnetic Resonance in Medicine*. 2009;62(2):544-549. doi:10.1002/mrm.22036
114. Heule R, Ganter C, Bieri O. Triple echo steady-state (TESS) relaxometry. *Magnetic Resonance in Medicine*. 2014;71(1):230-237. doi:10.1002/mrm.24659
115. Gandon Y, Olivié D, Guyader D, et al. Non-invasive assessment of hepatic iron stores by MRI. *The Lancet*. 2004;363(9406):357-362. doi:10.1016/S0140-6736(04)15436-6
116. Crawley AP, Wood ML, Henkelman RM. Elimination of transverse coherences in FLASH MRI. *Magnetic Resonance in Medicine*. 1988;8(3):248-260. doi:10.1002/mrm.1910080303
117. Smedile A, Bugianesi E. Steatosis and hepatocellular carcinoma risk. *European review for medical and pharmacological sciences*. 2005;9(5):291.
118. Cuadrado A, Orive A, García-Suárez C, et al. Non-alcoholic Steatohepatitis (NASH) and Hepatocellular Carcinoma. *OBES SURG*. 2005;15(3):442-446. doi:10.1381/0960892053576596
119. Thomsen C, Becker U, Winkler K, Christoffersen P, Jensen M, Henriksen O. Quantification of liver fat using magnetic resonance spectroscopy. *Magnetic Resonance Imaging*. 1994;12(3):487-495. doi:10.1016/0730-725X(94)92543-7
120. Reeder SB, Pineda AR, Wen Z, et al. Iterative decomposition of water and fat with echo asymmetry and least-squares estimation (IDEAL): Application with fast spin-echo imaging. *Magnetic Resonance in Medicine*. 2005;54(3):636-644. doi:10.1002/mrm.20624
121. Cassidy FH, Yokoo T, Aganovic L, et al. Fatty Liver Disease: MR Imaging Techniques for the Detection and Quantification of Liver Steatosis. *RadioGraphics*. 2009;29(1):231-260. doi:10.1148/rg.291075123
122. Reeder SB, Bice EK, Yu H, Hernando D, Pineda AR. On the performance of T2* correction methods for quantification of hepatic fat content. *Magnetic Resonance in Medicine*. 2012;67(2):389-404. doi:10.1002/mrm.23016
123. Hernando D, Liang Z-P, Kellman P. Chemical shift–based water/fat separation: A comparison of signal models. *Magnetic Resonance in Medicine*. 2010;64(3):811-822. doi:10.1002/mrm.22455
124. Yu H, Shimakawa AS, Reeder S, McKenzie CA, Brittain JH. Magnitude Fitting Following Phase Sensitive Water-Fat Separation to Remove Effects of Phase Errors. In: ; 2009.
125. Reeder SB, Robson PM, Yu H, et al. Quantification of hepatic steatosis with MRI: The effects of accurate fat spectral modeling. *Journal of Magnetic Resonance Imaging*. 2009;29(6):1332-1339. doi:10.1002/jmri.21751
126. Yu H, Shimakawa A, Hines CDG, et al. Combination of complex-based and magnitude-based multiecho water-fat separation for accurate quantification of fat-fraction. *Magnetic Resonance in Medicine*. 2011;66(1):199-206. doi:10.1002/mrm.22840
127. Berglund J, Kullberg J. Three-dimensional water/fat separation and T estimation based on whole-image optimization—Application in breathhold liver imaging at 1.5 T. *Magnetic Resonance in Medicine*. 2012;67(6):1684-1693. doi:10.1002/mrm.23185

128. Jonker JT, Wida R, Hammer S. 1.5 T and 7T MR Spectroscopy of Tissue Specific Changes in Ectopic Fat Content in Response to Exercise Training in Type 2 Diabetes Mellitus Patients: The ATLAS-study. In: *Proc Intl Soc Mag Reson Med*. ; 2011.
129. Schwenzer NF, Machann J, Haap MM, et al. T2* Relaxometry in Liver, Pancreas, and Spleen in a Healthy Cohort of One Hundred Twenty-Nine Subjects–Correlation With Age, Gender, and Serum Ferritin: *Investigative Radiology*. 2008;43(12):854-860. doi:10.1097/RLI.0b013e3181862413
130. Hines CD, Yokoo T, Bydder M, Sirlin CB, Reeder SB. Optimization of flip angle to allow tradeoffs in T1 bias and SNR performance for fat quantification. In: *Proc Int Soc Magn Reson Med*. Vol 18. ; 2010:2927.
131. de Bazelaire CMJ, Duhamel GD, Rofsky NM, Alsop DC. MR Imaging Relaxation Times of Abdominal and Pelvic Tissues Measured in Vivo at 3.0 T: Preliminary Results. *Radiology*. 2004;230(3):652-659. doi:10.1148/radiol.2303021331
132. Naressi A, Couturier C, Devos JM, et al. Java-based graphical user interface for the MRUI quantitation package. *MAGMA*. 2001;12(2):141. doi:10.1007/BF02668096
133. Sharma P, Martin DR, Pineda N, et al. Quantitative analysis of T2-correction in single-voxel magnetic resonance spectroscopy of hepatic lipid fraction. *Journal of Magnetic Resonance Imaging*. 2009;29(3):629-635. doi:10.1002/jmri.21682
134. Reeder SB, McKenzie CA, Pineda AR, et al. Water–fat separation with IDEAL gradient-echo imaging. *Journal of Magnetic Resonance Imaging: An Official Journal of the International Society for Magnetic Resonance in Medicine*. 2007;25(3):644–652.
135. Hernando D, Sharma SD, Kramer H, Reeder SB. On the confounding effect of temperature on chemical shift-encoded fat quantification. *Magnetic resonance in medicine*. 2014;72(2):464–470.
136. Heba ER, Sirlin CB, Wolfson T, Gamst A, Loomba R, Middleton MS. Agreement of 2-, 3-, 4-, 5-and 6-echo MRI-PDFF with MRS-PDFF in 580 adults with known or suspected non-alcoholic fatty liver disease (NAFLD). In: *Proceedings of the 22nd Annual Meeting of ISMRM, Milan, Italy*. ; 2014:138.
137. Bley TA, Wieben O, François CJ, Brittain JH, Reeder SB. Fat and water magnetic resonance imaging. *Journal of Magnetic Resonance Imaging*. 2010;31(1):4–18.
138. Reeder SB, Cruite I, Hamilton G, Sirlin CB. Quantitative assessment of liver fat with magnetic resonance imaging and spectroscopy. *Journal of Magnetic Resonance Imaging*. 2011;34(4):729-749. doi:10.1002/jmri.22580
139. Yokoo T, Serai SD, Pirasteh A, et al. Linearity, Bias, and Precision of Hepatic Proton Density Fat Fraction Measurements by Using MR Imaging: A Meta-Analysis. *Radiology*. 2017;286(2):486-498. doi:10.1148/radiol.2017170550
140. Lingvay I, Esser V, Legendre JL, et al. Noninvasive Quantification of Pancreatic Fat in Humans. *None*. 2009;94(10):4070-4076. doi:10.1210/jc.2009-0584
141. Wren TAL, Bluml S, Tseng-Ong L, Gilsanz V. Three-Point Technique of Fat Quantification of Muscle Tissue as a Marker of Disease Progression in Duchenne Muscular Dystrophy: Preliminary Study. *American Journal of Roentgenology*. 2008;190(1):W8-W12. doi:10.2214/AJR.07.2732
142. Adam SZ, Nikolaidis P, Horowitz JM, et al. Chemical Shift MR Imaging of the Adrenal Gland: Principles, Pitfalls, and Applications. *RadioGraphics*. 2016;36(2):414-432. doi:10.1148/rg.2016150139

143. Hu HH, Hines CDG, Smith DL, Reeder SB. Variations in T2* and fat content of murine brown and white adipose tissues by chemical-shift MRI. *Magnetic Resonance Imaging*. 2012;30(3):323-329. doi:10.1016/j.mri.2011.12.004
144. Franz D, Weidlich D, Freitag F, et al. Association of proton density fat fraction in adipose tissue with imaging-based and anthropometric obesity markers in adults. *International Journal of Obesity*. 2018;42(2):175-182. doi:10.1038/ijo.2017.194
145. Johnson BL, Schroeder ME, Wolfson T, et al. Effect of flip angle on the accuracy and repeatability of hepatic proton density fat fraction estimation by complex data-based, T1-independent, T2*-corrected, spectrum-modeled MRI. *Journal of Magnetic Resonance Imaging*. 2014;39(2):440-447. doi:10.1002/jmri.24153
146. Kühn J-P, Jahn C, Hernando D, et al. T1 bias in chemical shift-encoded liver fat-fraction: Role of the flip angle. *Journal of Magnetic Resonance Imaging*. 2014;40(4):875-883. doi:10.1002/jmri.24457
147. Karampinos DC, Yu H, Shimakawa A, Link TM, Majumdar S. T1-corrected fat quantification using chemical shift-based water/fat separation: Application to skeletal muscle. *Magnetic Resonance in Medicine*. 2011;66(5):1312-1326. doi:10.1002/mrm.22925
148. Tamada D, Wakayama T, Onishi H, Motosugi U. Multiparameter estimation using multi-echo spoiled gradient echo with variable flip angles and multicontrast compressed sensing. *Magnetic Resonance in Medicine*. 2018;80(4):1546-1555. doi:10.1002/mrm.27151
149. Horng DE, Hernando D, Reeder SB. Quantification of liver fat in the presence of iron overload. *Journal of Magnetic Resonance Imaging*. 2017;45(2):428-439. doi:10.1002/jmri.25382
150. Hamilton G, Middleton MS, Bydder M, et al. Effect of PRESS and STEAM sequences on magnetic resonance spectroscopic liver fat quantification. *Journal of Magnetic Resonance Imaging*. 2009;30(1):145-152. doi:10.1002/jmri.21809
151. Hu HH, Börnert P, Hernando D, et al. ISMRM workshop on fat–water separation: insights, applications and progress in MRI. *Magnetic resonance in medicine*. 2012;68(2):378–388.
152. Hines CDG, Yu H, Shimakawa A, McKenzie CA, Brittain JH, Reeder SB. T1 independent, T2* corrected MRI with accurate spectral modeling for quantification of fat: Validation in a fat-water-SPIO phantom. *Journal of Magnetic Resonance Imaging*. 2009;30(5):1215-1222. doi:10.1002/jmri.21957
153. Scharf LL, McWhorter LT. Geometry of the Cramer-Rao bound. *Signal Processing*. 1993;31(3):301-311. doi:10.1016/0165-1684(93)90088-R
154. Mojtahed A, Kelly CJ, Herlihy AH, et al. Reference range of liver corrected T1 values in a population at low risk for fatty liver disease—a UK Biobank sub-study, with an appendix of interesting cases. *Abdom Radiol*. 2019;44(1):72-84. doi:10.1007/s00261-018-1701-2
155. Henninger B, Kremser C, Rauch S, et al. Evaluation of MR imaging with T1 and T2* mapping for the determination of hepatic iron overload. *Eur Radiol*. 2012;22(11):2478-2486. doi:10.1007/s00330-012-2506-2
156. Hoad CL, Palaniyappan N, Kaye P, et al. A study of T1 relaxation time as a measure of liver fibrosis and the influence of confounding histological factors. *NMR in Biomedicine*. 2015;28(6):706-714. doi:10.1002/nbm.3299
157. Motosugi U, Bannas P, Hernando D, Rahimi MS, Holmes JH, Reeder SB. Intraindividual Crossover Comparison of Gadoxetic Acid Dose for Liver MRI in Normal Volunteers. *Magnetic Resonance in Medical Sciences*. 2016;15(1):60-72. doi:10.2463/mrms.2015-0005

158. Park CC, Hamilton G, Desai A, et al. Effect of intravenous gadoxetate disodium and flip angle on hepatic proton density fat fraction estimation with six-echo, gradient-recalled-echo, magnitude-based MR imaging at 3T. *Abdom Radiol*. 2017;42(4):1189-1198. doi:10.1007/s00261-016-0992-4
159. Hernando D, Wells SA, Vigen KK, Reeder SB. Effect of hepatocyte-specific gadolinium-based contrast agents on hepatic fat-fraction and R2∗. *Magnetic Resonance Imaging*. 2015;33(1):43-50. doi:10.1016/j.mri.2014.10.001
160. Bernstein MA, Fain SB, Riederer SJ. Effect of windowing and zero-filled reconstruction of MRI data on spatial resolution and acquisition strategy. *Journal of Magnetic Resonance Imaging*. 2001;14(3):270-280. doi:10.1002/jmri.1183
161. Campo CA, Hernando D, Schubert T, Bookwalter CA, Pay AJV, Reeder SB. Standardized Approach for ROI-Based Measurements of Proton Density Fat Fraction and R2* in the Liver. *American Journal of Roentgenology*. 2017;209(3):592-603. doi:10.2214/AJR.17.17812
162. Artz NS, Haufe WM, Hooker CA, et al. Reproducibility of MR-based liver fat quantification across field strength: Same-day comparison between 1.5T and 3T in obese subjects. *Journal of Magnetic Resonance Imaging*. 2015;42(3):811-817. doi:10.1002/jmri.24842
163. Rehm JL, Wolfgram PM, Hernando D, Eickhoff JC, Allen DB, Reeder SB. Proton density fat-fraction is an accurate biomarker of hepatic steatosis in adolescent girls and young women. *Eur Radiol*. 2015;25(10):2921-2930. doi:10.1007/s00330-015-3724-1
164. Bihan DL, Poupon C, Amadon A, Lethimonnier F. Artifacts and pitfalls in diffusion MRI. *Journal of Magnetic Resonance Imaging*. 2006;24(3):478-488. doi:10.1002/jmri.20683
165. Assaf Y, Freidlin RZ, Rohde GK, Basser PJ. New modeling and experimental framework to characterize hindered and restricted water diffusion in brain white matter. *Magnetic Resonance in Medicine*. 2004;52(5):965-978. doi:10.1002/mrm.20274
166. Cohen Y, Assaf Y. High b-value q-space analyzed diffusion-weighted MRS and MRI in neuronal tissues – a technical review. *NMR in Biomedicine*. 2002;15(7-8):516-542. doi:10.1002/nbm.778
167. Jian B, Vemuri BC, Özarslan E, Carney PR, Mareci TH. A novel tensor distribution model for the diffusion-weighted MR signal. *NeuroImage*. 2007;37(1):164-176. doi:10.1016/j.neuroimage.2007.03.074
168. Yablonskiy DA, Bretthorst GL, Ackerman JJH. Statistical model for diffusion attenuated MR signal. *Magnetic Resonance in Medicine*. 2003;50(4):664-669. doi:10.1002/mrm.10578
169. Ichikawa T, Haradome H, Hachiya J, Nitatori T, Araki T. Diffusion-weighted MR imaging with a single-shot echoplanar sequence: detection and characterization of focal hepatic lesions. *American Journal of Roentgenology*. 1998;170(2):397-402. doi:10.2214/ajr.170.2.9456953
170. Maier SE, Bogner P, Bajzik G, et al. Normal Brain and Brain Tumor: Multicomponent Apparent Diffusion Coefficient Line Scan Imaging. *Radiology*. 2001;219(3):842-849. doi:10.1148/radiology.219.3.r01jn02842
171. Yamasaki F, Kurisu K, Satoh K, et al. Apparent Diffusion Coefficient of Human Brain Tumors at MR Imaging. *Radiology*. 2005;235(3):985-991. doi:10.1148/radiol.2353031338
172. Kuroki Y, Nasu K, Kuroki S, et al. Diffusion-weighted Imaging of Breast Cancer with the Sensitivity Encoding Technique: Analysis of the Apparent Diffusion Coefficient Value. *Magnetic Resonance in Medical Sciences*. 2004;3(2):79-85. doi:10.2463/mrms.3.79

173. Park MJ, Cha ES, Kang BJ, Ihn YK, Baik JH. The Role of Diffusion-Weighted Imaging and the Apparent Diffusion Coefficient (ADC) Values for Breast Tumors. *Korean Journal of Radiology*. 2007;8(5):390-396. doi:10.3348/kjr.2007.8.5.390
174. Woodhams R, Matsunaga K, Iwabuchi K, et al. Diffusion-weighted imaging of malignant breast tumors: the usefulness of apparent diffusion coefficient (ADC) value and ADC map for the detection of malignant breast tumors and evaluation of cancer extension. *Journal of computer assisted tomography*. 2005;29(5):644–649.
175. Matsuki M, Inada Y, Tatsugami F, Tanikake M, Narabayashi I, Katsuoka Y. Diffusion-weighted MR imaging for urinary bladder carcinoma: initial results. *Eur Radiol*. 2007;17(1):201-204. doi:10.1007/s00330-006-0281-7
176. Muraoka N, Uematsu H, Kimura H, et al. Apparent diffusion coefficient in pancreatic cancer: Characterization and histopathological correlations. *Journal of Magnetic Resonance Imaging*. 2008;27(6):1302-1308. doi:10.1002/jmri.21340
177. Huang H, Ceritoglu C, Li X, et al. Correction of B0 susceptibility induced distortion in diffusion-weighted images using large-deformation diffeomorphic metric mapping. *Magnetic Resonance Imaging*. 2008;26(9):1294-1302. doi:10.1016/j.mri.2008.03.005
178. Reese TG, Heid O, Weisskoff RM, Wedeen VJ. Reduction of eddy-current-induced distortion in diffusion MRI using a twice-refocused spin echo. *Magnetic Resonance in Medicine*. 2003;49(1):177-182. doi:10.1002/mrm.10308
179. Price WS. Pulsed-field gradient nuclear magnetic resonance as a tool for studying translational diffusion: Part II. Experimental aspects. *Concepts in Magnetic Resonance*. 1998;10(4):197-237. doi:10.1002/(SICI)1099-0534(1998)10:4<197::AID-CMR1>3.0.CO;2-S
180. Tofts PS, Lloyd D, Clark CA, et al. Test liquids for quantitative MRI measurements of self-diffusion coefficient in vivo. *Magnetic Resonance in Medicine*. 2000;43(3):368-374. doi:10.1002/(SICI)1522-2594(200003)43:3<368::AID-MRM8>3.0.CO;2-B
181. Olson DL, Peck TL, Webb AG, Magin RL, Sweedler JV. High-Resolution Microcoil 1H-NMR for Mass-Limited, Nanoliter-Volume Samples. *Science*. 1995;270(5244):1967-1970. doi:10.1126/science.270.5244.1967
182. Kumar V, Yang T, Yang Y. Interpolymer complexation. I. Preparation and characterization of a polyvinyl acetate phthalate-polyvinylpyrrolidone (PVAP-PVP) complex. *International Journal of Pharmaceutics*. 1999;188(2):221-232. doi:10.1016/S0378-5173(99)00223-9
183. Reischauer C, Staempfli P, Jaermann T, Boesiger P. Construction of a temperature-controlled diffusion phantom for quality control of diffusion measurements. *Journal of Magnetic Resonance Imaging*. 2009;29(3):692-698. doi:10.1002/jmri.21665
184. Ertl H, Dullien F a. L. Self-diffusion and viscosity of some liquids as a function of temperature. *AIChE Journal*. 1973;19(6):1215-1223. doi:10.1002/aic.690190619
185. Toryanik AI, Taranenko VN. Molecular mobility and structure in water-acetone mixtures. *J Struct Chem*. 1988;28(5):714-719. doi:10.1007/BF00752054
186. Numano T, Homma K, Hirose T. Diffusion-weighted three-dimensional MP-RAGE MR imaging. *Magnetic Resonance Imaging*. 2005;23(3):463-468. doi:10.1016/j.mri.2004.12.002
187. Hernando D, Karampinos DC, King KF, et al. Removal of olefinic fat chemical shift artifact in diffusion MRI. *Magnetic Resonance in Medicine*. 2011;65(3):692-701. doi:10.1002/mrm.22670

188. Kapur GS, Cabrita EJ, Berger S. The qualitative probing of hydrogen bond strength by diffusion-ordered NMR spectroscopy. *Tetrahedron Letters*. 2000;41(37):7181-7185. doi:10.1016/S0040-4039(00)01188-6
189. Zhang N, Fitsanakis VA, Aschner M, Avison MJ, Gore JC. Variations in relaxivity of manganese between regions in rat brain. *Hippocampus*. 2006;1:1–2.
190. Mierisová Š, Ala-Korpela M. MR spectroscopy quantitation: a review of frequency domain methods. *NMR in Biomedicine*. 2001;14(4):247-259. doi:10.1002/nbm.697
191. Scheffler K, Hennig J. T1 quantification with inversion recovery TrueFISP. *Magnetic Resonance in Medicine*. 2001;45(4):720-723. doi:10.1002/mrm.1097
192. Kosta P, Argyropoulou MI, Markoula S, Konitsiotis S. MRI evaluation of the basal ganglia size and iron content in patients with Parkinson’s disease. *J Neurol*. 2006;253(1):26-32. doi:10.1007/s00415-005-0914-9
193. Aletras AH, Kellman P, Derbyshire JA, Arai AE. ACUT2E TSE-SSFP: A hybrid method for T2-weighted imaging of edema in the heart. *Magnetic Resonance in Medicine*. 2008;59(2):229-235. doi:10.1002/mrm.21490
194. Aherne T, Yee ES, Tscholakoff D, Gollin G, Higgins C, Ebert PA. Diagnosis of acute and chronic cardiac rejection by magnetic resonance imaging: a non-invasive in-vivo study. *J Cardiovasc Surg (Torino)*. 1988;29(5):587-590.
195. Dolan RS, Rahsepar AA, Blaisdell J, et al. Multiparametric Cardiac Magnetic Resonance Imaging Can Detect Acute Cardiac Allograft Rejection After Heart Transplantation. *JACC: Cardiovascular Imaging*. 2019;12(8, Part 2):1632-1641. doi:10.1016/j.jcmg.2019.01.026
196. Li X, Benjamin Ma C, Link TM, et al. In vivo T1ρ and T2 mapping of articular cartilage in osteoarthritis of the knee using 3T MRI. *Osteoarthritis and Cartilage*. 2007;15(7):789-797. doi:10.1016/j.joca.2007.01.011
197. Wood JC, Enriquez C, Ghugre N, et al. MRI R2 and R2* mapping accurately estimates hepatic iron concentration in transfusion-dependent thalassemia and sickle cell disease patients. *Blood*. 2005;106(4):1460-1465. doi:10.1182/blood-2004-10-3982
198. Sollmann N, Mathonia N, Weidlich D, et al. Quantitative magnetic resonance imaging of the upper trapezius muscles – assessment of myofascial trigger points in patients with migraine. *The Journal of Headache and Pain*. 2019;20(1):8. doi:10.1186/s10194-019-0960-9
199. Reiter DA, Roque RA, Lin P-C, Doty SB, Pleshko N, Spencer RG. Improved specificity of cartilage matrix evaluation using multiexponential transverse relaxation analysis applied to pathomimetically degraded cartilage. *NMR in Biomedicine*. 2011;24(10):1286-1294. doi:10.1002/nbm.1690
200. Reiter DA, Lin P-C, Fishbein KW, Spencer RG. Multicomponent T2 relaxation analysis in cartilage. *Magnetic Resonance in Medicine*. 2009;61(4):803-809. doi:10.1002/mrm.21926
201. Juras V, Bohndorf K, Heule R, et al. A comparison of multi-echo spin-echo and triple-echo steady-state T2 mapping for in vivo evaluation of articular cartilage. *Eur Radiol*. 2016;26(6):1905-1912. doi:10.1007/s00330-015-3979-6
202. Ben-Eliezer N, Sodickson DK, Block KT. Rapid and accurate T2 mapping from multi–spin-echo data using Bloch-simulation-based reconstruction. *Magnetic Resonance in Medicine*. 2015;73(2):809-817. doi:10.1002/mrm.25156
203. Brittain JH, Hu BS, Wright GA, Meyer CH, Macovski A, Nishimura DG. Coronary Angiography with Magnetization-Prepared T2 Contrast. *Magnetic Resonance in Medicine*. 1995;33(5):689-696. doi:10.1002/mrm.1910330515

204. Gold GE, Han E, Stainsby J, Wright G, Brittain J, Beaulieu C. Musculoskeletal MRI at 3.0 T: Relaxation Times and Image Contrast. *American Journal of Roentgenology*. 2004;183(2):343-351. doi:10.2214/ajr.183.2.1830343
205. Foltz WD, Al-Kwifi O, Sussman MS, Stainsby JA, Wright GA. Optimized spiral imaging for measurement of myocardial T2 relaxation. *Magnetic Resonance in Medicine*. 2003;49(6):1089-1097. doi:10.1002/mrm.10467
206. Heule R, Ganter C, Bieri O. Rapid estimation of cartilage T2 with reduced T1 sensitivity using double echo steady state imaging. *Magnetic Resonance in Medicine*. 2014;71(3):1137-1143. doi:10.1002/mrm.24748
207. Staroswiecki E, Granlund KL, Alley MT, Gold GE, Hargreaves BA. Simultaneous estimation of T2 and apparent diffusion coefficient in human articular cartilage in vivo with a modified three-dimensional double echo steady state (DESS) sequence at 3 T. *Magnetic Resonance in Medicine*. 2012;67(4):1086-1096. doi:10.1002/mrm.23090
208. Zur Y, Wood ML, Neuringer LJ. Spoiling of transverse magnetization in steady-state sequences. *Magnetic Resonance in Medicine*. 1991;21(2):251-263. doi:10.1002/mrm.1910210210
209. Christoffersson JO, Olsson LE, Sjöberg S. Nickel-doped agarose gel phantoms in MR imaging. *Acta radiologica*. 1991;32(5):426–431.
210. Pykett IL, Rosen BR, Buonanno FS, Brady TJ. Measurement of spin-lattice relaxation times in nuclear magnetic resonance imaging. *Phys Med Biol*. 1983;28(6):723–729. doi:10.1088/0031-9155/28/6/012
211. Liu F, Chaudhary R, Hurley SA, et al. Rapid multicomponent T2 analysis of the articular cartilage of the human knee joint at 3.0T. *Journal of Magnetic Resonance Imaging*. 2014;39(5):1191-1197. doi:10.1002/jmri.24290
212. Eminian S, Hajdu SD, Meuli RA, Maeder P, Hagmann P. Rapid high resolution T1 mapping as a marker of brain development: Normative ranges in key regions of interest. *PLOS ONE*. 2018;13(6):e0198250. doi:10.1371/journal.pone.0198250
213. Hernando D, Artz NS, Hamilton G, Roldan-Alzate A, Reeder S. Fully automated processing of multi-echo spectroscopy data for liver fat quantification. In: *Proceedings of the 22nd Annual Meeting of ISMRM. Milan, Italy*. Vol 2884. ; 2014.
214. Henkelman RM, McVeigh ER, Crawley AP, Kucharczyk W. Very slow in-plane flow with gradient echo imaging. *Magnetic Resonance Imaging*. 1989;7(4):383-393. doi:10.1016/0730-725X(89)90487-6
215. Reeder S, McVeigh E. Velocity Spoiling of Transverse Magnetization: Implications for CINE MRI. In: Ney York, NY, U.S.A; 1993:1268.
216. Liu F, Block WF, Kijowski R, Samsonov A. Rapid multicomponent relaxometry in steady state with correction of magnetization transfer effects. *Magnetic Resonance in Medicine*. 2016;75(4):1423-1433. doi:10.1002/mrm.25672
217. Sacolick LI, Wiesinger F, Hancu I, Vogel MW. B1 mapping by Bloch-Siegert shift. *Magnetic Resonance in Medicine*. 2010;63(5):1315-1322. doi:10.1002/mrm.22357
218. Hurley SA, Yarnykh VL, Johnson KM, Field AS, Alexander AL, Samsonov AA. Simultaneous variable flip angle–actual flip angle imaging method for improved accuracy and precision of three-dimensional T1 and B1 measurements. *Magnetic Resonance in Medicine*. 2012;68(1):54-64. doi:10.1002/mrm.23199

219. Xiaoke W, Scott R, Diego H. Single MR Spectral Peak Diffusion Phantom with Wide ADC Range Based on Acetone, H2O and Manganese Chloride. In: *Proceedings of the 24th Annual Meeting of ISMRM, Singapore, Singapore*. ; 2016:0921.